Recycling of Glass Fibre Reinforced Aluminium Laminates and Silicon Removal from Aerospace Al Alloy

PhD thesis

October 2012

Guoliang Zhu

This research described in this thesis was performed in the department of Materials Science and Engineering of Delft University of Technology, and in the department of Materials Science and Engineering of Shanghai Jiao Tong University.

T̆U Delft

Delft University of Technology

Recycling of Glass Fibre Reinforced Aluminium Laminates and Silicon Removal from Aerospace Al Alloy

Proefschrift

ter verkrijging van de graad van doctor
aan de Technische Universiteit Delft;
op gezag van de Rector Magnificus prof. ir. K.C.A.M. Luyben;
voorzitter van het College van Promoties
in het openbaar te verdedigen op dinsdag 6 november 2012 om 10.00 uur

door

Guoliang ZHU

Master of Science in Materials Processing
Harbin Institute of Technology, Harbin, China
geboren te Linli, Hunan, China

Keywords: Fibre Metal Laminates, GLARE, Recycling, 2024 Al alloy, Silicon, Purification, Doping, First-principles calculation

To my family…

Preface

This Ph.D. research, *Recycling of Glass Fibre Reinfoced Aluminium Laminates and Impurity Silicon Removal from Aerospace Al Alloys*, is started from September 2006. The first three years research work was carried out at the Department of Materials Science and Engineering, Shanghai Jiao Tong University (SJTU). The research in SJTU is a subproject of the National Key Basic Research Program of China (No.2005CB623703). The subproject is aimed at exploring a solution for impurity elements (Fe and Si) removal from industry pure Al and the recycled aerospace aluminium alloys due to their harmful influence on the fracture toughness of Al alloys. The objective of my research is to find a practical solution for the impurity Si removal from Al alloy melt in industrial scale. Si purification efficiency by using Ti addition was investigated in this thesis. The first-principles calculation was also employed to give us insight to the Si substitution behaviour in Al_3Ti, which is beneficial to understand the Si removal mechanism and the purification potential of Ti addition. The research results are presented in Chapter 4.

As a joint PhD student, I worked at Department of Materials Science and Engineering, Delft University of Technology (TU Delft) in the latter three years (from Oct. 2009 to Oct. 2012), focusing on the recycling of GLAss fibre ERinforced aluminium laminates (GLARE). This research was supported by the Royal Netherlands Academy of Science and Arts (KNAW) under projects No. 09CDP023 and 10CDP026. Delamination is the first and critical process for the recovery of materials from GLARE scrap, thermal method is used to decompose the resins between 2024 Al sheets and S2-glass fibre layers in this research. After the delamination, S2-glass fibres are obtained and 2024 Al sheets can be recovered by refining method. The related results are presented in Chapter 2 and Chapter 3.

Guoliang Zhu
October, 2012

Acknowledgements

This thesis would not have been made a reality without the guidance, support, help and understanding of many people involved directly or indirectly. I would like to thank one and all who helped me to achieve this.

First of all, I like to express my deepest gratitude to my supervisors Prof. dr. Rob Boom and Prof. dr. Yongxiang Yang for their tremendous guidance and encouragement. Professor Boom has always been enthusiastic, helpful and inspiriting to me, he always is generous when I need his help. I had a great support of Professor Yongxiang Yang which helped me of keeping my mind disengaged from existing difficulties. Professor Yongxiang Yang always provides his invaluable guidance, encouragement and willingness to address the queries whenever I knocked his door. I am extremely thankful to my daily supervisor Dr. Yanping Xiao who is a very kind, patient, helpful and generous person. Dr. Xiao's knowledge, research experiences and invaluable guidance have been very beneficial to this thesis. She is always generous when I ask for her help. I am grateful for what she has been, at times more a friend, than simply a daily supervisor. I would like to thank Mrs. Olga Wens-van Swol for her kind help during my PhD life. I would also like to thank Dr. Guiming Song for his help on SEM and TG test, as well as many pleasant and useful discussions.

I want to express my sincere thankful to Professor Baode Sun who is my supervisor in Shanghai Jiao Tong University. He brought me into this interesting research field, and taught me how to understand the complex mechanisms behind the experimental phenomena. His invaluable guidance throughout my PhD period in SJTU has been a pleasant learning experience. I also give my special thanks to Prof. Jun Wang in SJTU for everything he has done for me. He has always been around to help me professionally and personally. Other two very helpful and important people in SJTU are Dr. Da Shu and Dr. Yongbing Dai, thanks for their helpful guidance and nutritive discussions on experimental and simulation work. I also would like to thank Dr. Jianwei Gao, Dr. Anping Dong, Dr. Baoping Li, Dr. Haiyan Gao, Dr. Yanfeng Han, Dr. Zhengping Mao, Dr. Bo He, Dr. Jiao Zhang, Dr. Fei Li, Dr. Qisen Huang, Dr. Wencai Liu, Mr. Xianghui Wan, Mr. Sancai Ding for all they have done for me during this period.

The kind experimental help provided by John van den Berg, Ruud Hendrikx, Kees Kwakernaak, Lambert Schipperheijn, M.A. Leeflang. I would like to thanks Prof. Rinze Benedictus and Mr. Alonso Madruga from faculty LR for the GLARE prepregs preparation.

During my PhD, I was lucky to meet plenty of amazing colleagues. I have to thank Zhan Zhang, Qingshi Song, Yingxia Qu and Liang Zhang who did not refuse to help in any aspect if they could. Besides the interesting discussion and invaluable suggestions, I also

appreciate the wonderful time together with you guys, playing football, dinner, travel, BBQ, playing cards. I also want to thank Dr. Yulia Meteleva-Fischer who is always kind to help me in the laboratory.

Concerning the non-academic side of my time in The Netherlands, I have to think Dr. Derong Kong and Xiaoqian Lv for helping me in many aspects, especially during my initial days in The Netherlands. There are many other aspects for which I had the pleasure of sharing great company with Wenjian Li, Xiaojing Jin, Zhiming Yang, Jinhua Kan, Yanbin Shen, Yunhe Zhang, Zhe Guo, Dr. Chuangxin Zhao, Dr. Zhiguang Huan, Hong Liu, Dr. Lei Wu, Dr. Fuqiang Lai, Liyuan Fan, Gensheng Zhao, Yuting Tai, Lijie Qiu. My heartfelt thanks to each and everyone of you for all the help and happy time during my PhD life in The Netherlands.

Finally, I owe lot more than the word of 'Thanks' to my family. My parents always try their best to support me and my younger sister, give us the best they can provide, respect all the important and independent decisions that we made. They are my highly respected supervisors in my life. At last, I have to thank my younger sister for her support and encouragements.

Guoliang Zhu (Delft, October 2012)

Contents

Chapter 1 Introduction

As one member of Fibre Metal Laminates family, GLARE (GLAss fibre REinforced aluminum laminates) was invented by TU Delft, S2-glass fibres and 2024 Al alloy sheets are the main components in GLARE laminate structure. Now, about 500 m² GLARE is used as fuselage in each Airbus A380 due to its better weight saving, higher ultimate tensile strength, better blunt notch strength, excellent fire resistance and enhanced impact resistance compared to monolithic 2024 Al alloy. Many tons of new GLARE scrap has been accumulated during A380 manufacturing, and more End-of-Life (EOL) GLARE scrap will be generated after retire of planes within forty years. The recycling of energy intensive material 2024 Al and S2-glass fibre from GLARE scrap can contribute to the sustainability of the aluminium industry and fibre industry.

Si is a harmful impurity for aerospace Al alloys, and Si concentration is strictly controlled in aerospace Al alloys. But little Al alloy scrap with high Si concentration is usually mixed together with aerospace Al alloy scrap during the recycling of aerospace Al alloys, thus Si concentration in final secondary aerospace alloys exceeds the upper limit of nominal concentration. Besides the improvement of the efficiency of scrap classification, the removal of impurity Si from recycled aerospace Al alloys is also an option to improve the quality of secondary aerospace Al alloys.

In this chapter, the state of the art of the recycling of Fibre Metal Laminates as well as the recycling of aerospace Al alloy are briefly introduced. The structure of this thesis is presented.

1.1 Background

The 'Sustainable Development' concept was firstly introduced in the 1987 United Nations report of the Brundtland commission, and it is defined as follows [1]:

Sustainable Development is a development that meets the needs of the present without compromising the ability of future generations to meet their own needs. It contains within it two concepts: (1) the concept of needs, in particular the essential needs of the world's poor, to which overriding priority should be given; and (2) the idea of limitations imposed by the state of technology and social organization on the environment's ability to meet present and future needs.

Nobody doubts its importance today with the oil reserve decreasing rapidly. The climate change caused by pollutions and emissions from industrial activities, traffic, housing and farming, together with its hazardous effects also makes us focus on sustainable development. Technology innovation, development of new sources of energy and recycling of waste materials are three important contributors to our sustainable society. But, compared with technology innovation and development of new sources of energy, recycling is more easily to practice and it is already in practice for a long time. Recycling technologies have been developed in many different ways. In fact, with the industrial revolution, recycling has become one important sector in the industry chain, both in the field of organic materials and the field of inorganic materials. In the past 80 years, the concern about the environmental impact of municipal and industrial activities by emission and disposal of all kind of wastes grew considerably [2]. A good relationship between society and technology [3] is necessary to achieve sustainable development and the involvement of ethics is also crucial [4].

Closing the loop of the product life cycle is vital for the continued use of the materials in some applications. This demand has driven not only a great amount of research on recycling processes, but also the formation of several collaborative entities working on a more commercial or industrial level [5]. Another advantage of recycling research is that it can provide useful information for material designers to improve the recyclability of products.

This thesis focuses on materials recycling from GLARE (GLAss fibre REinforced aluminium laminates) scrap. The schematic diagram for the GLARE life cycle is presented in Figure 1.1. GLARE is one member of the Fibre Metal Laminates family, and is invented by TU Delft and AKZO. In 2012 about 500 m^2 GLARE is employed in the fuselage of each Airbus A380.
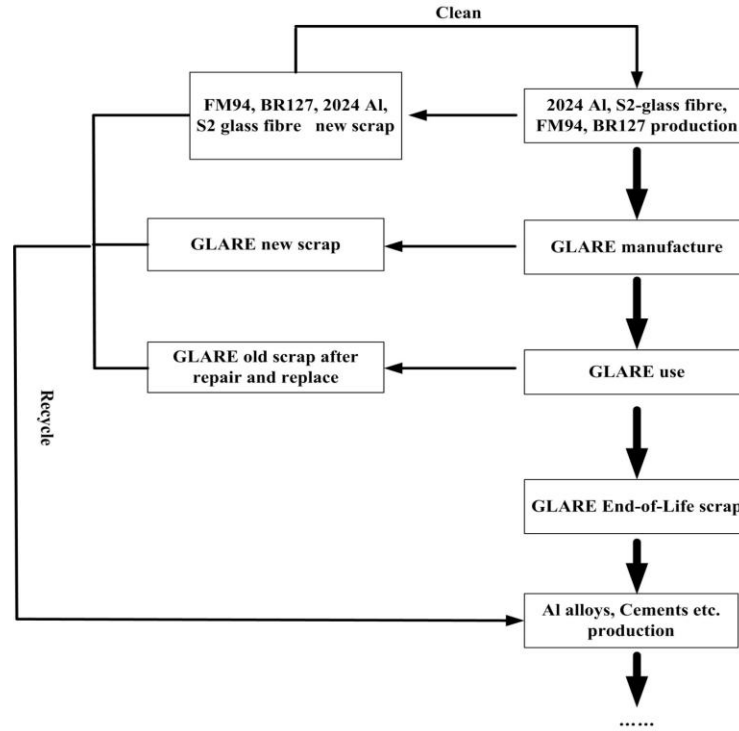
Figure 1.1 Schematic diagram for GLARE life cycle.

With the increased plane orders of Airbus A380, more End-of-Life (EOL) GLARE scrap will be generated after retire of planes within forty years. Moreover, already many tons new GLARE scrap has been accumulated during the Airbus A380 manufacturing. The estimation of GLARE scrap generation is presented in Table 1.1. The expected service period of A380 is 40 years based on the service period of A300, and we assume that 20 planes will be retired per year from 2045. We also assume that Airbus Company will stop production of A380 at 2045. The expected average order of A380 is 20 planes per year during the period of 2012-2045. The weight ratio of GLARE new scrap is 10% during manufacturing [6].

Table 1.1 Estimation of the yield of GLARE scrap.

Year	2012	2020	2030	2045 Stop production & First plane will be retired	2085 All planes are retired
A380 orders	253	413	613	913	913
End-of-Life scrap [t]	0	0	0	112	5094
New scrap [t]	157	256	380	566	566
Total scrap [t]	157	256	380	678	5660

3

Although GLARE is mainly applied in the aerospace industry and the yield of GLARE is limited compared with that of carbon fibre reinforced polymers (CFRPs), recycling of both the manufacturing new scrap and EOL old scrap already becomes a relevant issue and should be seriously considered. For many years, composite waste has been disposed of in landfill. An EU Directive on Landfill of Waste (Directive 99/31/EC) will result in a reduction in the amount of organic material landfilled. As a consequence, it is already illegal to landfill composites waste in many EU countries [7]. The glass fibre in GLARE is hard to decompose after landfill and the aerospace Al alloy is an energy intensive material (196-257 MJ/kg) [8-10], therefore GLARE recycling is important from both environment protection and economic benefits viewpoints. Moreover, the investigation of GLARE recycling can provide valuable reference information for the recycling of other FMLs. It is also helpful to expand applications of FMLs if we can prove that FMLs have a good recyclability.

Up to now, it is difficult to separate each type of Al alloy completely from Al scrap in a selection process, thus separated aerospace Al alloy scrap is usually mixed together with few casting alloys (or wrought alloys with high Si content), resulting in excessive Si concentration in recycled aerospace Al alloy. Therefore, an attempt to remove Si from an Al melt by using an alloying method is also discussed in this thesis considering that Si is a usual impurity element in aerospace Al alloy recycling, especially for 2xxx and 7xxx Al alloy.
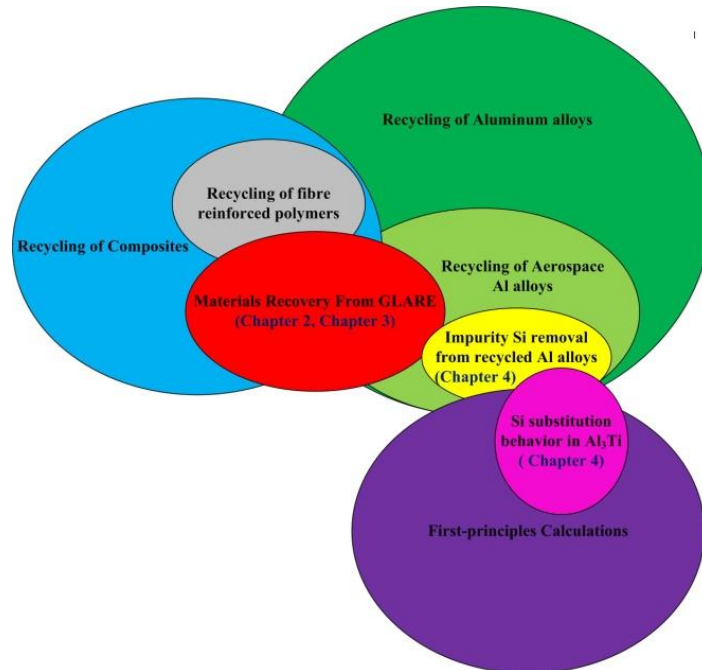
Figure 1.2 Illustration of relations of research activities presented in this thesis in connection with other related research fields.

The relations among these research activities in this thesis are shown in Figure 1.2. The cycle with red background presents the research work on materials recovery (2024 Al and S2 glass fibre) from GLARE. The cycle with yellow background presents the research work on impurity Si removal from Al melts, and first-principles calculation is employed to investigate the Si removal potential which is presented in the cycle with purple background.

This research work has a positive impact on environment, resources management and economic benefits.

1.2 Recycling of Fibre Metal Laminates (FMLs)

1.2.1 Historical overview of FMLs

Fibre-Metal-Laminates originate from metal bonding in English aircraft manufacturer De Havilland which is the first company to bond metal parts together [11]. In the 1950's metal bonding was intensively developed in the aerospace industry to avoid inter rivet buckling of thin sheets. The bonded structure showed higher (compression) strength compared with riveting, but riveting was perceived as a widely accepted industrial process [11-12]. The fatigue testing at the Fokker Company and the NLR (Nationaal Lucht- en Ruimtevaartlaboratorium) both in the Netherlands indicated that the laminated metal sheets had a favourable resistance to fatigue and also showed high damage tolerance.

In the 1970's composites were widely investigated but were very expensive. Against this situation, the combinations of metal and composites became a new idea and were studied in Great Britain and USA as a kind of intermediate between metallic and composite structure. The researcher Schliekelmann and his co-workers of Fokker found that NASA researchers were especially interested in local reinforcements bonded to aluminium structures in Space Shuttle components during a visit to the USA at the end of the seventies. This inspired researchers at Fokker to add fibres into their laminated metals. The crack growth of unidirectional carbon fibres reinforced laminates was two or three times slower than in monolithic aluminium however this was not spectacular in view of the high cost of the laminates. Delft University of Technology was involved in the optimization of the materials at the end of the seventies. Professors Schijve and Vogelesang assigned the flight simulation tests on carbon and aramid fibre reinforced laminates to student Lex ten Have in 1978. Delft student Marissen developed an analytical model for the prediction of fatigue crack growth in fibre metal laminates, based on fracture mechanics principles [11]. Other students were also involved in further optimization of fibre metal laminates in 1980. Finally, materials in fibre metal laminates were selected, are AKZO's aramid fibre, two aluminium alloys (2024 and 7475) from ALCOA and epoxy adhesive of 3M, respectively.

On 9 January 1981, the patent on Fibre Metal Laminates was field in the USA, the name of the applicant is Delft University of Technology but AKZO holds the rights. The first commercial fibre metal laminates product under the trade name Arall (ARamid fibres

reinforced ALuminium Laminates) was launched by ALCOA in 1981/1982. During the 1980's the material was further developed. The testing of Arall showed that the aramid fibres did not perform well when the laminate was subjected to compressive loads. This led to the choice of S2-Glass fibres embedded in epoxy between 2024 aluminium alloy sheets: the GLARE family (see Figure 1.3). At the same time other beneficial properties of the laminates became apparent such as the impact strength, residual strength and its fire resistance properties. A patent on GLARE was authorised on the 14th of October 1987 by AKZO with Roebroeks and Vogelesang named as inventors [11].

Figure 1.3. GLARE[8].

In the 1990's the research was focused to make GLARE ready for a major application. Especially the splicing concept was important to reduce the costs of the finished product. With splices the GLARE panels can be much larger than the size of the metal sheets. Also a lot of effort was put into quality assurance of the laminates. Airbus showed sincere interest in applying GLARE on the A3XX in the second half of the 1990's, the A3XX was under development at that time. Finally this interest resulted in the commitment of Airbus to apply GLARE in the fuselage of the A380 (as the A3XX was renamed) [13].

In April 2005 the first superjumbo airplane with application of GLARE on major structural fuselage parts, namely the A380, has flown commercially [14]. GLARE is currently produced by Cytec Engineered Materials in Wrexham, UK, who supplies it to the Airbus A380 component manufacturing facilities at Stork Fokker in the Netherlands as well as at Airbus in Nordenham, Germany. This does not mean that the fundamental research in Delft stopped. The concept of Fibre-Metal-Laminates is still under development to expand its applications.

1.2.2 Properties of GLARE

GLARE is a member of the Fibre Metal Laminate (FML) material family, and GLARE is built up of alternating metal and fibre layers. For standard GLARE, aluminium alloy

2024-T3 coated with primer BR 127, and S2-glass fibres embedded in epoxy FM 94 are bonded together to form a laminate. This stack is cured in an autoclave at 120 ℃ and 6 bar for 1 hour [15-16].

Now six different standard grades GLARE have been produced, as shown in Table 1.2. They are all based on unidirectional S-glass fibres embedded with FM 94 adhesive resulting in a 0.127 mm thick prepregs with a nominal fibre volume fraction of 59%. Different standard GLARE grades are nominated according to different stacking orientations of prepreg layer in between the aluminium alloy sheet [11]. The system is based a notation with four variables: GLARE X-X/X-X. The outer surfaces of a GLARE laminate are always aluminium alloy to prevent moisture intrusion. The first variable gives the GLARE type. The second and third variable characterizes the number of aluminium layer and prepreg layers, respectively. The last variable gives the thickness of the aluminium layers in the laminate. The direction of the fibres is given with respect to the rolling direction of the aluminium layers, whereby the rolling direction is defined as 0°, the transverse rolling direction is defined as 90°.

Table 1.2 Standard GLARE grades [11].

Grade	sub	Metal sheet thickness [mm] & alloy	Prepreg orientation in each fibre layer	Main beneficial characteristics
GLARE 1	-	0.3-0.4 7475-T761	0/0	Fatigue, strength, yield stress
GLARE 2	GLARE 2A	0.2-0.5 2024-T3	0/0	Fatigue, strength
	GLARE 2B	0.2-0.5 2024-T3	90/90	Fatigue, strength
GLARE 3	-	0.2-0.5 2024-T3	0/90	Fatigue, impact
GLARE 4	GLARE 4A	0.2-0.5 2024-T3	0/90/0	Fatigue, strength in 0° direction
	GLARE 4B	0.2-0.5 2024-T3	90/0/90	Fatigue, strength in 90° direction
GLARE 5	-	0.2-0.5 2024-T3	0/90/90/0	Impact
GLARE 6	GLARE 6A	0.2-0.5 2024-T3	+45/-45	Shear off-axis properties
	GLARE 6B	0.2-0.5 2024-T3	-45/+45	Shear off-axis properties

Figure 1.4. Partial GLARE in fuselage of Airbus A380 [17].

Weight reduction and improved damage tolerance characteristics are the two main advantages of GLARE compared to aluminium alloy. Other favourable properties are higher ultimate tensile strength, better blunt notch strength, excellent fire resistance, enhanced impact resistance, good lightning resistance and better corrosion behaviour [14]. The weight saving caused by GLARE is about 10 wt% compared to monolithic aluminium alloys [11], which is crucial to improve fuel efficiency. In 2012 about 500 m^2 GLARE is employed in each Airbus A380 [17], as shown in Figure 1.4.

1.2.3 GLARE recycling

GLARE is a laminated material consisting of thin layers of aluminium sheet (typically more than 70% in volume) and prepreg (glass fibre layers embedded in epoxy resin FM 94). The first important point for materials recovery from GLARE is to separate the prepregs and 2024 Al sheets. Thus the removal (or recycling) of FM 94 becomes the key problem required to be solved because the FM 94 worked as adhesive in this laminated material.

The prepreg is one kind of Fibre Reinforced polymers (FRPs), therefore, the state of art of FRPs recycling is introduced here.

1.2.3.1 Fibre reinforced polymers recycling

Recycling of FRPs has been intensively investigated in the past decade [18-23]. Different solutions for FRPs recycling have been studied so far, including mechanical recycling, chemical recycling and thermal recycling. Mechanical treatment through crushing and milling is relatively inexpensive and simple, but it is only able to produce short milled fibres with poor mechanical properties just can be used as filler/reinforcement materials [24-25].

Chemical recycling such as glycolysis [26] or hydrogenolysis [27] can decompose the epoxy resin into its original monomer to produce a potential chemical feedstock. Nitric acid solutions at 343–363 K can act as a reactive medium by degrading bisphenol-F epoxy resins recovering clean carbon fibres [28]. Moreover, a supercritical fluids (SCFs) method

8

has also been investigated for recycling of fibres and resins [29]. Supercritical water (SCW) is also a potential medium for the recycling of fibres and resins since low cost, recyclable, non-toxic and relatively easy to handle [30].

Table 1.3 Summary analysis of different recycling processes [10].

Methods	Advantages	Drawbacks	Progress	
			Recycler	Process scale[#]
Mechanical Recycling	–Recovery of both fibres and resins[13] –No use or production of hazardous materials	–Significant degradation of mechanical properties[13] – Unstructured. Coarse and non-consistent fibre architecture[32] –Limited possibilities for re-manufacturing	[33] [34] [35] [36] [13]	P L L L L
Chemical Recycling	–Very high retention of mechanical properties and fibre lengths[37-38] –High potential for material recovery from resin[39]	–Common reduced adhesion to polymeric resins[37] –Low contamination tolerance[39-40] –Reduced scalability of most methods[39, 41] –Possible environmental impact if hazardous solvents are used[42]	[38] [43] [44] [18]	P P L L
Thermal Recycling	A –High retention of mechanical properties –Potential to recover chemical feedstock from the resin[45] –No use of chemical solvents	–Possible deposition of char on fibre surface[31, 46] –Sensitivity of properties of recycled fibres to processing parameters[31] –Environmentally hazardous off-gases[47]	[48] [49] [50] [51] [52] [53] [54] [22]	C C C P P P P L
	B –High tolerance to contamination[55] –No presence of residual on carbon fibre surface[56] –Well established and documented process	–Strength degradation between 25% and 50% for carbon fibre, but has a limited impact on glass fibre[57] –Fibre length degradation[57-58] –Unstructured (''fluffy'') fibre architecture[13, 57] –Impossibility for material recovery from resin[58]	[59] [60] [61]	P

A - Pyrolysis, B - Oxidation atmosphere;
P - pilot scale, L - laboratory scale, C - commercial-scale, U/P - upgrade planned

Pyrolysis and fluidised bed are two important methods for thermal recycling. Pyrolysis processes [31] allow for the recovery of long high modulus fibres. Fluidised beds can operate at high temperatures under an oxidizing atmosphere to produce clean, resin-free fibres but causing a reduction in the mechanical properties of carbon fibres. The summary of different recycling methods is listed in Table 1.3.

1.2.3.2 State of the art of GLARE recycling

Two different GLARE recycling methods, mechanic recycling and thermal recycling, were carried out by Tempelman [62].

(1) Mechanical separation: The first study of GLARE recycling was carried out by Tempelman [62]. Since generation of the EOL GLARE scrap is not earlier expected than around 2045, the investigation focused on the manufacturing scrap of GLARE. Due to the large difference of thermal expansion coefficients between aluminium (2.4×10^{-5}/K) and glass fibres (0.8×10^{-5}/K), a low temperature cryogenic liberation process was employed to separate the aluminium foils from the epoxy resin and glass fibres. In the process, a granulator in the presence of liquid nitrogen at -196 ^{o}C was used to cut the GLARE scrap into small pieces with a size of 10 mm while cryogenic liberation takes place. The mixture of liberated aluminium pieces and un-separated GLARE is then processed in an Eddy Current separator. Here the liberated aluminium particles (~10 mm size) are separated from the resin, fibres and the un-liberated composites according to their differences in density and electrical conductivity. Reasonable liberation and separation efficiencies were obtained; however, different particle size requirements between cryogenic separation (granulation at maximum 10 mm) and eddy current separation (minimum 10 mm) have negative effects on the final separation and the scrap quality. From a commercialisation point of view, the cost of low temperature cryogenic liberation is high compared to the market value of the recovered materials [63].

(2) Thermal delamination: A high temperature liberation process has also been studied by Templeman [62]. He tried to destroy the epoxy resin and to delaminate the GLARE at 220 ^{o}C in an open furnace, but the delaminated aluminium was still covered with solid residues which required mechanical treatment such as sand blasting [63].

A more effective approach to GLARE recycling is required.

1.3 Aerospace aluminium alloys recycling

2024 Al alloy sheets are employed in GLARE, and separated 2024 Al sheets can be obtained after GLARE delamination. The recovery of 2024 Al alloy from GLARE scrap is attractive due to its high market value.
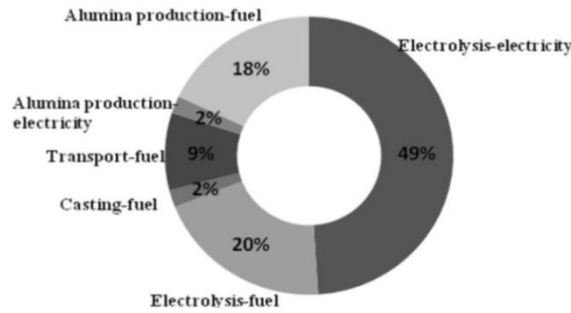
Figure 1.5. Energy consumption (113 GJ/tonne for primary aluminium production [65].
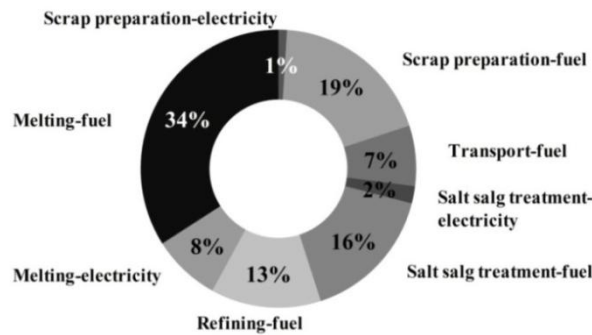
Figure 1.6. Energy consumption (13.6 GJ/tonne) for the production of aluminium from scrap [65].

The advantages of aerospace alloys recycling compared with production of primary aerospace Al alloys, are very clear and very strong [64]:

♦ *Energy saving*. The energy consumption for the production of primary aluminium from ores is huge, and the total energy input is about 113 GJ/t, as shown in Figure 1.5 [65]. Most of the energy is consumed by the molten-salt electrolysis of alumina. Direct energy usage is much lower in the production of secondary or recycled aluminium, and total energy consumption is 13.6 GJ/ton, as shown in Figure 1.6 [65].

♦ *Waste disposal reduction*. The mass of solid waste generated per tonne of recycled aluminium is 90% lower than that for primary metal [66].

♦ *Emission reduction*. Compared with the primary production, the emissions of aluminium recycling are reduced by over 90% per tonne [66].

♦ *Capital cost reduction*. The capital equipment used for recycling is less complex and thus less expensive compared to production of primary aluminium.

However, the unique compositions and performance requirements of aerospace Al alloys have resulted in very little research on the recycling of aerospace Al alloys. In order to

meet the performance requirements of aerospace Al alloy and product specifications, all aerospace alloys are produced utilizing primary metal. The typical high content of alloying elements and the very low levels of impurities to optimize toughness and other performance characteristics restrict the re-use of recycled aerospace Al alloys in non-aircraft application [67].

Recently, an appropriate new commercial scenario was developed by Das [67]:

- An aircraft-recycling centre would be established.

- As far as economically feasible, the major components of the aircraft would be disassembled and major non-aluminium components would be removed.

- As far as practically possible, the aluminium aircraft components would be pre-sorted by alloy type, most importantly by separation of 2xxx and 7xxx series alloys.

- The remaining structure would be automatically shredded, sorted, and molten to provide metal in the most valuable form for reuse.

- The recycled metal would be cast into ingot or billet of one of a useful set of high-strength aluminium alloy compositions available for a wide variety of non-fracture critical aerospace components, and subsequently fabricated into new end products that meet established performance requirements.

The composition of aerospace Al alloys can be strictly controlled by following this scenario. Then recycled aerospace Al alloys are possible to be reused in non-critical aircraft components (such as stiffeners, flaps, and other relatively low-to-moderately stressed components made of sheet, plate, or extrusions), non-aircraft application (train bodies, truck bodies, rivets and auto bumpers), as well as casting (2xx.0 and 7xx.0 series alloy, Al-Cu and Al-Zn alloy, respectively). In some cases, minor adjustment to the composition of recycled aerospace alloy is necessary to meet the re-use requirements.

The most popular solution for aluminium recycling in industry is the refining method. The refining method requires melting of the material to be recycled, casting of a billet, and then hot extrusion of the billet to form a consolidated product in wire or other forms. Several different solutions on laboratory scale have also been developed, such as the direct conversion method, powder metallurgy method as well as incorporation. The summary of advantages and drawbacks for those methods are listed in Table 1.4.

For the recycling of 2024 Al sheets obtained from GLARE scrap, the refining method is employed due to its advantages to high quality secondary aluminium combined with a concise operation.

Table 1.4. Summary of aluminium recycling methods.

Methods	Scrap	Advantages	Drawbacks	References	Process scale#
Remelting (Including Flux-free remelting and Refining)	New Old	- High quality secondary aluminium - Operation is concise and simple	- High energy cost compared with direct conversion method - Flux slag is produced during remelting and refining - Weigh loss caused by oxidation and burning	[68-72]	C
Direct conversion	*New chips*	- Low energy cost - High yield	- Poor secondary aluminium quality compared with Refining method - Limited to Casting aluminium alloy	[73-75]	L
Powder metallurgy	*New (chips and pure Al powder)*	- High yield for small size chips	- Pressure and primary aluminium powers are required in sintering to get high quality secondary aluminium -Complicated operation	[76-77]	L
Incorporation	*New Old*	- High quality secondary aluminium - Composition adjustment – Simple operation	- Flux slag is produced - High energy cost - Primary aluminium is required	[78]	L

C - commercial-scale L - laboratory scale

1.4 Thesis outline

Efforts have been made in this thesis to recycle materials from GLARE for a better sustainable society. The focus is placed on the GLARE delamination, glass fibres properties degradation as well as the yield of 2024 Al alloy after delamination. Besides, an attempt to remove Si from an Al melt by using an alloying method was also investigated considering that Si is a usual impurity element in aerospace Al alloy recycling

This thesis is constructed in the way shown in Figure 1.7, and the contents of the chapters are summarized as follows:
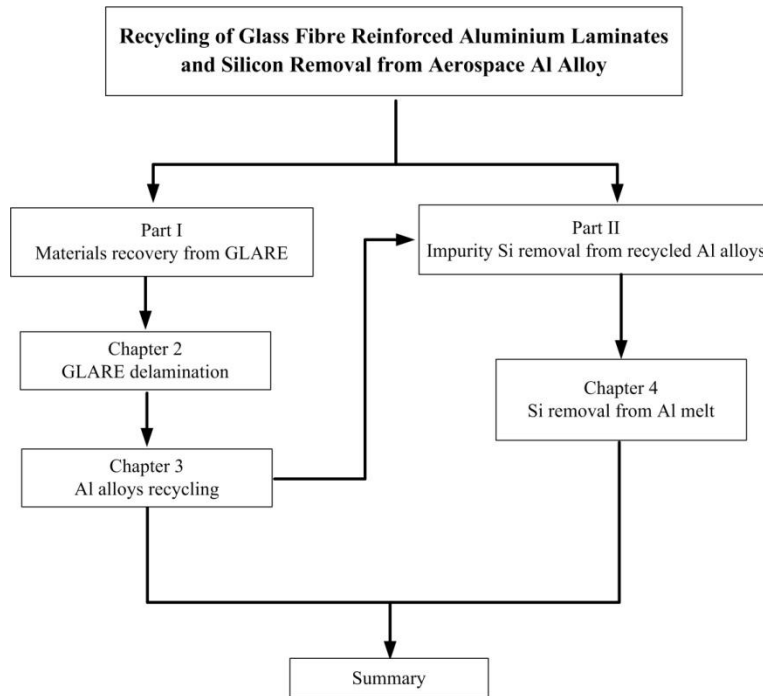
Figure 1.7. Structure of the thesis.

In ***Chapter 2***, in order to obtain an appropriate holding temperature for GLARE thermal delamination, the thermal degradation behaviour of epoxy resins in GLARE under dynamic and isothermal conditions was investigated and kinetic models were built up based on differential scanning calorimetry (DSC) and thermo gravimetric analysis (TGA). Inert and oxidising atmospheres and different heating rates are employed in the thermal analysis. The GLARE thermal delamination process is decided based on thermal analysis results and experimental optimization.

Chapter 3 primarily describes the refining of 2024 Al alloy sheets after GLARE delamination. This work was focused on the yield and quality of recycled Al alloy under

different refining conditions. High yield and satisfied Al alloy composition are preferred. The NaCl-KCl salt system was selected as main part of the flux in Al recycling and two different weight ratios of NaCl to KCl were employed, 70:30 and 44:56, respectively. Different additives are introduced into the NaCl-KCl salt system to study the effect of the flux component on the quality of Al alloy recycling. Moreover, the weight ratio of flux to Al scrap was changed in a reasonably range to obtain the optimum ratio with the aim of obtaining high quality aluminium with the minimum ratio. In industrial scale recycling, the big GLARE plane is probable cut into small pieces, therefore the influence of size of recycled Al sheets on Al refining was also discussed in this chapter. The EOL GLARE recycling was also evaluated at the end of this chapter.

Si is a usual impurity element in wrought aluminium alloys, and it will be very interesting if we can decrease its content during wrought aluminium refining. Here, an attempt to remove the impurity element Si from Al melt was studied in *Chapter 4*. We focus on impurity Si removal from an Al-Si melt with very low Si concentration, generally lower than 1 wt%, which is significant for wrought Al recycling and refining. The alloying method was considered because of treatment capacity and lower cost compared to a three-layer electrolytic purification method and a segregation method. Different Al-Si-X ternary phase diagrams were investigated by researchers in the past decades. In this research work, Ti was selected as one potential element for impurity Si removal after the evaluation of Al-Si-X ternary phase diagrams. Ti was introduced into Al-Si melt by the addition of K_2TiF_6, and $(Al,Si)_3Ti$ ternary compounds were formed with a higher melting point and higher density compared to the Al melt and therefore can be removed easily from Al melt. The influence of K_2TiF_6, holding temperature and holding time on purification efficiency were investigated. In this chapter, first-principles calculations were also used to understand and predict the structure stability of materials [79-81] and doping behaviour [82-84]. Si site preference in Al_3Ti was studied by using a first-principles calculation (based on CASTEP code-Cambridge Sequential Total Energy Package) to estimate the Si removal potential with Ti addition. The diffusion behaviour of Si in Al_3Ti was also discussed.

At last, the main outcome of this thesis research is finally presented as summary.

References

[1] Brundtland GH et.al. Our common future. Oxford publisher, UK (1987).

[2] Reh L. Challenges for progress industries in recycling. China Particuolugy 4 (2006) 47.

[3] Robèrt KH, Schmidt-Bleek B, Larderel JA, Basile G, Jansen JL, Kuehr P, Thomas PP, Hawken P, Wackernagel M. Strategic sustainable development-selection, design and synergies of applied tools. Journal of Cleaner Production 10 (2002) 197.

[4] Walker S. Sustainable by design: Explorations in theory and practice. Earthscan publisher, London, UK (2006).

[5] Pimenta P, Pinho ST. Recycling carbon fibre reinforced polymers for structural applications: Technology review and market outlook. Waste Management 31 (2011) 378.

[6] Potter K. An introduction to composite products: design, development and manufacture. Chapman & Hall publisher, London, UK (1997).

[7] Pickering SJ. Recycling technology for thermoset composite materials-current status. Composites Part A 37 (2006) 1206.

[8] Fitch PE, Cooper JS. Life cycle energy analysis as a method for material selection. Journal of Mechanical Design. Trans ASME 126 (2004) 798.

[9] Das S. JOM 52 (2000) 41.

[10] Office of industrial technologies. Energy, environmental and economics handbook. US Department of Energy (1997).

[11] Vlot A, Gunnink JW. **Fibre** Metal Laminates: An Introduction. Dordrecht: Kluwer Academic Publishers (2001).

[12] Vlot A. Glare: History of the Development of a New Aircraft Material. Kluwer Academic publishers (2001).

[13] Tjarko de Jong. Formation of Laminates. PhD thesis, Delft University of Technology (2004).

[14] Plokker HM. Crack closure in GLARE. Master thesis, Delft University of Technology (2005).

[15] Plokker HM, Alderliesten RC, Benedictus R. Crack closure in fibre metal laminates. Fatigue Fract. Eng. Mater. Struct. 30 (2007) 608-620

[16] Hinz S, Omoori T, Hojo M, Schulte K. Damage characterization of fibre metal laminates under interlaminar shear load. Composites: Part A 40 (2009) 925.

[17] http://www.premium-aerotec.com/en/Manufacturing_2.html

[18] Liu YY, Shan GH, Meng LH. Recycling of carbon fibre reinforced composites using water in subcritical conditions. Materials Science and Engineering A 520 (2009) 179.

[19] Songa YS, Younb JR, Gutowski TG. Life cycle energy analysis of fibre-reinforced composites. Composites Part A 40 (2009) 1257.

[20] Asokan P, Osmani M, Price ADF. Assessing the recycling potential of glass fibre reinforced plastic waste in concrete and cement composites. Journal of Cleaner Production 17 (2009) 821.

[21] Dang WR, Kubouchi M, Sembokuya H, Tsuda K. Chemical recycling of glass fibre reinforced epoxy resin cured with amine using nitric acid. Polymer 46 (2005) 1905.

[22] Lester E, Kingman S, Wong KH, Rudd C, Pickering S, Hilal N. Microwave heating as a means for carbon fibre recovery from polymer composites: a technical feasibility study. Materials Research Bulletin 39 (2004) 1549.

[23] Bai YP, Wang Z, Feng LQ. Chemical recycling of carbon fibres reinforced epoxy resin composites in oxygen in supercritical water. Materials and Design 31 (2010) 999.

[24] Ogi K, Shinoda T. Strength in concrete reinforced with recycled CFRP pieces. Compos Part A 36 (2005) 893.

[25] Gallet C, Kermarrec M. Molten salts: a promising lead in composites recycling. JEC Compos

22 (2006) 71.

[26] Gersifi KE, Durand G, Tersac G. Solvolysis of bisphenol A diglycidyl ether/anhydride model networks. Polymer Degradation and Stability 91 (2006) 690.

[27] Braun D, Gentzkow W, Rudolf AP. Hydrogenolytic degradation of thermosets. Polymer Degradation and Stability 74 (2001) 25.

[28] Dang W, Kubouchi M, Yamamoto S, Sembokuya H, Tsuda K. An approach to chemical recycling of epoxy resin cured with amine using nitric acid. Polymer 43 (2002) 2953.

[29] Pinero-Hernanz R, Garcia-Serna J, Dodds C, Hyde J, Poliakoff M, Cocero MJ, Kingman S, Pickering S, Lester E. Chemical recycling of carbon fibre composites using alcohols under subcritical and supercritical conditions. Journal of Supercriticcal Fluids 46 (2008) 83.

[30] Pinero-Hernanz R, Dodds C, Hyde J, Garcia-Serna J, Poliakoff M, Lester E, Cocero MJ, Kingman S, Pickering S, Wong KH. Chemical recycling of carbon fibre reinforced composites in nearcritical and supercritical water. Composites Part A 39 (2008) 454.

[31] Meyer LO, Schulte K, Grove-Nielsen E. CFRP-rcycling following a pyrolysis route: process optimization and potentials. Journal of Composite Materials 43 (2009) 1121.

[32] Palmer J, Ghita OR, Savage L, Evans KE. Successful closed-loop recycling of thermoset composites. Composites Part A 40 (2009) 490.

[33] ECRC Services Company. Official website at: http://www.ecrc-greenlabel.org

[34] Kouparitsas CE, Kartalis CN, Varelidis PC, Tsenoglou CJ, Papaspyrides CD. Recycling of the fibrous fraction of reinforced thermoset composites. Polymer Composites 23 (2002) 682.

[35] Takahashi J, Matsutsuka N, Okazumi T, Uzawa K, Ohsawa I, Yamaguchi K, Kitano A. Mechanical properties of recycled CFRP by injection molding method. In: ICCM-16, Japan Society for Composite Materials, Kyoto, Japan (2007).

[36] Ogi K, Nishikawa T, Okano Y, Taketa I. Mechanical properties of ABS resin reinforced with recycled CFRP. Advanced Composite Materials 16 (2007) 181.

[37] Jiang G, Pickering SJ, Lester EH, Turner TA, Wong KH, Warrior NA. Characterisation of carbon fibres recycled from carbon fibre/epoxy resin composites using supercritical n-propanol Composite Science Technology 69 (2009) 192.

[38] Nakagawa M, Shibata K, Kuriy H. Characterization of CFRP usingrecovered carbon fibers from waste CFRP. In: Second International Symposiumon fiber recycling. The Fiber Recycling 2009 Organizing Committee, Atlanta, Georgia, USA (2009).

[39] Marsh G. Carbon recycling: a soluble problem. Reinforced Plastics 53 (2009) 22.

[40] Gosau JM, Wesley TF, Allred RE. Recovering carbon fibre and more from scrap composite material. In: SAMPE'09 Conference, SAMPE, Baltimore, MD, USA (2009).

[41] Warrior NA, Turner TA, Pickering SJ. AFRECAR and HIRECAR Project results. In: Carbon fibre recycling and reuse 2009 Conference, IntertechPira, Hamburg, Germany (2009).

[42] Liu YY, Meng LH, Huang YD, Du JJ. Recycling of carbon/epoxy composites. Journal Applied Polymer Science 94 (2004) 1912.

[43] ATI (1994) Adherent Technologies Inc. Official website at: http://www.adherenttech.com.

[44] Hyde JR, Lester E, Kingman S, Pickering S, Wong KH. Supercritical propanol, a possible route to composite carbon fibre recovery: a viability study. Composites Part A 37 (2006) 2171.

[45] Cunliffe AM, Jones N, Williams PT. Pyrolysis of composite plastic waste. Environmental Technology 24 (2003) 653.

[46] Wong KH, Pickering SJ, Turner TA, Warrior NA. Compression moulding of a recycled carbon fibre reinforced epoxy composite. In: SAMPE'09 Conference. SAMPE, Baltimore, MD, USA (2009).

[47] Alsop SH. Pyrolysis off-gas processing. In: SAMPE'09 Conference. SAMPE, Baltimore, MD, USA (2009).

[48] RCFL. Recycled Carbon Fibre Ltd. Official website at: http://www.recycledcarbonfibre.com

[49] JCMA (2006) The Japan Carbon Fiber Manufacturers Association. Official website at: http://www.carbonfiber.gr.jp

[50] MIT, Materials Innovation Technologies, LLC. Official website at: http://www.emergingmit.com

[51] CFK. CFK Valley Stade Recycling GmbH & Co. KG. Official website at: http://www.cfk-recycling.com

[52] Karborek, Karborek S.p.a. Official website at: http://www.karborek.it/fibra

[53] Wood K. Carbon fiber reclamation: going commercial. High Performance of Composites 3 (2010) 1.

[54] HADEG. HADEG Recycling GmbH. Official website at: http://www.hadeg-recycling.de

[55] Pickering SJ, Carbon fibre recycling technologies: what goes in and what comes out? In: Carbon Fibre Recycling and Reuse 2009 Conference, IntertechPira, Hamburg, Germany (2009).

[56] Jiang G, Pickering SJ, Walker GS, Wong KH, Rudd CD. Surface characterisation of carbon fibre recycled using fluidised bed. Applied Surface Science 254 (2008) 2588.

[57] Wong KH, Pickering SJ, Turner TA, Warrior NA. Preliminary feasibility study of reinforcing potential of recycled carbon fibre for flame-retardant grade epoxy composite. In: Composites Innovation 2007 - Improved Sustainability and Environmental Performance, Net Composites, Barcelona, Spain (2007).

[58] Pickering SJ, Kelly RM, Kennerley JR, Rudd CD, Fenwick NJ. A fluidisedbed process for the recovery of glass fibres from scrap thermoset composites. Composite Science Technology 60 (2000) 509.

[59] Turner TA, Pickering SJ, Warrior NA. Development of high value composite materials using recycled carbon fibre. In: SAMPE'09 Conference. SAMPE, Baltimore, MD, USA (2009).

[60] Yip HLH, Pickering SJ, Rudd CD. Characterisation of carbon fibres recycled from scrap composites using fluidised bed process. Plastics, Rubber and Composites 31 (2002) 278.

[61] Kennerley JR, Kelly RM, Fenwick NJ, Pickering SJ, Rudd CD. The characterisation and reuse

of glass fibres recycled from scrap composites by the action of a fluidised bed process. Composites Part A 29 (1998) 839.

[62] Tempelman E. Sustainable transport and advanced materials. PhD Thesis, Delft University of Technology (1999).

[63] Yang Y, Boom R, Irion B, van Heerden DJ, Kuiper P, de Wit H. Recycling of composite materials. Chemical Engineering & Processing: Process Intensification. 51 (2012) 53.

[64] Schlesinger ME. Aluminium recycling. Taylor & Francis Group, Boca Raton, London (2007).

[65] Rombach G. Material for the future: Aluminium production and processes. DMG Business Media, Ltd., Surrey, UK (1998).

[66] Martchek KL. Life cycle benefits, challenges, and the potential of recycled aluminum. In: Proceedings of the Air and Waste Management Association 90th. Annual meeting and exhibition, Paper 97-RP124B.01 (1997).

[67] Das SK,. Kaufman JG.. Recycling aluminium aerospace alloys. Light metals, (2007) 1161.

[68] Xiao Y, Reuter MA. Recycling of distributed aluminium turning scrap. Minerals Engineering 15 (2002) 963.

[69] Xiao YP, Reuter MA, Boin U. Aluminium Recycling and Environmental Issues of Salt Slag Treatment. Journal of Environment Science and Health 40 (2005) 1861.

[70] Mashhadi HA, Moloodi A, Golestanipour M, Karimi EZV. Recycling of aluminium alloy turning scrap via cold pressing and melting with salt flux. Journal of materials processing technology 209 (2009) 3138.

[71] Tenorio JAS, Carboni MC, Espinosa DCR. Recycling of aluminium-effect of fluoride addtions on the salt viscosity and on the aluminium dissolution. Journal of Light Metals 1 (2001) 195.

[72] Reuter MA, Heiskanen K, Bion U, van Schaik A, Verhoee E, Yang Y, Georgalli G. The metrics of material and metal ecology. Elsevier, Amsterdam (2005).

[73] Tang W, Reynolds, AP. Production of wire via firction extrusion of aluminum alloy machining chips. Journal of Materials Processing Technology 210 (2010) 2231.

[74] Fogagnolo JB, Ruiz-Navas EM, Simón MA, Martinez MA. Recycling of aluminium alloy and aluminium matrix composite chips by pressing and hot extrusion. Journal of Materials Processing Technology 143-144 (2003) 792.

[75] Gronostajski J, Matuszak A. The recycling of metals by plastic deformation: an example of recycling of aluminum and its alloy chips. Journal of Materials Processing Technology 92-93 (1999) 35.

[76] Sherafat Z, Paydar, MH, Ebrahimi R. Frabrication of Al7075/Al, two phase material, by recycling Al7075 alloy chips using powder metallurgy route. Journal of Alloys and Compounds 487 (2009) 395.

[77] Samuel M. A new technique for recycling aluminium scrap. Journal of Materials Processing Technology 135 (2003) 117.

[78] Puga H, Barbosa J, Soares D, Silva F, Ribeiro S. Recycling of aluminium swarf by direct incorporation in aluminium melts. Journal of Materials Processing Technology 209 (2009) 5195.

[79] Wang JY, Zhou YC, Liao T, Zhang J, Lin ZJ. First-principles investigation of the phase stability of Ti_2AlC with Al vacancies. Scripta Materialia. 58 (2008) 227.

[80] Han YF, Dai YB,Shu D, Wang J, Sun BD. First-principles calculation on the stability of Al/TiB_2 interface. Applied Physics Letters. 89 (2006) 144107.

[81] Mishin Y, Mehl M, Papaconstantopoulos D. Phase stability in the Fe-Ni system: Investigation by first-principles calculations and atomistic simulations. Acta Materialia 53 (2005) 4029.

[82] Yu R, He LL and Ye HQ. Effect of W on structural stability of TiAl intermetallics and the site preference of W. Phys. Rev. B 65 (2002) 184102.

[83] Carara SS, Thesing LA, Piquini P. First principles study of vacancies and Al impurities in TiN. Thin Solid Films 515 (2006) 2730.

[84] Bredow T. Theoretical investigation of nitrogen substitution in cubic zirconia. Phys Rev B 75 (2007) 144102.

Chapter 2 GLARE thermal delamination

GLARE recycling consists of two steps, the first step is thermal delamination, and then the recycling of 2024 Al scrap. In this chapter, thermal delamination of GLARE is investigated. In order to obtain an appropriate holding temperature for GLARE thermal delamination, the thermal degradation behaviour of epoxy resins in GLARE under dynamic and isothermal conditions were investigated and kinetic models were built up based on differential scanning calorimetry (DSC) and thermogravimetric analysis (TGA). Application of inert and oxidising atmospheres as well as different heating rates is investigated in the thermal analysis. The GLARE thermal delamination process is determined based on thermal analysis results and experimental optimization.

21

2.1 Introduction

GLARE (GLAss fibre/epoxy REinforced aluminium laminates) is a member of the Fibre Metal Laminates family, and it has been selected as upper fuselage skin in the superjumbo Airbus A380 because of the excellent damage tolerance, fatigue resistance, flame penetration resistance and 10% weight saving compared to monolithic 2024 Al alloy [1-3]. About 500 m^2 GLARE is employed in each Airbus A380 [4]. With the increased plane orders of Airbus A380, a constant flow of End-of-Life (EOL) GLARE scrap will be generated after retiring of planes within forty years. Moreover, many tons industrial (new) GLARE scrap have been accumulated during the Airbus A380 manufacturing. Although GLARE is mainly applied in the aerospace industry and the yield of GLARE is limited compared with that of carbon fibre reinforced polymers (CFRPs), recycling of both the industrial new scrap and EOL old scrap already becomes a relevant issue and should be seriously considered.

Traditionally, in the disposal of EOL fibre-reinforced polymers, much of the polymers waste currently produced is ultimately sent to landfill [5-6], which is a poor solution for environmental impact, management of resources, and economic opportunity [7]. So it is very clear that turning GLARE waste into a valuable resource is important for the continued and sustainable use of the materials in some applications which depends on the compositions and properties of recycled materials. Different methods for fibre reinforced polymers recycling have been available (though most of them are not yet commercialized), including mechanical recycling, thermal recycling and chemical recycling [6, 8-9]. Mechanical recycling of GLARE usually leads to small pieces of aluminium alloy sheets and short glass fibres. Tempelman [10] developed a low temperature cryogenic liberation process to separate the aluminium sheets and the glass fibres/epoxy layers from GLARE, based upon the large difference of thermal expansion coefficients between glass fibres (0.8×10^{-5}/K) and aluminium (2.4×10^{-5}/K). But GLARE scrap needs to be cut into pieces of 10 mm size which causes a seriously properties degradation of glass fibres and a reduction of yield of recycled 2024 Al alloy. Chemical recycling is based on treatment in a reactive medium, such as nitric acid [11], catalytic solutions [12], alcohol [13], and some subcritical or supercritical fluids [14] etc. Comparing to general fibre reinforced polymers, the challenge in GLARE recycling is the selection of a medium reactive solution which should be inert to the aluminium alloy in GLARE. Even though a suitable medium reactive solution is found, the efficiency of chemical recycling could be limited because of the good hygroscopicity resistance of GLARE.

Thermal recycling could be a practical solution for materials recycling from GLARE scrap. GLARE thermal delamination which depends to a large extent on thermal decomposition behaviour of epoxy resins in GLARE was critical. Thermal analysis of epoxy resins under non-isothermal and isothermal conditions can provide accurate process parameters for GLARE thermal delamination. The thermal decomposition behaviour of epoxy resins at elevated temperature (non-isothermal condition) can provide detailed information for GLARE thermal delamination, e.g. initial decomposition temperature, end decomposition temperature, and relationship between decomposition degree and temperature under

different heating rates. Thermal decomposition behaviour of epoxy resins under given fixed temperatures (isothermal condition) is also important to understand the relationships between decomposition degree, holding time and decomposition rate at different decomposition temperatures.

Thermogravimetric analysis (TGA) [15-17], differential thermal analysis (DTA) and differential scanning calorimetry (DSC) [18] are often used to study non-isothermal and isothermal kinetics of epoxy resins decomposition or curing. For decomposition of epoxy resins in GLARE, non-isothermal DSC is helpful to study the range of decomposition temperature of epoxy resins, but the heat flow in the non-isothermal DSC tests is complicated due to the hybrid structure and complicated components. Mass loss is a significant criterion for the decomposition degree of epoxy resins in GLARE delamination. Change of mass can be associated with the oxidation and decomposition of epoxy resin [16]. Therefore, thermogravimetric analysis (TGA) should be more applicable to determine the parameters of kinetic models for epoxy resins decompositions in GLARE.

The aim of this chapter is to study the decomposition behaviour and kinetics of epoxy resins in GLARE under non-isothermal and isothermal conditions. Both nitrogen and air atmospheres are investigated. Firstly, DSC and TGA tests are used to identify the decomposition temperature range of epoxy resins under non-isothermal condition. Then the thermal decomposition behaviour of commercial epoxy resins in GLARE delamination under isothermal conditions is investigated by using thermogravimetric analysis. The employed temperatures for isothermal thermal analysis are decided according to the decomposition temperature range of epoxy resins obtained by the non-isothermal thermal analysis. The isothermal kinetic models are established based on the rate of mass loss of epoxy resins during thermal decomposition. Based on the thermal analysis results of epoxy resins decomposition under non-isothermal and isothermal conditions, GLARE scrap delamination at selected temperatures is performed, and the recycled 2024 Al alloy sheets are treated with ultrasonic cleaning to remove the primer residues.

2.2 Materials and experiments

2.2.1 Materials

The GLARE 3-8/7-(0.3-0.4) new scrap from the Airbus A380 window is used in this research. The GLARE new scrap consists of 8 layers 2024-T3 aluminium alloy sheets with modified epoxy phenolic primer BR 127 on both surfaces of each sheet, bonded together with 7 layers of modified epoxy film adhesive FM 94/S2-glass fibre prepreg system [1, 3, 19]. The detailed structure of the GLARE scrap is shown in Figure 2.1. The total thickness of GLARE is 4.6 mm, and the thickness of prepregs between two aluminium alloy sheets is 0.3 mm. XRF test of the modified epoxy phenolic primer BR 127 shows that certain elements such as Cu, Cr, Sr, Mn, Cl, Fe, S and Br were introduced, but unfortunately the precise concentrations of those elements in this commercial primer are unknown.

To identify different decomposition temperature regions of BR 127 and FM 94, 2024 Al

alloy sheet/BR 127 (named as Coated-Al where primer BR 127 is coated on 2024 Al sheets) and FM 94/S2-glass fibre prepreg (named as Prepreg where S2-glass fibre is pre-impregnated in FM 94 matrix) were separately cured in an autoclave at 120 ^{o}C for 1 hour.

For isothermal and non-isothermal analysis, the initial mass for each cuboid shaped GLARE, Coated-Al and Prepreg for test is taken as 60 mg. The test shows that the weight percent of epoxy in GLARE is 10 wt%, which means that the sample contains 6 mg epoxy resins.
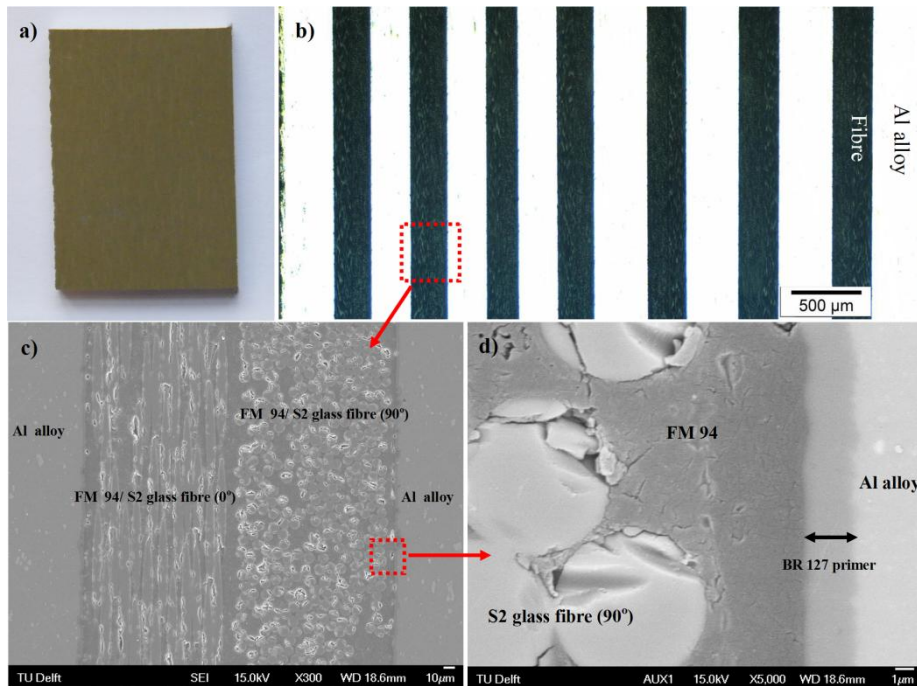
Figure 2.1. New GLARE scrap from Airbus A380 manufacturing a) front view, b) layered structure, c) and d) SEM patterns, the magnification is 300× and 5000×, respectively.

For GLARE delamination under isothermal conditions in a box furnace, the size of prepared GLARE scrap is 50 mm×35 mm×4.6 mm (Length × Width × Thickness) and the weight is about 20 g.

2.2.2 Experiments

2.2.2.1 Thermal analysis under non-isothermal condition

All mass change and heat flow curves of GLARE, Coated-Al and Prepreg under non-isothermal condition were obtained using a simultaneous thermal analysis NETZSCH STA 409 which comprises both thermogravimetric analysis (TGA) and differential scanning

calorimeter (DSC) in dry nitrogen or air atmosphere at a flow rate of 100 ml min^{-1}. To identify the initial decomposition temperatures of two different commercial epoxy resins during GLARE delamination, the cured Coated-Al and Prepreg were separately heated up to 600 $^{\circ}$C at a heating rate of 5 $^{\circ}$C min^{-1} in nitrogen or air atmosphere. According to the decomposition temperatures of Coated-Al and Prepreg, GLARE samples were heated up from ambient temperature to 600 $^{\circ}$C at a rate of 1, 2, 5 $^{\circ}$C min^{-1} in nitrogen, but were only heated up from ambient temperature to 500 $^{\circ}$C at a rate of 1, 2, 5 $^{\circ}$C min^{-1} in air atmosphere due to a lower start melting temperature (502 $^{\circ}$C) [20] of 2024 Al alloy. The decomposition result of Coated-Al and Prepreg indicated that 500 $^{\circ}$C is high enough for GLARE thermal analysis in air.

2.2.2.2 Thermal analysis under isothermal condition

Mass changes of GLARE under isothermal condition in dry nitrogen or air atmosphere were obtained by using TG device (SETSYS Evolution-1750, SETARAM). The TG device was heated from the ambient temperature to the given temperature at a heating rate of 90 °C min^{-1}. The sample was put in an Al_2O_3 crucible which was connected to a fine Al_2O_3 rod, which was slowly inserted into the furnace. Total holding time for isothermal treatment is 3 hours, and then cooled down to room temperature in furnace without heating power. The gas conditions of the furnace during the whole treatment process were set up as 100 ml min^{-1} N_2 for inert condition or 80 ml min^{-1} N_2 and 20 ml min^{-1} O_2 for simulating a flow of air where N_2 and O_2 was mixed firstly before using.

2.2.2.3 GLARE thermal delamination

The thermal delamination of GLARE scrap was carried out in a Carbolite electric resistance furnace under air atmosphere, and the delamination temperature was decided based on the thermal analysis results of resins decomposition. After thermal delamination, obtained 2024 Al alloy sheets were cleaned by ultrasonic treatment (BRANSON 5510- 40 KHz) in water for 3 minutes to be ready for characterization and further metallurgical refining.

2.2.3 Isothermal decomposition kinetics

Two general categories of kinetic models are used in the thermal analysis of resin decomposition: *n*th-order and autocatalytic.

The equations of *n*th-order reaction are described as follows [21-23]:

$$\frac{d\alpha}{dt} = k(T)f(\alpha) \tag{2-1}$$

$$k(T) = A\exp\left(\frac{-E_a}{RT}\right) \tag{2-2}$$

$$f(\alpha) = (1-\alpha)^n \qquad (2\text{-}3)$$

Where α is the decomposition degree, t is decomposition time (s), da/dt is the decomposition rate, T is decomposition temperature (K), $k(T)$ is the rate constant (s^{-1}), $f(\alpha)$ is the reaction model, A is the pre-exponential factor, E_a is the activation energy (J mol^{-1}), R is the universal gas constant, and n is reaction order.

According to equations (2-1), (2-2) and (2-3), the final equation of nth-order kinetic model can be written as:

$$\frac{d\alpha}{dt} = A \exp(-\frac{E_a}{RT})(1-\alpha)^n \qquad (2\text{-}4)$$

Systems obeying an nth-order kinetics model will obviously reach the maximum reaction rate at the beginning of the decomposition (t=0).

In this research, the decomposition degree α is defined as [24-25]:

$$\alpha = \frac{m_i - m}{m_i - m_e} \qquad (2\text{-}5)$$

where m_i, m, and m_e are the mass of epoxy resins before, during in and after decomposition process, respectively.

Under an isothermal condition, the parameters A, E_a and n can be obtained through two steps linear regression analysis by using the equations (2-6) and (2-7) which are modified from equations (2-4) and (2-2), respectively:

$$\ln(\frac{d\alpha}{dt}) = n \ln(1-\alpha) + \ln k \qquad (2\text{-}6)$$

$$\ln k = \ln A - \frac{E_a}{RT} \qquad (2\text{-}7)$$

For autocatalytic reaction, the function $f(\alpha)$ has the following form [26-27]:

$$f(\alpha) = \alpha^m (1-\alpha)^n \qquad (2\text{-}8)$$

Therefore, the equation for an autocatalytic kinetic model can be written as:

$$\frac{d\alpha}{dt} = A \exp(-\frac{E_a}{RT})\alpha^m (1-\alpha)^n \qquad (2\text{-}9)$$

where m is also a reaction order. The more accurate description should be as follows [28-29]:

$$\frac{d\alpha}{dt} = (k_1 + k_2\alpha^m)(1-\alpha)^n \tag{2-10}$$

where k_1, k_2 are the rate constants (s^{-1}), and $k_1 = (d\alpha/dt)$ at $t = 0$. The maximum decomposition rate appears at about 10-40% of decomposition for an autocatalytic reaction [23].

Under an isothermal condition, the constant k_1 can be obtained as the initial decomposition rate when decomposition degree α is zero. In order to calculate other parameters k_2, m and n, the equation (2-10) can be rearranged in the following forms:

$$\ln(\frac{d\alpha}{dt}) = n\ln(1-\alpha) + \ln(k_1 + k_2\alpha^m) \tag{2-11}$$

$$\ln\left\{\left[\left(\frac{d\alpha}{dt}\right)/(1-\alpha)^n\right] - k_1\right\} = m\ln\alpha + \ln k_2 \tag{2-12}$$

$$\ln\left(\frac{d\alpha}{dt}\right) - \ln(k_1 + k_2\alpha^m) = n\ln(1-\alpha) \tag{2-13}$$

Firstly, we can assume that the reaction order n can be determined according to the slope of a plot of $\ln(d\alpha/dt)$ versus $\ln(1-\alpha)$, as described in equation (2-11). Then, the reaction order m and the constant k_2 can be calculated from the slope and the intercept of a plot of $\ln\left\{[(d\alpha/dt)/(1-\alpha)^n] - k_1\right\}$ versus $\ln\alpha$ by using the obtained parameters k_1 and n, as presented in equation (2-12). More precise values of parameters are possible when an iterative procedure is used. The new refined parameter n can be determined from equation (2-13) after using the previously obtained k_1, k_2 and m values. The new n can be applied to the equation (2-12) to obtain new values of k_2 and m. The iterative procedure can be repeated until the values of parameters are tending toward stability.

Moreover, all the parameters A, E_a and n in nth-order model and parameters k_1, k_2, m and n in an autocatalytic model can also be obtained by using the function "Non-linear Curve Fit" in software ORIGIN or MATLAB, with introduced kinetic equations. The precision of obtained parameters by software ORIGIN or MATLAB should also be good.

2.3 Results and discussion

2.3.1 Thermal analysis under non-isothermal and isothermal conditions

2.3.1.1 Non-isothermal condition

The non-isothermal DSC tests for GLARE, Prepreg and Coated-Al are separately

investigated in nitrogen and air atmospheres to understand the decomposition behaviour of FM 94 and BR 127 during GLARE delamination. The results are shown in Figures 2.2 and 2.3. Considering that the softening point of S2-glass fibre is 1506 ^{o}C (much higher than 600 ^{o}C), the heat flow of Prepreg in Figure 2.2 and 2.3 is completely caused by the decomposition of FM 94. For Coated-Al system, the nominal melting temperature of 2024 Al alloy is between 502 ^{o}C and 638 ^{o}C, and this is why an endothermic peak occurred at 502 ^{o}C. Therefore, the heat flow of Coated-Al is primarily caused by the decomposition of BR 127 at temperatures below 502 ^{o}C. The heat change caused by oxidation of 2024 Al alloy under air atmosphere is negligible when the temperature is below 502 ^{o}C because of the protection of the existing Al_2O_3 films on the surface of Al sheets.
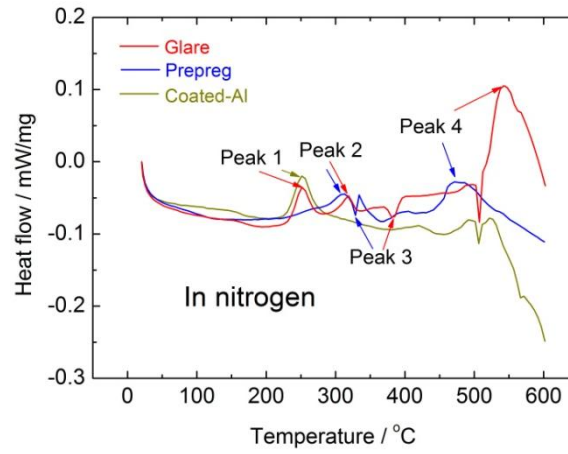

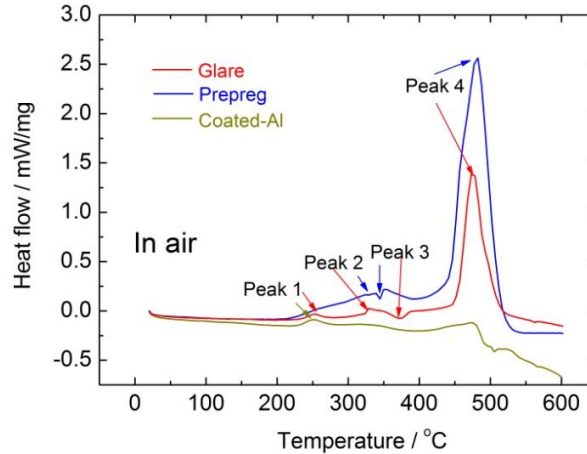*Figure 2.2. DSC curves of GLARE, Prepreg and Coated-Al in nitrogen, the heating rate for all tests are 5 ^{o}C min^{-1}.*

Figure 2.3. DSC curves of GLARE, Prepreg and Coated-Al in air, the heating rate for all tests are 5 ^{o}C min^{-1}.

Four peaks (excluding the endothermic peak around 502 ^{o}C caused by Al oxidation) caused by epoxy decomposition can be observed (Figure 2.2 and 2.3) in heat flow of GLARE under both nitrogen and air atmospheres, including three exothermic peaks and one endothermic peak. By comparing the heat flow of GLARE and BR 127 in nitrogen and air atmospheres, it is obvious that the formation of first exothermic peak (step 1) of GLARE is caused by the decomposition of epoxy BR 127 and the initial decomposition temperature of BR 127 in air is about 225 ^{o}C with the heating rate of 5 ^{o}C min^{-1}. One small exothermic peak (step 2), one endothermic peak (step 3) and one large exothermic peak (step 4) can be observed in the heat flow curves of FM 94 decomposition under both atmospheres, especially in air. It is clear that the heat flow of step 4 in air is more intensive than that in nitrogen. The initial decomposition temperatures of each step of FM 94 are about 290 ^{o}C, 345 ^{o}C and 405 ^{o}C, respectively in air when the heating rate is 5 ^{o}C min^{-1}. Though we did not test the decomposition products due to restricted functioning of our equipment, but the possible reason for the occurrence of the exothermic peak of step 2 is the thermal decomposition of secondary alcohol groups (generated during curing) and the dehydration of FM 94 according to the general decomposition sequence of epoxy resins. Then the further pyrolysis of the dehydrated structure of FM 94 contributes to the endothermic peak of step 3. At last, the exothermic reactions between decomposition products and oxygen contribute to the formation of the large exothermic peak of step 4. The difference between the decomposition behaviour of BR 127 and FM 94 may be attributed to the different structure and molecular formula. However, the decomposition products in each step should be further investigated to better understand the decomposition behaviour of BR 127 and FM 94.

Figure 2.4 and 2.5 show the mass loss and DSC heat curves of GLARE in the non-isothermal simultaneous thermal analysis (STA) with different heating rates. With higher heating rate, there is not enough time for epoxy resins decomposition due to the low thermal conductivity of GLARE, and the decomposition moves to the higher temperature region. The decomposition is more intensive under higher temperature, resulting in a higher endothermic/exothermic peak height. As mentioned before, the total percentage of epoxy in GLARE is 10 wt% which is consistent with a final mass loss of GLARE in air at a heating rate of 1 ^{o}C min^{-1}. Thus the conversion (decomposition degree) of epoxy under different non-isothermal conditions can be calculated, which is presented in Figures 2.6 and 2.7. The conversion of epoxy resins decreases at higher heating rate when samples are heated to the same maximum temperature, and this is due to the hysteretic decomposition at higher heating rate. It is obvious that the final conversion of epoxy resins in air is bigger than that in nitrogen at the same heating rate. Epoxy resins conversions are 75% and 100% in nitrogen and air at 500 ^{o}C with the heating rate of 1 ^{o}C min^{-1}, respectively. The decomposition conversion of resin is just 90% though the sample is heated up to 600 ^{o}C in nitrogen with a heating rate of 1 ^{o}C min^{-1} which is obviously incomplete. Therefore, an oxidising atmosphere should be more beneficial to the epoxy resins decomposition compared to an inert atmosphere.

As can be seen in Figure 2.4 and 2.5, the exothermic peak of step 4 in air is more intensive than that in nitrogen, and the released heat can be used for thermal delamination. Thus an oxidising atmosphere is more helpful to energy saving compared to a nitrogen atmosphere.

Furthermore, most of the off-gas generated during thermal delamination should in theory be carbon dioxide and water vapour in air if the decomposition products of epoxy can completely react with oxygen and those reactions also can supply heat for thermal delamination. But a more deleterious off-gas is generated in a nitrogen atmosphere, such as methane, ethane and acetone.
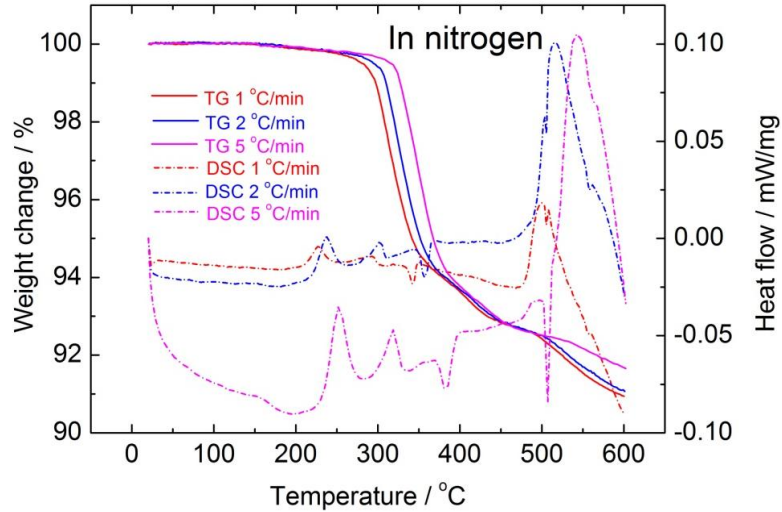
Figure 2.4. Effect of heating rate on weight change and heat flow of GLARE delamination in nitrogen.
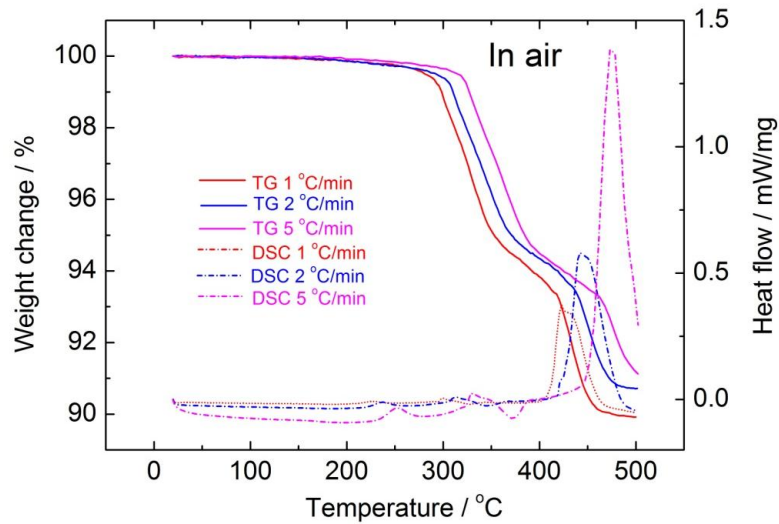
Figure 2.5. Effect of heating rate on weight change and heat flow of GLARE delamination in air.
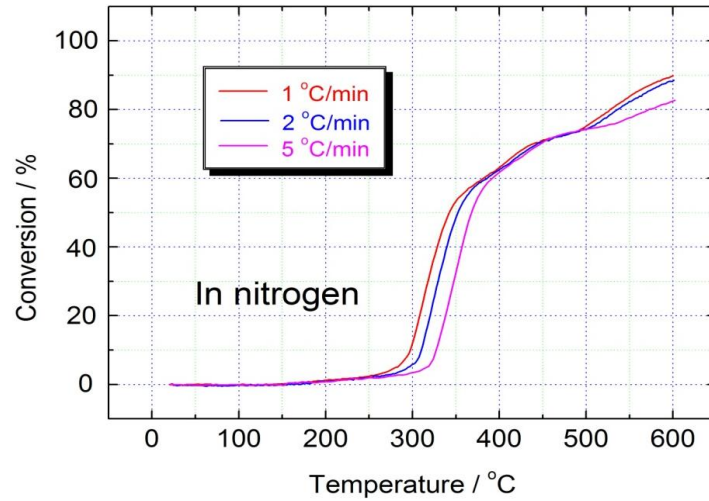
Figure 2.6. Effect of heating rate on conversion of epoxy resins decomposition in GLARE under nitrogen atmosphere.
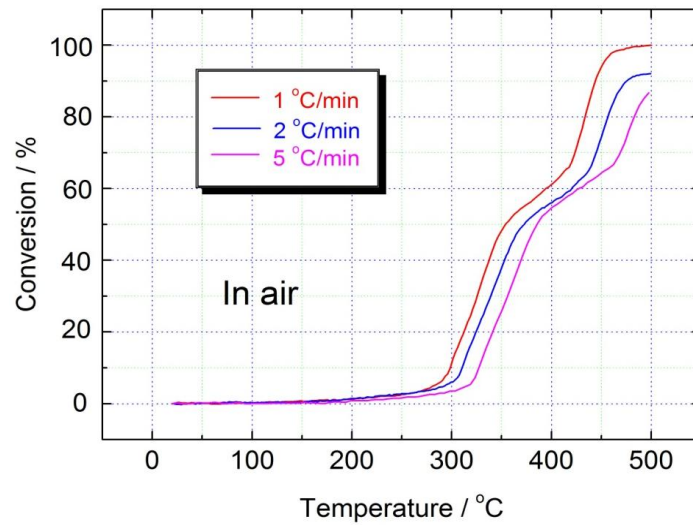
Figure 2.7. Effect of heating rate on conversion of epoxy resins decomposition in GLARE under air atmosphere.

The details of epoxy decomposition of GLARE in each step under both atmospheres were also investigated to better understand the influence of heating rate and atmosphere. They are listed in Tables 2.1 and 2.2.

Table 2.1. Initial decomposition temperatures (T_i / ^oC) and temperature at maximum decomposition ratio (T_m/^oC) for each step under non-isothermal condition in nitrogen and air.

Heating rate / ^oC min^{-1}		Step 1		Step 2		Step 3		Step 4	
		T_i	T_m	T_i	T_m	T_i	T_m	T_i	T_m
Nitrogen	1	188	227	255	293	311	341	354	500
	2	210	238	262	301	317	356	368	516
	5	223	251	282	319	334	380	406	543
Air	1	188	227	255	298	318	326	356	423
	2	212	238	260	313	330	344	388	442
	5	225	251	288	329	344	371	408	473

Table 2.2. Mass loss of epoxy resins decomposition in each step under non-isothermal condition in nitrogen (from 20 ^oC to 600 ^oC) and air atmospheres (from 20 ^oC to 500 ^oC).

Heating rate / ^oC min^{-1}		Mass loss / wt%				
		Step 1	Step 2	Step 3	Step 4	Total
Nitrogen	1	2.6	20.2	31.8	35.2	89.8
	2	2.8	14.9	39.0	31.8	88.5
	5	2.8	13.5	46.6	19.8	82.7
Air	1	2.8	21.6	26.4	49.2	100.0
	2	2.9	20.8	30.4	38.0	92.1
	5	2.8	19.5	32.5	31.9	86.7

The steps are defined according to the heat flow peaks. The mass loss in Table 2.2 describes the decomposition degree when the temperature increased from the initial decomposition temperature of this step to the initial decomposition temperature of the next step. It should be noticed that all end temperatures for tests in air are 500 ^oC to avoid the influence of a drastic oxidation of Al alloy on heat curve and mass change when the temperature is higher than the start melting temperature (502 ^oC). As can be seen in Table 2.1, the initial decomposition temperatures T_i and the temperature T_m at the maximum conversion rate of BR 127 (step 1) are very close in both atmospheres at the same heating rate. Furthermore, the mass loss of step 1 is also the same in both atmospheres at different heating rates, as

listed in Table 2.2. Therefore, the decomposition behaviour of BR 127 in air should be similar to that in nitrogen under non-isothermal condition. Just the initial decomposition temperature is enhanced from 188 to 225 $^{\circ}$C when the heating rate is increased from 1 to 5 $^{\circ}$C min^{-1}. The decomposition behaviour of FM 94 is more complex and it was described in steps 2-4 for both atmospheres. All T_i and T_m of steps 2-4 are enhanced with the increasing of heating rate in both atmospheres. Different from steps 2 and 4, the mass loss of step 3 is increased with increasing heating rate in both atmospheres, and the mass loss of step 3 in nitrogen is bigger than that in air. As mentioned before, the endothermic peak of step 3 is attributed to the pyrolysis of dehydrated structure of FM 94, oxygen is not involved in the pyrolysis reaction, may be nitrogen is more helpful to this pyrolysis process resulting in bigger mass loss in step 3. However, the total conversion of epoxy resins in air is bigger than that in nitrogen when the same heating rate is employed though the end temperature in air is 100 $^{\circ}$C lower.

2.3.1.2 Isothermal condition

The results of the thermal analysis under non-isothermal conditions indicated that there are four steps during the epoxy resins decomposition in GLARE. In order to better understand the decomposition behaviour, the analysis of isothermal kinetics was studied under different temperatures, which are selected according to the initial decomposition temperature of each step in air at 1 $^{\circ}$C min^{-1} heating rate (see Table 2.1). The given temperatures are 230 $^{\circ}$C, 310 $^{\circ}$C, 350 $^{\circ}$C and 450 $^{\circ}$C, respectively.

Figure 2.8 and 2.9 show the isothermal decomposition curves of epoxy resins of GLARE at different temperatures in nitrogen and air. The final conversion is enhanced with isothermal temperature. The decomposition percentage is 4.4% and 7.2% at 230 $^{\circ}$C for 3 hours when the decomposition atmosphere is nitrogen and air, respectively. According to the conversion curves in nitrogen and air at 230 $^{\circ}$C, it is obvious that the oxidising atmosphere can accelerate the decomposition of epoxy BR 127 compared to an inert atmosphere. As we can see in Figures 2.8 and 2.9, at 310 $^{\circ}$C, both conversions in nitrogen and air atmospheres are increased with increasing isothermal holding time through the entire 3 hours, and the final conversion is 48.4% and 43.4% in nitrogen and air, respectively, which may be attributed to the more efficient pyrolysis of step 3 in nitrogen compared to that in air. The final conversion at 350 $^{\circ}$C after 3 hours is increased to 57.8% and 69.4%, respectively in nitrogen and air. All epoxy resins in GLARE can be completely decomposed at 450 $^{\circ}$C, the required time is respectively 100 and 70 min in nitrogen and air. In general, an oxidising atmosphere is more preferred for epoxy resins decomposition compared to inert atmosphere.

Figure 2.8. Conversion versus. time at different isothermal temperatures for epoxy resins decompositions in GLARE under nitrogen atmosphere.
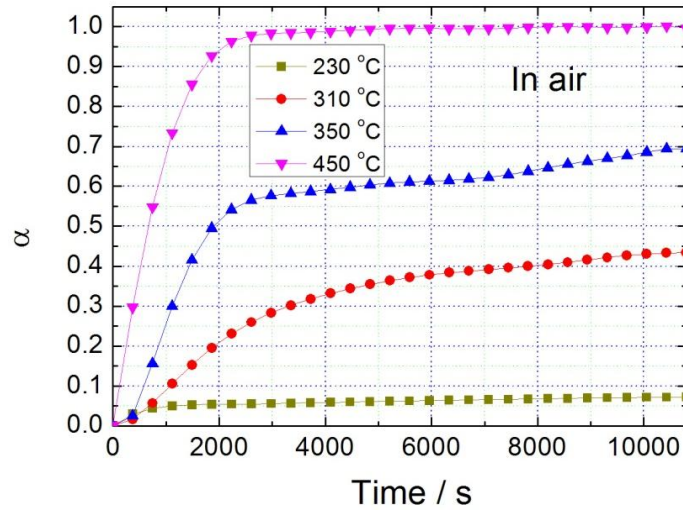
Figure 2.9. Conversion versus. time at different isothermal temperatures for epoxy resins decompositions in GLARE under air atmosphere.

The curves of the conversion rate as a function of time are shown in Figure 2.10 and 2.11. It can be seen that the peak values of the conversion rate increased with the isothermal temperature, especially at higher temperature range. But, the discrepancy of maximum conversion rates caused by different atmospheres is negligible though the final conversion in air is higher than that in nitrogen.
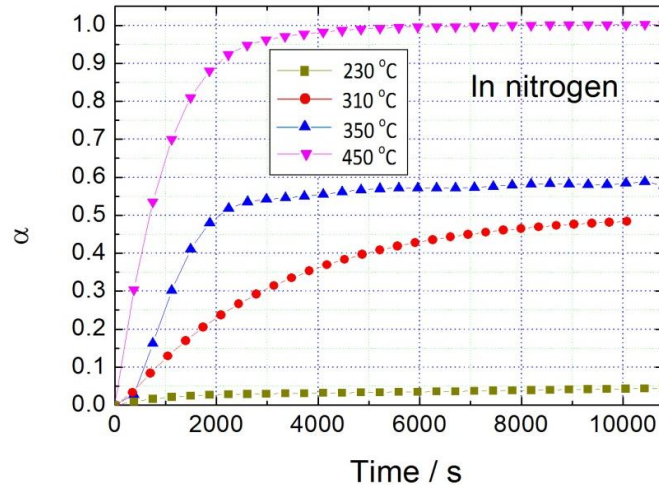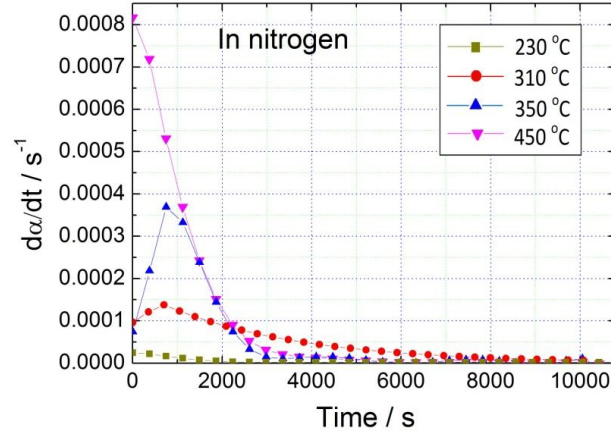
Figure 2.10. Conversion rate versus. time at different isothermal temperatures for epoxy resins decompositions in GLARE under nitrogen atmosphere.
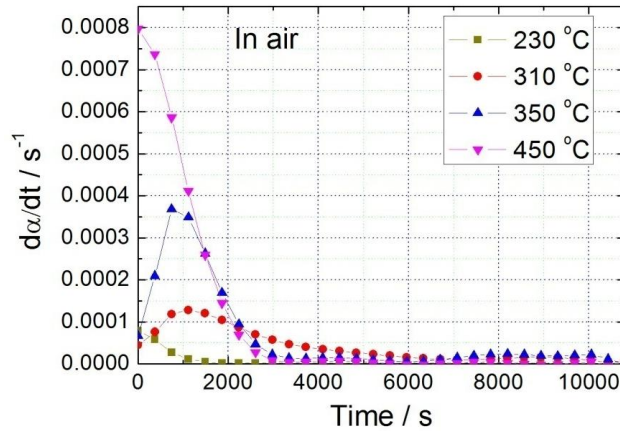
Figure 2.11. Conversion rate versus. time at different isothermal temperatures for epoxy resins decompositions in GLARE under air atmosphere.

The conversion rate (as a function of conversion of epoxy resins) at different temperatures in nitrogen and air are shown in Figure 2.12 and 2.13 (symbols), respectively. As can be seen in Figure 2.12 and 2.13, the decomposition behaviour at 230 ^{o}C and 450 ^{o}C in nitrogen and air follows the *n*th-order mechanism with a maximum conversion rate at the beginning of decomposition. The decomposition behaviour at 310 ^{o}C and 350 ^{o}C in nitrogen and air proceed through an autocatalytic mechanism, and the maximum conversion rates occur in the 10-25% conversion region. The isothermal holding temperatures are selected according to the initial temperatures of four different steps which are defined based on the heat flow under dynamic condition. At 230 ^{o}C, the main conversion is attributed to the reaction

35

presented as the step 1 in the dynamic thermal analysis. Similarly, conversion at 310 ^{o}C are attributed to steps 1-2, conversion at 350 ^{o}C are attributed to steps 1-3, and conversion at 450 ^{o}C are attributed to steps 1-4. Thus the resins decomposed in 3 hours are much different at different isothermal holding temperature, leading to two different decomposition mechanisms.

Figure 2.12. Comparison of experimental (symbols) and theoretical (lines) conversion rate versus conversion at different isothermal temperatures for epoxy resins decomposition in nitrogen.

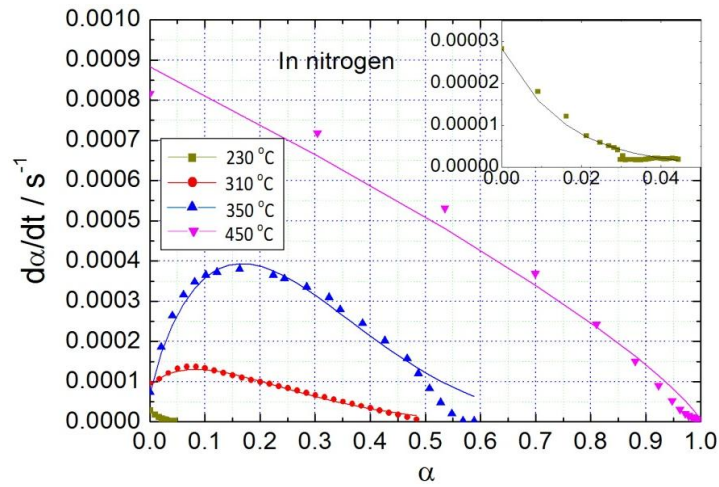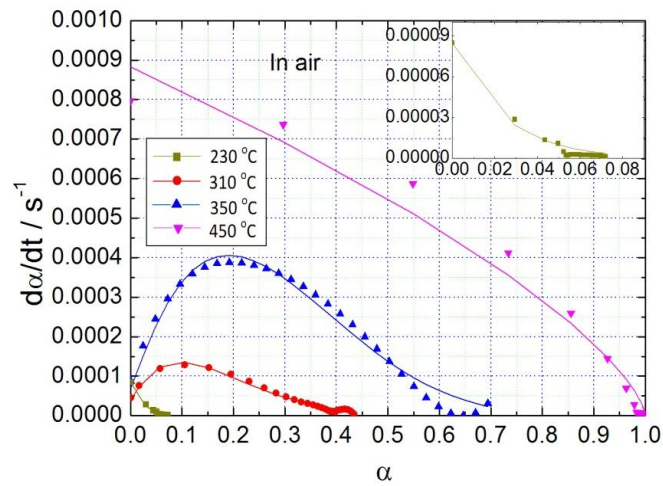

Figure 2.13. Comparison of experimental (symbols) and theoretical (lines) conversion rate versus conversion at different isothermal temperatures for epoxy resins decomposition in air.

The parameters of the kinetic models are obtained after regression based on the equations (2-4) and (2-10) and are listed in Table 2.3.

For the nth-order decomposition mechanism (at 230 $^{\circ}$C and 450 $^{\circ}$C), the activation energies in nitrogen atmosphere are little lower in comparison to those in air atmosphere at the same holding temperature, but the initial conversion rates k (maximum conversion rate) in air are higher compared to those in nitrogen, especially at 230 $^{\circ}$C. It is consistent with previous dynamic thermal analysis results. As we can see in Table 2.1, the required start temperature for step 1 and step 4 in nitrogen is little lower than that in air, indicating that the decomposition should be little easier in nitrogen compared to decomposition in air, at 230 $^{\circ}$C and 450 $^{\circ}$C. But the conversion in air is higher than that in nitrogen at 230 $^{\circ}$C for 3 hours, and the needed time for complete decomposition in air is shorter than that in nitrogen at 450 $^{\circ}$C, as shown in Figures 2.8 and 2.9. For the autocatalytic decomposition mechanism (at 310 $^{\circ}$C and 350 $^{\circ}$C), both constants k_1 and k_2 obey the Arrhenius form (equation 2-2). The constant k_1 governs the early stage autocatalytic reaction and the term $k_2\alpha^m$ represents the effect of the reaction products on the conversion rate [30-31]. Thus, according to the obtained parameters in Table 2.3, the values of $k_2\alpha^m$ in air are obviously stronger than those in nitrogen, indicating that the effect of reaction products on conversion rate is more significant within an oxidising atmosphere.

The comparison of the experimental data with the decomposition rates obtained from the kinetic models is presented in Figure 2.12 and 2.13. It is clear that most of the predicted values agree with the experimental data.

Table 2.3. Parameters of kinetic models for epoxy resin decomposition at four temperatures.

Atmosphere	Temperature °C	nth-order				Autocatalytic			
		E_a / KJ	A / $\times 10^3$	$k = A \times exp(-E_a/RT)$ / $\times 10^{-5}$	n	k_1 / $\times 10^{-5}$	k_2 / $\times 10^{-3}$	m	n
Nitrogen	230	84.08	15.24	2.83	63.15	/	/	/	/
	310	/	/	/	/	9	1.13	0.89	5.67
	350	/	/	/	/	7	3.80	0.89	4.11
	450	112.92	126.99	88.28	0.80	/	/	/	/
Air	230	85.66	66.31	8.44	42.12	/	/	/	/
	310	/	/	/	/	4	3.13	1.03	8.46
	350	/	/	/	/	7	5.83	1.10	4.34
	450	114.18	156.67	88.31	0.68	/	/	/	/

2.3.2 GLARE delamination

2.3.2.1 Delamination experiments

The thermal analysis of epoxy resins decomposition under non-isothermal and isothermal conditions provide useful information for optimization of process parameters of GLARE thermal delamination. It is obvious that an oxidising atmosphere is more preferred for GLARE delamination. Different from thermal analysis where the mass of GLARE sample is only 0.06 gram, a longer holding time would be required for large-sized GLARE scrap delamination because of the influence of kinetic factors, such as scrap size and air convection. An appropriate holding temperature is important for GLARE thermal delamination with high efficiency. The holding temperature should be high enough to ensure that epoxy resins can be completely decomposed at this temperature while avoiding the oxidation of 2024 Al alloy. Based on previous non-isothermal analysis results for epoxy resins decomposition in air (Figure 2.9), the suitable holding temperature for GLARE delamination should be selected in between 450 $^{\circ}$C and 502 $^{\circ}$C (start melting temperature of 2024 Al alloy).

In order to determine the optimum holding temperature for GLARE delamination, four different holding temperatures were investigated, 440 $^{\circ}$C, 460 $^{\circ}$C, 480 $^{\circ}$C and 500 $^{\circ}$C, respectively. GLARE delamination experiments were conducted in an electric resistance furnace under air atmosphere and Figures 2.14-2.17 show the results. As we can see in the Figures 2.14-2.17, the Al sheets and S2-glass fibre were well separated after thermal delamination even though the holding temperature was just 440 $^{\circ}$C. The results also show that some oxidation spots occur on the surface of Al sheets when the holding temperature was 500 $^{\circ}$C, as shown in Figure 2.17. A strong exothermic peak can be found in DSC curves of GLARE in air at about 450 $^{\circ}$C (Figures 2.3 and 2.5) which causes the temperature around the Al sheet to be higher than the preset furnace temperature of 500 $^{\circ}$C. The real temperature in the furnace should be close to the aluminium alloy start melting point, resulting in plenty of oxidation spots on the Al sheets. It can be concluded that 500 $^{\circ}$C is a little too high for GLARE thermal delamination.

Figure 2.14. GLARE delamination in air at 440 °C. The holding time is a) 30 min, b) 60 min, c) 90 min, d) 120 min, e) 150 min, f) 180 min and g) 210 min, respectively.

Figure 2.15. GLARE delamination in air at 460 °C. The holding time is a) 30 min, b) 60 min, c) 90 min, d) 120 min, e) 150 min and f) 180 min, respectively.
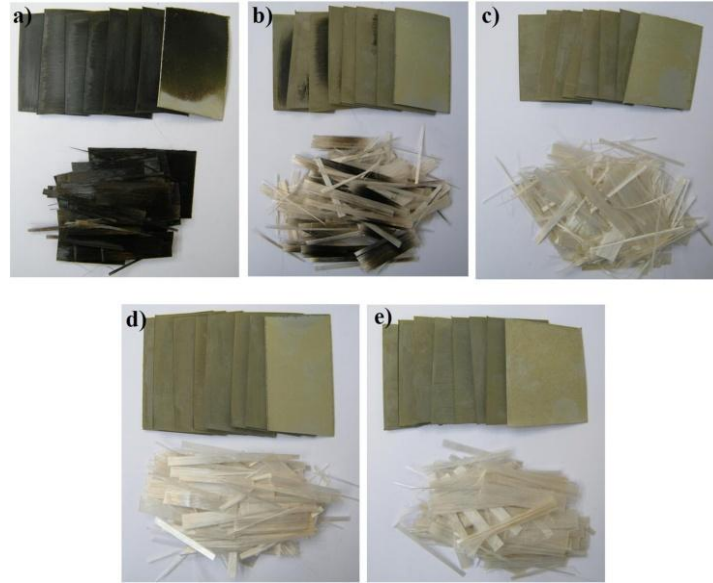
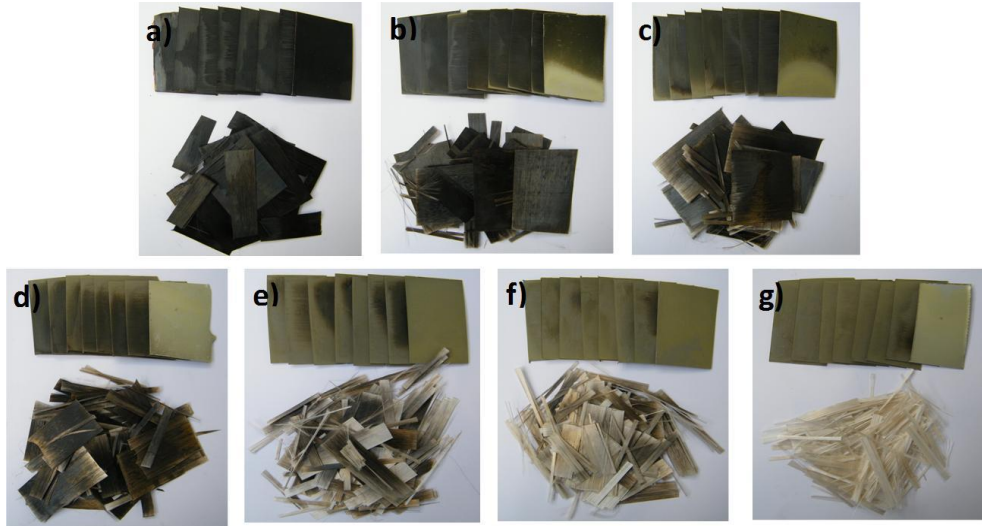*Figure 2.16. GLARE delamination in air at 480 °C. The holding time is a) 30 min, b) 90 min, c) 120 min, d) 150 min and e) 180 min, respectively.*

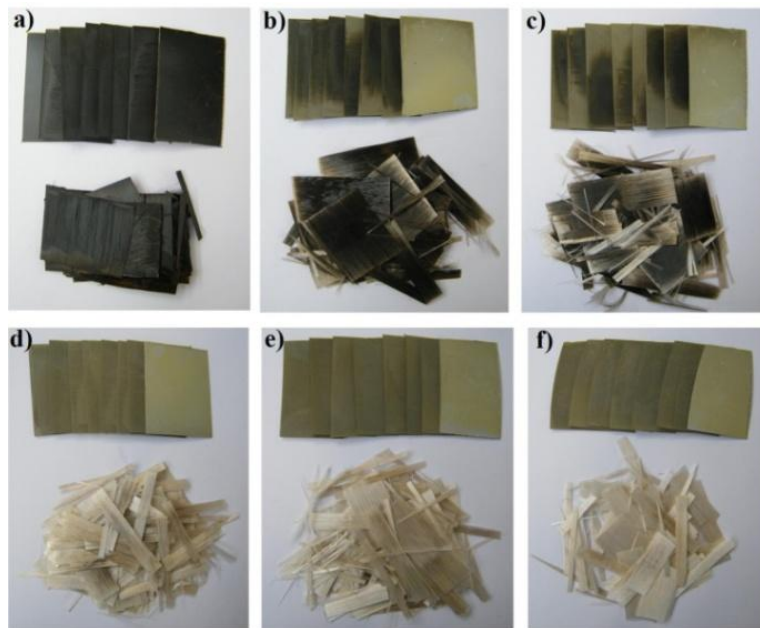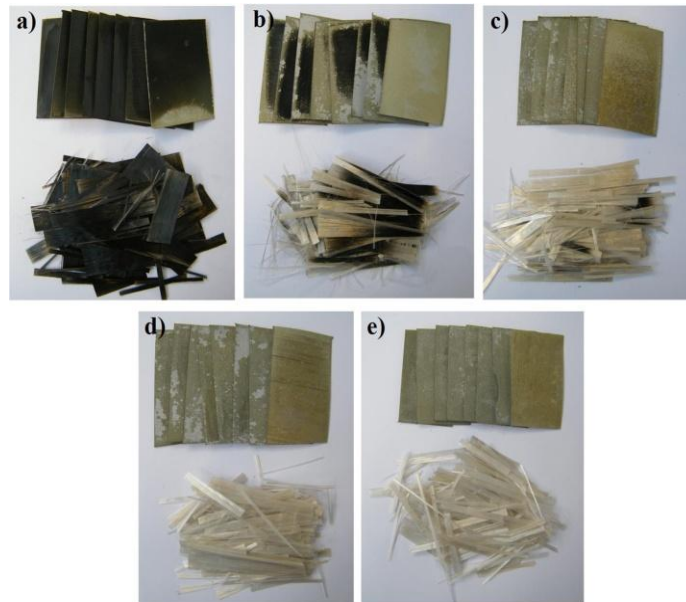*Figure 2.17. GLARE delamination in air at 500 °C. The holding time is a) 30 min, b) 60 min, c) 90 min, d) 120 min and e) 150 min, respectively.*

The weight changes of GLARE during delamination are shown in Figure 2.18. The required holding time for complete delamination of GLARE is decreased with increasing holding temperature. The delamination processes is finished after 120 min when the temperature is 480 $^\circ$C, but the required holding time increases to 210 min at a lower temperature of 440 $^\circ$C. The weight of GLARE is increased with holding time after 90 min at 500 $^\circ$C which is attributed to the oxidation of 2024 Al.

According to the results of GLARE delamination, the appropriate delamination process is found to be at holding temperature of 480 $^\circ$C for 120 min.
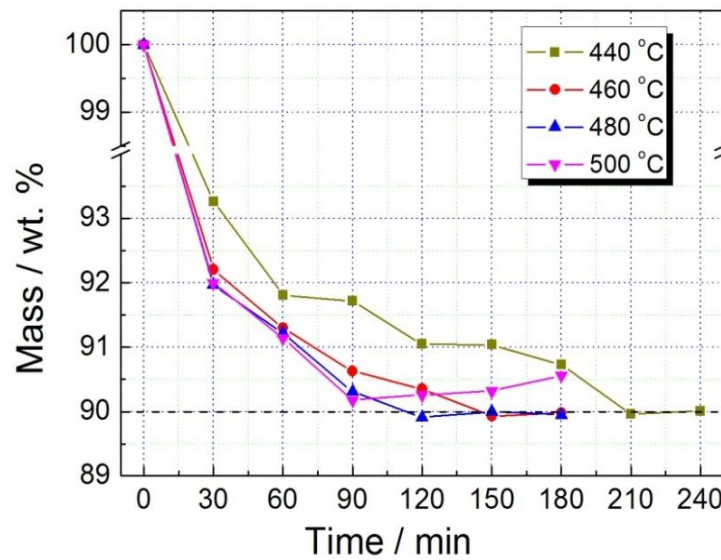
Figure 2.18. Effect of thermal condition on the weight loss of GLARE scrap.

2.3.2.2 Property degradation of recycled S2-glass fibre

The SEM pattern of recycled S2-glass fibre after delamination is shown in Figure 2.19. It can be seen that the surface of the fibre is clean, indicating that FM 94 was completely decomposed under 480 $^\circ$C for 2 hours. The tensile strength for four kinds of fibres after exposure at different temperatures has been tested by the company AGY, which is a world leader in high performance glass fibres used in a broad range of markets, including automotive, construction, defence, electronics, aerospace and marine. The tensile tests of AGY were performed at room temperature by following ASTM 2101-94 standard, the results are shown in Figure 2.20 [32]. The degradation of the tensile strength for recycled S2-glass fibre can be easily identified with Figure 2.20. As we can see in this figure, the tensile strength degradation is about 50% after thermal delamination at 480 $^\circ$C.

41
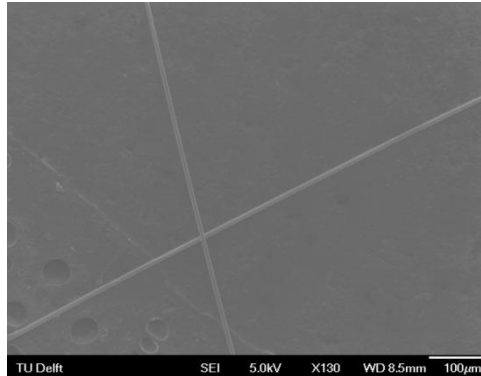
Figure 2.19. SEM pattern of recycled S2-glass fibres after delamination under 480 ^{o}C for 120 min.
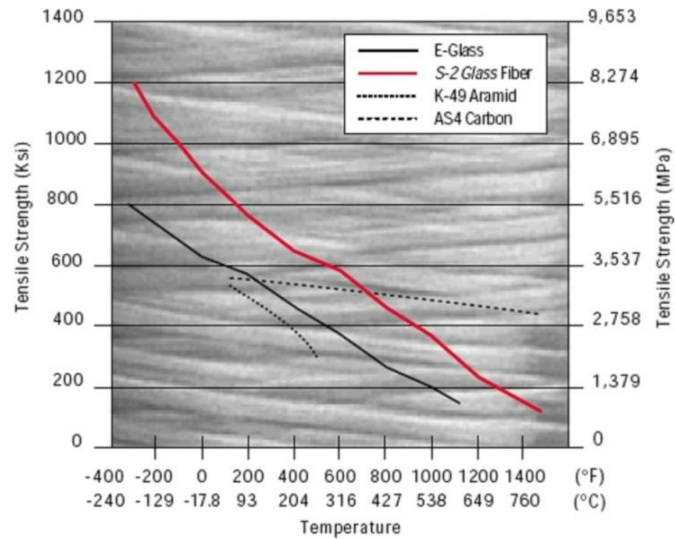
Figure 2.20. Fibre tensile strength after exposure at different temperatures, and the tensile tests were performed at room temperature by following ASTM 2101-94 standard [32].

2.3.2.3 Ultrasonic cleaning of recycled 2024 Al sheets

After thermal delamination, most of the primer residues on the surfaces of 2024 Al alloy sheets can be removed by ultrasonic cleaning in water. The 2024 Al alloy sheets after ultrasonic cleaning are presented in Figure 2.21. One surface of topmost Al sheet of GLARE in Figure 2.21 is much cleaner compared with other 15 surfaces, and basically no primer residue left on it. The most likely reason is that this surface was not treated by grit blasting during the production of GLARE, thus the primer residues on it can be easily cleaned because of the smooth surface.
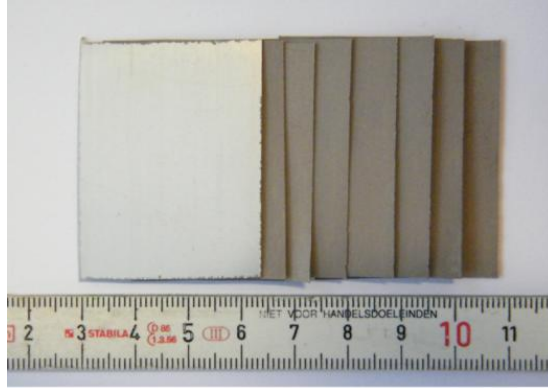
Figure 2.21. Al alloy sheets in GLARE after ultrasonic cleaning.

The composition of 2024 Al alloy sheet surface after delamination was investigated by using XRF analysis, and the composition of 2024 Al alloy surface after ultrasonic cleaning and polish was determined. The Al sheets after different treatments are shown in Figure 2.22, and the compositions are listed in Table 2.4. The composition of polished Al alloy presents the real composition of 2024 Al alloy used in GLARE.
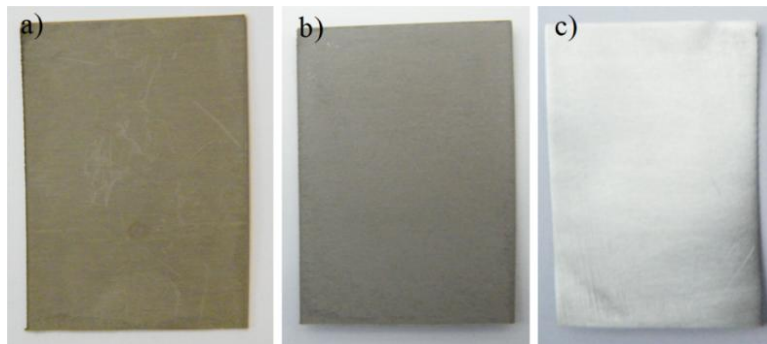
Figure 2.22. Al alloy sheet after a) thermal delamination, b) ultrasonic cleaning and c) polishing.

Table 2.4. Composition (wt%) of Al alloy sheet surface, concentrations of other elements are less than 0.02 wt%.

	Cu	Mg	Mn	Fe	Si	Ti	Cl	S	Ca	Br	Sr	Al
AD[a]	8.56	1.26	1.030	0.209	/	0.053	0.215	0.268	0.513	0.330	0.323	85.60
AU[b]	6.41	1.28	0.801	0.188	0.218	0.042	0.046	0.309	0.225	0.018	0.014	90.31
AP[c]	4.37	1.13	0.642	0.126	0.165	0.030	/	0.017	/	/	/	93.45

[a] *After Delamination* [b] *After Ultrasonic cleaning* [c] *After Polishing*

The tested composition shows that the Cu concentration of 2024 Al alloy sheet surface after delamination is 8.56 wt% while the concentration of Cu is 4.37 wt% in the polished 2024 Al alloy. The Mn concentration after delamination is also higher than that in polished 2024 Al alloy but the difference is small, just 0.25 wt%. The concentration of Mg, Fe, Cl, Ca, S, Br, and Sr are also higher than those of polished 2024 Al alloy. The excess concentrations should come from the residual primers. But considering that the thickness of coating is so thin compared to that of 2024 alloy sheet, the difference between the final composition of 2024 Al alloy after re-melting and nominal composition of 2024 Al alloy should be very small. The XRF results also indicated that ultrasonic cleaning can remove most of the residues on the 2024 Al alloy surface and decrease the concentration of impurity elements, especially for Cu, Mn, Br, Sr, Ca, and Cl.

2.4 Conclusions

The non-isothermal and isothermal thermal analysis is employed to study the decomposition behaviour of epoxy resins BR 127 and FM 94 in GLARE, which provides significant information for optimization of process parameters for thermal delamination of GLARE.

Under non-isothermal conditions, the decomposition of resins consists of four steps, where the first step is attributed to the decomposition of BR 127, and the later three steps are attributed to decomposition of FM 94. The initial decomposition temperature of BR 127 and FM 94 is 188 ^{o}C and 255 ^{o}C, respectively, in both oxidising and inert atmospheres, when the heating rate of 1 ^{o}C min^{-1} is employed. The final conversion of resins in air and nitrogen is 100% and 90%, respectively, when the GLARE sample of 60 mg is heated up to 500 ^{o}C in air and up to 600 ^{o}C in nitrogen with the same heating rate of 1 ^{o}C min^{-1}.

Based on the results of non-isothermal analysis, four holding temperatures (230 ^{o}C, 310 ^{o}C, 350 ^{o}C and 450 ^{o}C) are selected to investigate the isothermal kinetics of resins decomposition in GLARE. The conversion is 4.4%, 48.4%, 57.8% and 100% when samples were kept at 230 ^{o}C, 310 ^{o}C, 350 ^{o}C and 450 ^{o}C, respectively, for 3 hours in nitrogen, while the conversion under the same conditions in air is 7.2%, 43.4%, 69.4% and 100%, respectively. All epoxy resins in GLARE can be completely decomposed at 450 ^{o}C, and the required time is 100 min and 70 min, respectively, in nitrogen and air. Thus, an oxidising atmosphere is more preferred for resins decomposition which is consistent with the non-isothermal analysis results. Two decomposition mechanisms, nth-order for decomposition at 230 ^{o}C and 450 ^{o}C and autocatalysis for decomposition at 310 ^{o}C and 350 ^{o}C, are derived from the isothermal analysis. The isothermal kinetic models were constructed according to the relations between mass loss and time. For nth-order decomposition, the activation energies in nitrogen atmosphere are little higher in comparison to those in air atmosphere at the same holding temperature, but the initial conversion rates k (maximum conversion rate) in air are higher compared to those in nitrogen, especially at 230 ^{o}C. For autocatalytic decomposition, the effect of reaction products on conversion rate is more significant within an oxidising atmosphere.

The optimum GLARE thermal delamination process should be at 480 ^{o}C for 2 hours based

on the results of thermal analysis and experimental optimization, so that the S2-glass fibres and 2024 Al alloy can be well separated. The degradation of the tensile strength for recycled S2-glass fibres is about 50% after GLARE thermal delamination at 480 ^{o}C according to the test result of company AGY for fibres exposed at different temperatures. Most of the residues on the 2024 Al sheet surface after primer BR 127 decomposition can be removed in water with ultrasonic cleaning.

References

[1]   Vlot A, Gunnink JW. Fibre Metal Laminates, An Introduction. Dordrecht: Kluwer Academic Publishers (2001).

[2]   Hinz S, Omoori T, Hojo M, Schulte K. Damage characterisation of fibre metal laminates under interlaminar shear load. Composites: Part A 40 (2009) 925.

[3]   Alderliesten RC, Homan JJ. Fatigue and damage tolerance issues of Glare in aircraft structure. International Journal of Fatigue 28 (2006) 1116.

[4]   http://www.fokker.com/Innovations-GLARE.

[5]   Asokana P, Osmania M, Price ADF. Assessing the recycling potential of glass fibre reinforced plastic waste in concrete and cement composites. Journal of Cleaner Production 17 (2009) 821.

[6]   Pickering SJ. Recycling technologies for thermoset composite materials-current status. Composites Part A 37 (2006) 1206.

[7]   Pimenta S, Pinho ST. Recycling carbon fibre reinforced polymers for structural application: technology review and market outlook. Waste Management 31 (2011) 378.

[8]   Yoshioka T, Sato T, Okuwaki A. Hydrolysis of waste PET by sulfuric acid at 150 ^{o}C for a chemical recycling. Journal of Applied Polymer Science 52 (1994) 1353.

[9]   Chen JS, Ober CK, Poliks MD. Characterization of thermally reworkable thermoset; materials for environmentally friendly processing and reuse. Polymer 43 (2003) 131.

[10] Tempelman E. Sustainable transport and advanced materials. PhD Thesis, Delft University of Technology (1999).

[11] Dang WR, Kubouchi M, Sembokuya H, Tsuda K. Chemical recycling of glass fibre reinforced epoxy resin cured with amine using nitric acid. Polymer 46 (2005) 1905.

[12] Allred RE, Gosau JM, Shoemaker JM. Recycling processing for fibre/epoxy composites. In: SAMPE 2001 Symposium & Exhibition. SAMPE, Longbeach, CA, USA. 2001:172.

[13] Pinero-Hernanz R, Garcia-Serna J, Dodds C, Hyde J, Poliakoff M, Cocero MJ, Kingman S, Pickering S, Lester E. Chemical recycling of carbon fibre composites using alcohols under subcritical and supercritical. The Journal of Supercritical fluids 46 (2008) 83.

[14] Jiang G, Pickering SJ, Lester EH, Turner TA, Wong KH, Warrior NA. Characterisation of carbon fibres recycled from carbon fibre/epoxy resin composites using supercritical *n*-propanol. Composites Science Technology 69 (2009) 192.

[15] Shokrolahi F, Sadi M, Shokrolahi P. A study on curing kinetic of bisphenol-F using benzyl dimethyl amine by isothermal DSC. Journal of Thermal Analysis and calorimetry 82 (2005) 151.

[16] Lee JY, Choi HK, Shim MJ, Kim SW. Kinetics studies of an epoxy cure reaction by isothermal DSC analysis. Thermochimica Acta 343 (2000) 111.

[17] Guo ZS, Du SY, Zhang MB, Wu ZJ. Modeling the curing kinetics for a modified bismaleimide resin using isothermal DSC. Journal of Applied Polymer Science 92 (2004) 3338.

[18] Barral L Cano J, López J, López-Bueno I, Nogueira P, Abad MJ, Ramíez C. Decomposition behavior of epoxy-resin systems cured by diamines. European Polymer Journal 36 (2000) 1231.

[19] Wu GC, Yang JM. The mechanical behavior of GLARE laminates for aircraft structures. JOM 57 (2005) 72.

[20] Jen MHR, Sung YC, Lai YD. Tensile and fatigue testing of hybird Al/APC-2 Nanocomposite laminates at elevated temperature. Advanced Materials Research 47-50 (2008) 592.

[21] Bamford CH, Tipper CFH, editors. Comprehensive chemical kinetics. New York: Elsevier (1980).

[22] Park JW, Oh SC, Lee HP, Kim HT, Yoo KO. A kinetics analysis of thermal degradation of polymers using a dynamic method. Polymer Degradation and Stability 67 (2000) 535.

[23] Janković B. The kinetics analysis of isothermal curing reaction of an unsaturated polyester resin: estimation of the density distribution function of the apparent activation energy. Chemical Engineering Journal 162 (2010) 331.

[24] Sorai M. Comprehensive handbook of calorimetry & thermal analysis. Chichester: John Wiley & Sons Ltd (2004).

[25] Hatakeyama T, Quinn FX. Therrnal analysis fundamentals and applications to polymer science (Second Edtion). Chichester: John Wiley & Sons Ltd (1999).

[26] Šesták J, Berggren G. Study of the kinetics of the mechanism of solid-state reactions at increasing temperatures. Thermochim Acta 3 (1971) 1.

[27] Lee JH, Lee JW. Kinetics parameters estimation for cure reaction of epoxy based vinyl ester resin. Polymer Engineering Science 34 (1994) 742.

[28] Kamal MR, Sourour S. Kinetics and thermal characterization of thermoset cure. Polymer Engineering Science 13 (1973) 59.

[29] Ryan ME, Dutta A. Kinetics of epoxy cure: a rapid technique for kinetic parameter estimation. Polymer 20 (1979) 203.

[30] Boey FYC, Qiang W. Experimental modeling of the cure kinetics if an epoxy-hexaanhydro-4-methylphthalicanhydride (MHHPA) system. Polymer 41 (2000) 2081.

[31] Hseih HK, Su CC, Woo EM. Cure kinetics and inter-domain etherification in an amine-cured phenoxy/epoxy system. Polymer 39 (1998) 2175.

[32] www.agy.com/technical_info/graphics_PDFs/Advanced_Materials.pdf

Chapter 3 Al alloy recycling

After GLARE delamination, S2-glass fibre and 2024 Al sheets are well separated, then the recycling of 2024 Al sheets can be carried out, which is presented in this chapter. The yield and quality of the recycled Al alloy are two important criteria to evaluate the recycling result. High metal yield of Al alloy with similar composition to original 2024 Al alloy is preferred in this research. Refining method is employed for the recycling of 2024 Al in this work due to its advantages on high yield and good quality, and $NaCl-KCl-Na_3AlF_6$ and $NaCl-KCl-MgF_2$ are selected as fluxes. Six factors which have an important influence on Al recycling results are investigated, the studied factors are listed below:

- ◆ *Weight ratio of NaCl to KCl*
- ◆ *Additives in NaCl-KCl flux*
- ◆ *Refining temperature*
- ◆ *Size of 2024 Al scrap*
- ◆ *Weigh ratio of flux to 2024 Al scrap*
- ◆ *Refining atmosphere*

The yield of recovered Al alloy can reach as high as 98 wt% by using a refining method with appropriate process parameters, and the compositions of the recovered Al alloy are well consistent with the nominal composition of 2024 Al alloy when $NaCl-KCl-MgF_2$ flux is used.

The EOL GLARE recycling was also evaluated at the end of this chapter. The experiment results indicated that the Ti-6Al-4V hi lock (Fastener for GLARE assembly) did not dissolve into the Al melt while settle down to the bottom of the crucible due to the higher melting point and larger density of Ti-6Al-4V alloy compared to 2024 Al. Thus, the Ti concentration in the recycled Al alloy within the range of 2024 Al alloy nominal composition can be obtained after re-melting of EOL GLARE scrap.

3.1 Introduction

After GLARE delamination, S2-glass fibres and 2024 Al alloy sheets are completely separated. The quality of the recycled 2024 Al alloy is one of the vital criteria for evaluating GLARE recycling. Thus 2024 Al alloy recycling is very important for the whole recycling procedure. A higher recovery and yield of Al alloy with the similar composition with initial alloy are preferred in Al recycling. It is expected that the recycled 2024 Al alloys can be used again for GLARE production and the greatest value of the recyclates can be achieved.

As mentioned in chapter 1, there are many methods developed for Al recycling. *Refining method* is employed in this work because of its concise operation and high quality recycled Al alloy. Though the metal oxidation loss during re-melting and refining are always unavoidable, this can be solved to a large extent by using an appropriate salt flux. Moreover, the flux can be repeatedly used due to the clean surface of Al alloy scrap after simple treatment, thus the negative impact of salt slag on environment is low because of the rotative small amount of salt flux.

In this chapter, the influence of two different fluxes based on NaCl-KCl system on yield and quality of recycled 2024 Al alloy are studied. Besides, the effect of the amount of additional fluorides in NaCl-KCl, re-melting temperature, weight ratio of salt fluxes to alloys and the size of 2024 Al alloy scrap on the recycling result are also investigated.

3.2 The role of salt flux and its treatment

3.2.1 Salt flux for Al recycling

The salt flux is a barrier between the liquid aluminium alloy and the oxygen of the atmosphere during the re-melting and refining process and can reduce the superficial oxidation. Salt flux is also an efficient absorber for the oxide layers and contaminations. For Al recycling, suitable salt fluxes should have the following properties [1]:
- Melting point below 720 $^{\circ}$C
- Low viscosity
- Easily detachable from the liquid bath
- Reacting with the alloying element in Al alloy
- No input of new impurities into Al alloy
- Not hygroscopic
- Low vapor pressure
- Low cost
- Low treatment cost for salt slag.

The main functions of the salt fluxes in Al recycling are listed below[1]:

- Prevent the oxidation of molten Al alloy
- Remove the superficial oxide layer formed previously or during the heating of

furnace
- Promote the coalescence of Al alloy droplets
- Maintain the oxides in suspension within the salt slag
- React with impurities.

The salt fluxes are usually based on NaCl and KCl mixtures because of the low cost and low melting point of these materials. Sodium chloride is lower in cost, while potassium chloride has lower viscosity and surface tension which increase the salt fluidity. The mixture of NaCl and KCl also has a lower melting point than sodium chloride or potassium chloride alone, and the equimolar NaCl and KCl mixture provides a minimum melting point of the system. The phase diagram of NaCl-KCl system [2] is shown in Figure 3.1.

Chlorides and fluorides such as $MgCl_2$, $CaCl_2$, $AlCl_3$, Na_3AlF_6, NaF, MgF_2, KF, BaF_2 and CaF_2 are usually employed as positive additions for NaCl and KCl salt mixtures to obtain a better refining efficiency of Al alloy recycling.
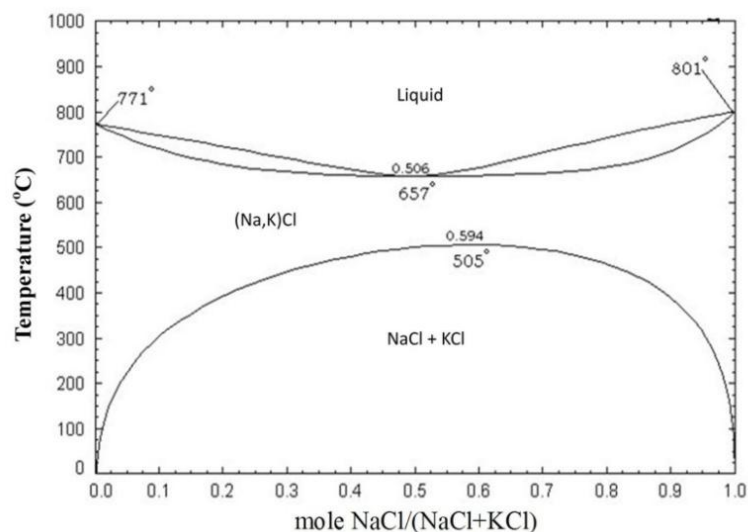

Figure 3.1. Phase diagram of NaCl-KCl system [2].

3.2.2 Effect of additives on flux performance

Several aspects of additional salts which are closely related to the final performance of fluxes are listed below[1]:

- Interfacial tension between Al alloy and salt
- Coalescence ability and viscosity
- Interaction between Al alloy and salt
- Metal yield.

Interfacial tension

The interfacial tension between Al alloy melt and molten salt is an important factor for the quality of recycled Al alloy during Al refining. The interfacial tension is closely related to the composition of Al alloy as well as the composition of salt flux. Moreover, for most systems, interfacial tension decreases with increasing refining temperature. But the influence of temperature on interfacial tension is rather little compared to the composition of salt flux. The effect of salt flux composition on interfacial tension is the direct result of interaction between all metal cations and halide anions in the salt melt. Higher interfacial tension between molten Al and salt melt is required to promote the coalescence of metal droplets and the separation of salts from the metal pool.

The interfacial tension between liquid aluminium and equimolar NaCl-KCl mixture is 7.55×10^{-4} kg/cm^2 at 740 ^{o}C, while the value of the interfacial tension between the liquid Al alloy of beverage cans and equimolar NaCl-KCl mixture is 5.61×10^{-4} kg/cm^2 [3]. The interfacial tension is decreased with the increasing activity of surface active elements [4].

The effect of fluoride additions to equimolar NaCl-KCl salt fluxes on the interfacial tension between liquid aluminium and the salt flux was firstly studied by Martin-Grain et al. [5]. After that, more fluorides [3,6-8] were selected to add into equimolar NaCl-KCl salt flux by researchers to enlarge the range of effective fluorides, and the effect of alloying elements such as Mg on interfacial tension were also studied. Fluorides additions will decrease the interfacial tension between the aluminium melt and the salt flux. The efficiency on interfacial tension decrease was compared for different fluorides, and the interfacial tension between aluminium melt and salt flux with different additives was arranged in an decreasing order of efficiency as follows [3]:

$$Na_3AlF_6 \rightarrow LiF \rightarrow CaF_2 \rightarrow MgF_2 \rightarrow NaF \rightarrow KF$$
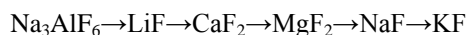
Coalescence ability and viscosity

In aluminium recycling, coalescence can be explained as the ability of junction and growth of aluminium droplets, firstly dispersing in the salt flux then forming bigger drops which have better conditions to be decanted into an aluminium pool under the flux [1]. The coalescence is also the capability to remove the superficial layer of oxide [9].

Various kinds of fluorides and chlorides were added to the NaCl-KCl mixture [9], and the effects of additional fluorides and chlorides on aluminium coalescences are described in Table 3.1. It is obvious that fluoride additions are more efficient for aluminium coalescence compared to chloride additions.

The fluorides additions also have influence on the viscosity, and the additions of NaF and KF decrease the viscosity of molten salts [10-11]. The decrease of the viscosity explains partially the results of Tenório and Delgado [12] who observed an increase in the aluminium recovery as the amount of fluoride increase in the molten salt. For chlorides, the additions of CaCl$_2$, MgCl$_2$ and MnCl$_2$ are also beneficial to decrease the viscosity of molten salts [13]. The decrease of viscosity is helpful to the movement of small

aluminium droplets trapped within the salt layer, and provides better conditions for aluminium coalescence. On the contrary, the additions of Na_3AlF_6, Na_2SiF_6 or CaF_2 will increase the viscosity of molten salts [13].

Table 3.1. Effect of fluorides and chlorides additions on the coalescence of aluminium in the salt flux [9].

Additions	Coalescence	Required time for coalescence (second)
Na_3AlF_6	Complete	30
CaF_2	Moderate	222
NaF	Complete	> 270
AlF_3	Almost complete	36
MgF_2	Moderate	> 300
$NaAlF_4$	Almost complete	24
LiF	Complete	114
KF	Complete	41
SrF_2	Almost complete	52
BaF_2	Almost complete	37
$MgCl_2$	None	-
$CaCl_2$	None	-
LiCl	Poor	> 600
$AlCl_3$	Poor	> 600

The work of Ye and Sahai [14] shows that Na_3AlF_6, NaF, KF and LiF present excellent performance on coalescence when 5% (% is the weight percent in this chapter unless otherwise stated) fluoride was added to the equimolar NaCl-KCl mixtures, though the cryolite (Na_3AlF_6) addition increases the viscosity of molten flux.

Therefore, the performance of fluoride additions should be determined by the co-action of the change of viscosity and the ability of breaking the oxide layer and [1].

Salt/oxide interaction

The solubility of oxide in molten salts was investigated [15-16], the result indicated that Na_3AlF_6 can dissolve up to 12% Al_2O_3 at 955 ^{o}C, NaF can dissolve 5% Al_2O_3 at 985 ^{o}C and CaF_2 dissolves about 25% Al_2O_3 at 1275 ^{o}C. But the equimolar of NaCl-KCl mixture without fluorides addition showed poor performance [10]. It is very difficult for chlorides to dissolve any alumina and the solubility of Al_2O_3 in chlorides is practically zero. It explains well the phenomena mentioned before: the salt fluxes with chloride additions are hard to promote the aluminium coalescence.

Previous research [10] indicated that the additions of fluorides can enhance the alumina solubility in salt flux, and the most effective addition is NaF, followed by CaF_2 and KF. The solubility order of alumina in salt is arranged as:

$$NaF \rightarrow CaF_2 \rightarrow KF$$

Although it is well recognized that the salt fluxes can promote the removal of the oxide layer, few data are available for the explanation of the mechanism of oxide layer removal. Ye and Sahai [14] suggested that the fluorides of molten salts attack the external oxide layer, providing the access of chloride ions to the interface of metal/oxide. The removal of the oxide layer is attributed to the formation of aluminium chloride which is volatile at the temperature of recycling processes. Van Linden and Stewart [17] suggested that the molten salt intensively wets the external oxide layer, then the boundaries of oxide layer is dissolved by the fluoride containing salt fluxes which would cause the separation of the oxide layer.

Effect of salt addition on metal yield

The aluminium yield is increased with the increase of fluoride concentrations in the salt flux up to 10% [17]. Above this concentration, the aluminium yield decreases with increasing of CaF_2 or MgF_2 addition and remains constant for NaF and KF addition.

Johnston and Peterson [18] studied the effect of magnesium on the aluminium yield. The results indicated that magnesium promotes the formation of spinel $MgO \cdot Al_2O_3$ or $MgAlO_4$ in the black dross. The spinel has higher density than salt flux, therefore, it has a strong tendency to sink through the slag layer. This fact implies a decrease in the aluminium yield because of the enrichment of oxides in the bottom of the slag layer, and this causes difficulties in the separation of aluminium from slag.

The effect of equimolar NaCl-KCl salt fluxes with additional KF, CaF_2 or Na_3AlF_6 fluorides on aluminium yield was studied by Tenório and Delgado [12]. The maximum aluminium yields were 95%, 92% and 94% when 5% KF, 5% CaF_2 and 5% Na_3AlF_6 were added to equimolar NaCl-KCl salts, respectively.

Xiao and Reuter [19] investigated the recycling of aluminium turning scrap by using the salt fluxes consisting of 70% NaCl-30% KCl and additional Na_3AlF_6, and the aluminium yield can reach 95% but the yield depends on the size and quality of the turning scrap.

The fluoride efficiency on the metal yield increases in the following sequence [12]:

$$KF \rightarrow Na_3AlF_6 \rightarrow NaF \rightarrow CaF_2$$
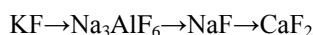
3.2.3 Magnesium behaviour after refining with salt flux

Many important aluminium alloys contain 0.1-10% magnesium, especially casting alloys 518 and 520, which contain 8% and 10% Mg, respectively. Some wrought alloys also contain high levels of magnesium, the nominal Mg concentration of 2024, 7075 and 7050 Al alloy are 1.2-1.8%, 2.1-2.9% and 1.9-2.6%, respectively [20]. In recycling, the wrought

aluminium scrap is always contaminated with some casting aluminium or contains impurity elements which are hard to remove. It is quite often practice to use the wrought aluminium to produce casting aluminium with lower magnesium content (generally less than 0.2 wt%). Therefore, it is necessary to apply demagging (removal of Mg) during the re-melting operations. This demagging requirement was necessary to avoid the formation of magnesium silicide, a brittle intermetallic compound which might break under stress and might introduce cracks in the castings. There are three general methods for magnesium removal: chlorination, using solid chloride-containing fluxes and injection of AlF_3 or $NaAlF_4$ [13]. But it is also important to keep magnesium in the aluminium during the re-melting of clean wrought aluminium scrap, and in such a way, the clean scrap can be reused as the same wrought aluminium after recycling. Therefore, it is important to understand the influence of fluxes on magnesium behaviour during re-melting.

Magnesium can react with some fluoride and chloride salts ($Mg + 2MeX = MgX_2 + 2Me$ or $Mg + MeX_2 = MgX_2 + Me$) at very high temperature, as shown in Figure 3.2 [13]. If the equilibrium constant is greater, it implies the loss of Mg into chloride or fluoride is very significant. Therefore, the addition of NaCl and KCl will not remove magnesium from an Al melt, but the addition of NaF, KF and AlF_3 in flux is active for magnesium removal during re-melting, according to the results presented in Figure 3.2. Cryolite can also react with magnesium [21], the magnesium will escape from the Al melt and form the compound $NaMgF_3$.
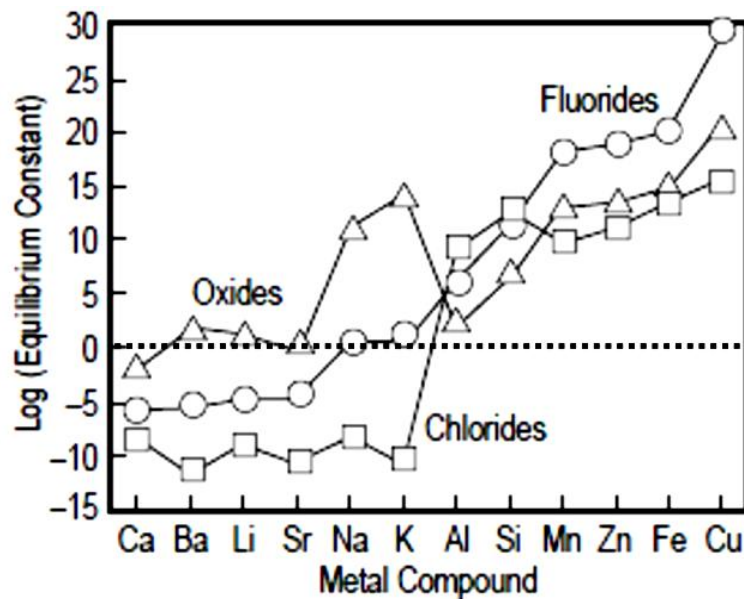

Figure 3.2. Reaction equilibrium between magnesium in aluminium and different oxides, chlorides and fluorides at 723 ^oC using reaction $Mg + 2MeX = MgX_2 + 2Me$ and $Mg + MeX_2 = MgX_2 + Me$ [13].

3.2.4 Treatment of salt slag

The commercial process in Europe for Al recovery from scrap involves crushing, sizing, re-melting and refining often in rotary furnaces under the protection of salt flux. During re-melting, after decomposition of organic contaminants (paints, plastics, coatings, and hybrid sandwich components), residual carbon is available to react with liquid aluminium and is entrapped in the salt slag. Moreover, other contaminants will also react with active liquid aluminium and form compounds. The salt slag is basically a conglomerate of crystallized salt, solid non-metallic product (NMP) and small metal beads. The NMP mainly consists of aluminium oxides, oxides of alloying elements (Mg, Si, Cu, Zn, Fe, etc), spinels, Al_4C_3, AlN, AlP, Al_2S_3 [22]. Landfill of this material is still economically feasible in some countries, but is either banned or too expensive elsewhere, such as in Europe.
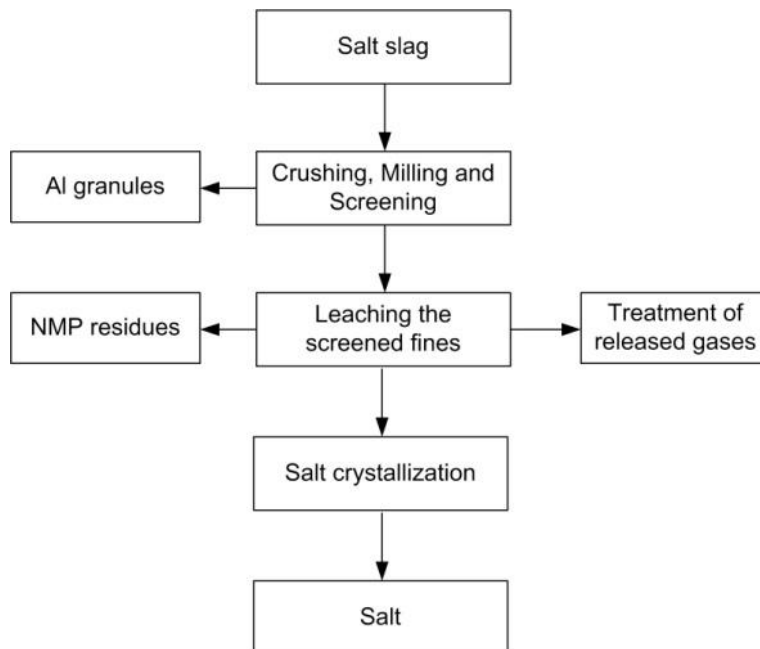
Figure 3.3. Flow diagram of Al recovery from salt slag and salt reuse.

It is common practice to recover most of the aluminium from salt slag by crushing, milling, and screening to separate the entrapped aluminium granules, leaching of the fines in water to produce saturated brine, diluting the generated gases or using the gases as fuel; solid-liquid separation and leaching of NMP residue; and slat crystallization (as shown in Figure 3.3). The crystallized salt and the separated metal granules are returned to the secondary aluminium smelters. The washed NMP residues, including oxides and carbon, are filtered and dried. After calcinations, residues can be further processed for application in the cement industry or for refractory bricks [22]. During the leaching with water, some gases are leased, such as H_2, NH_3, CH_4, PH_3, H_2S, HCl and HF [23-24].

The released gases should be seriously treated to avoid any environmental pollution. In the case that the gas components are burned for heat generation, a subsequence standard off-gas treatment is required. The released gases can also be cleaned by using activated carbon filters and also by the use of sulphuric acid that reacts with the NH_3 to produce $NH_4(SO)_3$ [1].

3.3 Selection of salt flux

Considering that cryolite addition in NaCl-KCl salt flux can dissolve Al_2O_3 on the Al scrap surface, accelerate metal coalescence and obtain satisfied metal yield [12,15-16,19], thus the **NaCl-KCl-Na$_3$AlF$_6$** system is employed as salt flux in this work to study the effect of salt flux on alloy composition and metal yield during Al recycling. NaCl-KCl-Na$_3$AlF$_6$ is a commonly used salt system in industry and much research work. In this investigation, the weight ratio of NaCl to KCl in NaCl-KCl salt flux is 70:30 and 44:56, respectively. The salt composition of 70%NaCl-30%KCl was selected based on the preferred European melt salt composition. The salt composition of 44% NaCl–56% KCl is the eutectic composition of the NaCl–KCl system which would give better melting results theoretically due to the lower eutectic temperature of about 657 ^{o}C. The weight ratio of cryolite to NaCl-KCl salt mixture is 0, 5, 10, 15 and 20%, respectively. Though it is clear that cryolite will react with Mg to form MgF_2 during refining, this NaCl-KCl-Na$_3$AlF$_6$ system is efficient and competitive because of its price, outstanding ability on metal coalescence (see Table 3.1) and foreseeable high yield. Mg loss can also be compensated by the addition of pure Mg or Mg-Al master alloy in final aluminium alloy preparation.

To avoid Mg loss in the alloy during refining, another fluoride addition MgF_2 instead of cryolite can be considered. An important advantage for MgF_2 addition in the NaCl-KCl system is that it will not react with Mg and can prevent Mg loss in refining. Moreover, MgF_2 addition has also positive influence on metal yield, though its influence on the ability of metal coalescence is not as good as cryolite. Thus the **NaCl-KCl-MgF$_2$** system is also considered as flux in this investigation, the weight ratio of NaCl to KCl in NaCl-KCl salt flux is 44:56, and the weight ratio of cryolite to NaCl-KCl salt mixture is 5, 10, 15 and 20%, respectively.

3.4 Experimental details

The experiments for re-melting and refining of separated 2024 Al alloy scrap after GLARE delamination were carried out in an electric resistance chamber furnace (Carbolite company). Before GLARE thermal delamination, big GLARE scrap needs to be cut into small pieces to facilitate delamination operation and improve delamination efficiency. But, the size of Al alloy scrap has an important influence on metal yield during refining, thus 2024 Al alloy scrap with different sizes are employed to study the influence of scrap size on 2024 Al refining. The size (Length $\times$ Width) of 2024 Al scrap is 35 mm$\times$25 mm, 20 mm$\times$15 mm, 10 mm$\times$10 mm and 5 mm$\times$5 mm with a thickness of 0.4 mm, respectively. Figure 3.4 shows the Al scrap with the size of 35 mm$\times$25 mm$\times$0.4 mm.

25 g 2024 Al scrap was put into a C4 size alumina crucible and Al scrap pieces were covered with salt fluxes to minimize oxidation, enhance the coalescence of metal beads and collect the various contaminants from the scrap during re-melting and refining.
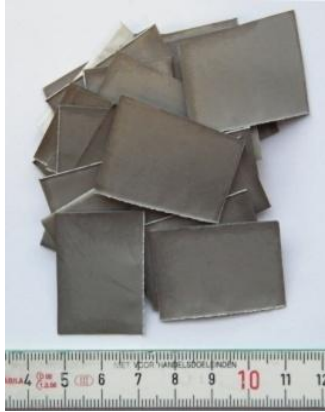
Figure 3.4. 2024 Al scrap for re-melting with the size of 35×25×0.4 mm.

The following parameters are studied through individual refining tests:

- Composition of salt flux

    70%NaCl-30%KCl-(0, 5, 10, 15 and 20%) Na$_3$AlF$_6$

    44%NaCl-56%KCl-(0, 5, 10, 15 and 20%) Na$_3$AlF$_6$

    44%NaCl-56%KCl-(5, 10, 15 and 20%) MgF$_2$

- Refining temperature

    720, 760 and 800 ^{o}C

- Refining atmosphere

    N$_2$ and air

- Weight ratio of NaCl-KCl salt mixture to 2024 Al alloy scrap

    0.5, 1, 1.5 and 2

- Size of 2024 Al scrap

    35 mm×25 mm, 20 mm×15 mm, 10 mm×10 mm and 5 mm×5 mm

The details about the experiments executed in this research are described in Table 3.2.

Table 3.2 Experimental conditions.

No.	Size of Al sheets (mm) Length×Width	T (°C)	Flux☆ (%)	Ratio*	Atmosphere	UC#
			Flux NaCl-KCl-Na₃AlF₆			
			Influence of Na₃AlF₆ amount in flux			
1-5	35×25	800	A with 0, 5, 10, 15 and 20% Na₃AlF₆	2	N₂	Yes
6	35×25	800	A with 10% Na₃AlF₆	2	N₂	No
7-11	35×25	800	B with 0, 5, 10, 15 and 20% Na₃AlF₆	2	N₂	Yes
			Influence of refining temperature			
12-13	35×25	720	A or B with 10% Na₃AlF₆	2	N₂	Yes
14-15	35×25	760	A or B with 10% Na₃AlF₆	2	N₂	Yes
			Influence of refining atmosphere			
16-17	35×25	800	A or B with 10% Na₃AlF₆	2	Air	Yes
			Influence of Al scrap size			
18-20	5×5, 10×10, 20×15	800	B with 10% Na₃AlF₆	2	N₂	Yes
			Influence of weight ratio of NaCl-KCl salts to Al scrap			
21-23	10×10	800	B with 10% Na₃AlF₆	1.5, 1, 0.5	N₂	Yes
			Flux NaCl-KCl-MgF₂			
			Influence of MgF₂ amount in flux			
24-27	35×25	800	B with 5, 10, 15 and 20% MgF₂	2	N₂	Yes
			Influence of weight ratio of NaCl-KCl salts to Al scrap			
28-29	35×25	800	B with 5% MgF₂	1.5, 1	N₂	Yes

☆ *A is salts mixture of 70%NaCl-30%KCl, B is salts mixture of 44%NaCl-56%KCl. * Weight ratio of NaCl-KCl salt mixture to Al scrap. # Ultrasonic cleaning.*

During re-melting and refining, heating rates of 15 ^{o}C min^{-1} was used. The temperature was controlled within an accuracy of ± 5 ^{o}C. Holding time was 2 hours for all experiments at the refining temperature. The gas flow rate of nitrogen was controlled at 2 dm^{3} min^{-1}.

After re-melting, the crucibles with the samples were washed with hot water, then the metal beads and the precipitates were filtered, dried and sieved. After mass balancing, the fraction of metal recovered with respect to the total scrap (in other words the metal yield) was calculated and the size distribution of recovered metal beads was measured. The metal beads are formed due to the high surface tension of the molten aluminium and no stirring employed in the crucible. Due to unknown quantities of oxide material entering, oxidation and side reactions, considerable care must be taken to produce a good mass balance. This, in addition to careful experimentation, is of utmost importance to produce good yield data. The recycled Al alloys were prepared for the XRF (Philips PW2400 WD-XRF spectrometer) and SEM (JEOL JSM 6500F) analysis to compare the composition and microstructures with the initial 2024 Al alloy. The filtered precipitates (dross) were prepared for XRD analysis (Bruker D8 Advance X-Ray Diffractometer) to identify the phases included.

3.5 Re-melting and refining results

3.5.1 Refining with flux NaCl-KCl-Na$_3$AlF$_6$

3.5.1.1 Influence of Na$_3$AlF$_6$ amount in flux

The salt composition of 70%NaCl-30%KCl was selected based on the preferred European salt flux composition. The salt flux on equimolar NaCl–KCl composition, i.e. 44%NaCl–56%KCl, was also employed in this research which would give better melting results theoretically due to the lower eutectic temperature of about 657 ^{o}C. Addition of cryolite to the mixture of NaCl and KCl was applied to increase the interfacial tension between the salt and the molten metal, enhance the stripping of oxide film from the metal droplets, favour the agglomeration of the metal droplets and reduce the aluminium loss by entrapped metal into salt slag. The size of 2024 Al scrap sample for refining is 35 mm×25 mm with a thickness of 0.4 mm, as shown in Figure 3.4. All employed weight ratios of the NaCl-KCl salts mixture (cryolite was not included in the weight of salt mixture) to scrap were set to 2, and the additional cryolite in the salt mixture is 0, 5, 10, 15 and 20%, respectively. The refining temperatures of all tests were chosen as 800 ^{o}C, and the tests were conducted under nitrogen protection.

Basic salt composition 1: 70%NaCl-30%KCl (Experiments 1-6)

The metal beads after refining by using 70%NaCl-30%KCl-Na$_3$AlF$_6$ fluxes are illustrated in Figure 3.5.

The refining result by using flux without cryolite was unsatisfactory. Aluminium was

surrounded by the Al_2O_3 film during refining, and NaCl and KCl can not destroy the oxide layer between molten flux and liquid aluminium, leading to awful aluminium coalescence.

But after the addition of cyolite in the salt flux, Al_2O_3 film dissolution into cryolite and larger metal beads can be obtained due to the significantly improved aggregation ability. When the cryolite amount is 5%, recovered 2024 Al alloy consists of abundant small size metal beads. When additional cryolite is higher than 10%, one big metal bead together with a small quantity of small size metal beads which were still entrapped in the salt flux are observed. But the increase of cryolite amount in salt flux has little influence on the metal coalescence when the additional cryolite is higher than 10%.

The 2024 Al alloy without ultrasonic cleaning after thermal delamination was also remelted by using of 70%NaCl-30%KCl salt flux with additional 10% Na_3AlF_6. The recovered 2024 Al is shown in the Figure 3.5 f), consisting of single big metal bead and plenty of small metal beads. This phenomena indicated that the coating residues on the surface of 2024 Al sheets would have minor influence on the metal coalescence during refining.
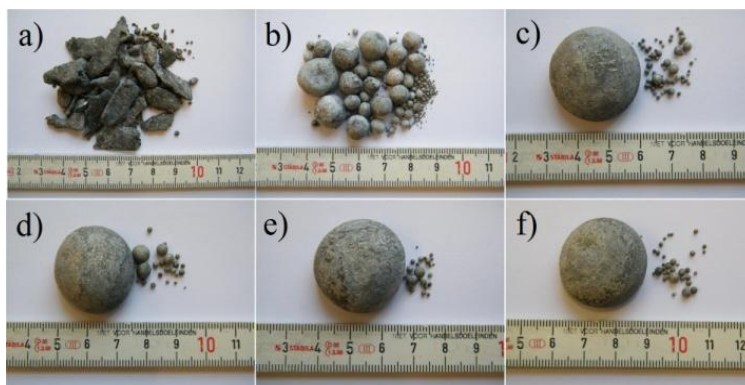
Figure 3.5. Recovered Al alloys after refining with flux 70%NaCl-30%KCl-Na_3AlF_6. Na_3AlF_6 addition in flux is a) 0, b) 5%, c) 10%, d) 15% and e) 20%. f) is recovered Al alloy after refining Al sheets without ultrasonic cleaning and additional cryolite in flux is 10%.

In order to better evaluate the recyclability of 2024 Al alloy after GLARE delamination, the total metal yield and the yields of different metal beads size ranges are investigated, and the effect of cryolite addition amount in the salt flux on metal yield is also discussed, as illustrated in Figure 3.6. Considering that the 2024 Al alloy scrap after delamination and ultrasonic cleaning is very clean, the recovery of 2024 Al scrap, namely the content of 2024 Al alloy in 2024 Al scrap, is assumed as 100%. From these results in Figure 3.6, it can be seen that the total metal yield of 2024 Al with 0, 5, 10, 15, 20% additional cryolite in fluxes are 97.5, 96.9, 97.4, 97.0 and 97.5%, respectively. The total yield after refining without cryolite addition in flux is higher than others because the oxides on the surfaces of aluminium scrap were not removed due to the negligible solubility of alumina in NaCl-KCl system. The total metal yield for 2024 Al scrap without ultrasonic cleaning is 96.46%.

The total metal yield represents the obtained 2024 Al alloy amount from the scrap if disregarding the possible reactions of salt flux with metal.

Since the small metal particles (< 2 mm) are eventually lost into the salt flux during industrial operation, the yield of big metal beads (≥ 2 mm) can better represent the recyclability. As we can see in Figure 3.6, the discrepancy of big metal beads (≥ 2 mm) yields are obvious, especially for 0% and 5% cryolite additions. The salt flux without additional cryolite has a poor performance on the refining behaviour compared to other fluxes, which was caused by the inability of NaCl-KCl mixture on metal coalescence. The yield of big metal beads (diameter ≥ 2 mm) is 93.4, 95.2, 96.8, 96.5 and 97.2% when the additional cryolite is 0, 5, 10, 15 and 20%, respectively. The yield of big metal beads after refining of Al scrap without ultrasonic cleaning is 96.0%. The difference between yields of big metal beads is small when the cryolite amount in the salt flux is higher than 10%, indicating that 10% cryolite addition in the salt flux is enough. For refining of Al scrap without ultrasonic cleaning, both total metal yield and big metal beads yield are little lower than those of Al scrap which were treated by ultrasonic cleaning though the cryolite amount in fluxes were the same. The residues on the Al sheets surfaces were entrapped in the salt flux during the refining, and increase the viscosity of molten salt flux which baffles the coalescence of Al alloy small beads.

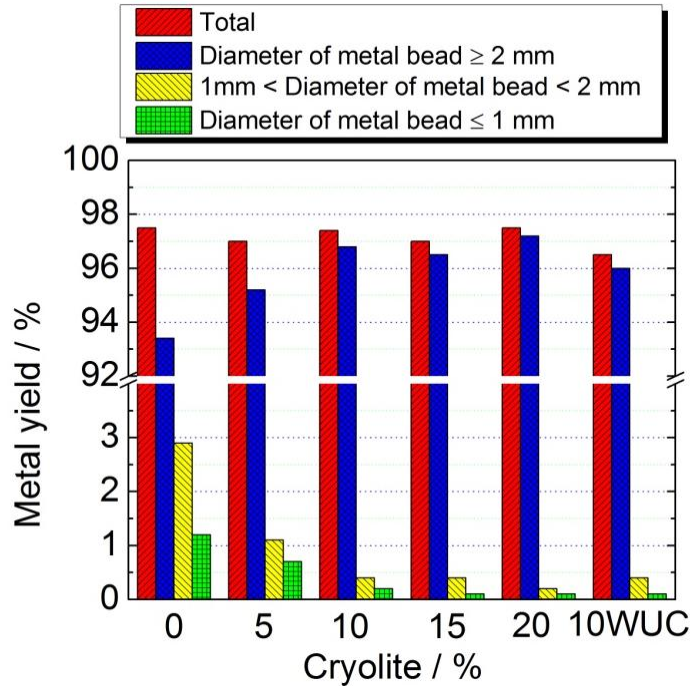*Figure. 3.6. Effect of Na$_3$AlF$_6$ addition in flux 70%NaCl-30%KCl-Na$_3$AlF$_6$ on total metal yield and size distribution of metal beads. The additional Na$_3$AlF$_6$ amounts in fluxes is 0, 5, 10, 15 and 20%, respectively. 10 WUC (without ultrasonic cleaning) means the Al sheets were untreated with ultrasonic cleaning before refining and the additional Na$_3$AlF$_6$ amount in salt flux is 10%.*

The inner morphology of recovered Al bead was observed, as the cross section shown in Figure 3.7 (a)-e)). The recovered metal beads were cut into two parts and no obvious defects can be found besides some micro holes in the grain boundary which is caused by the exfoliation of entrapped salts during polish, as presented in Figure 3.7 f). But the entrapped salt can easily move to the salt layer on the top of liquid aluminium during stewing in the industrial scale refining. The high quality of scrap with most of coatings on the 2024 Al sheets removed during thermal delamination, is the major reason for the high yield and good quality of recovered 2024 Al alloy. The influence of cryolite addition amount in flux on the quality of recovered aluminium alloy is limited.

The microstructure of recovered 2024 Al alloy was also investigated by using SEM and EDS analysis. The SEM patterns of recovered 2024 Al with 10% additional cyolite in the salt flux are shown in Figure 3.8. Main phases besides Al matrix in the recovered 2024 Al alloy are Al_2Cu (white phase) and AlCuMnFe (grey phase) precipitated around the grain boundary, but another important phase Al_2CuMg which usually occurred in initial 2024 Al alloy was not found. This can be explained by the magnesium reacting with cryolite, resulting in most or even all magnesium loss to the salt flux during the refining.
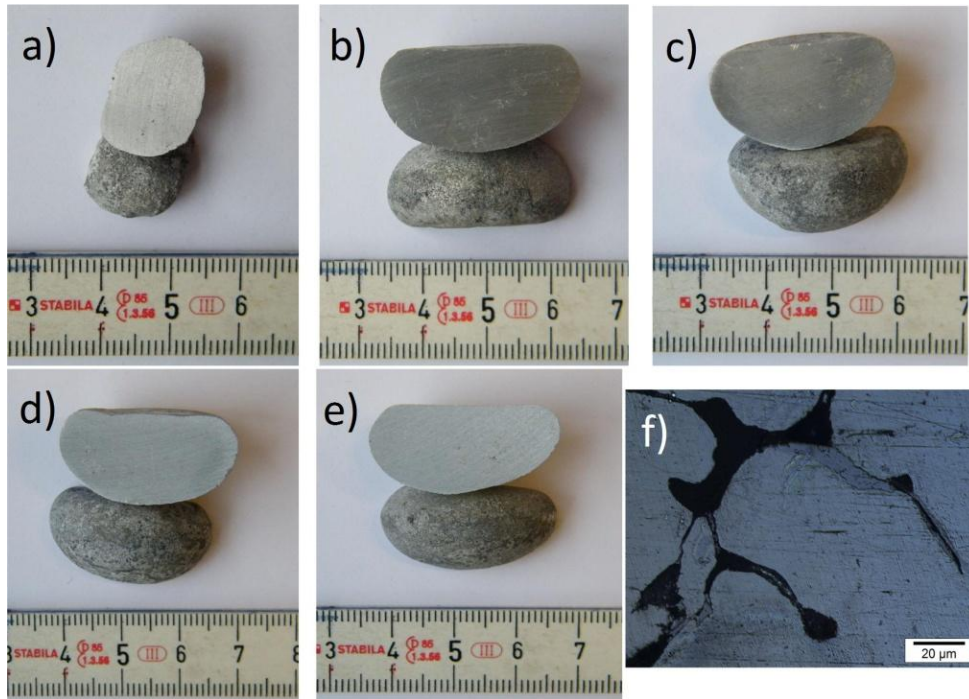

Figure 3.7. The inner morphology of recovered Al alloys. a) 5, b) 10, c) 15 and d) 20% Na_3AlF_6. e) is recovered Al alloy after refining Al sheets without ultrasonic cleaning and additional Na_3AlF_6 in flux is 10%. f) is the high magnification picture of c), the holes in the grain boundary are formed because of the exfoliation of entrapped salts during polish.
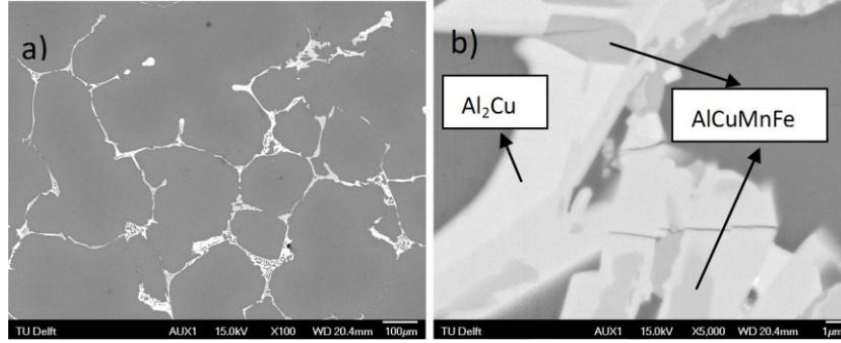
Figure 3.8. SEM patterns of 2024 Al alloy after refining with 70%NaCl-30%KCl salt flux including 10% additional Na₃AlF₆. a) low magnification (×100) and b) high magnification (×5000).

The XRF results of recovered Al alloys are listed in Table 3.3. It was found that all magnesium was lost in the recovered 2024 aluminium beads during refining with NaCl-KCl-Na₃AlF₆ flux due to the reaction between magnesium and cryolite. It confirmed that magnesium loss is the reason for disappearing of Al₂CuMg phase. But other alloying elements (Cu and Mn) are kept and impurity elements (Fe, Si, Ti) concentrations are not increased, just Al concentration was slightly improved due to extra Al formation during the reaction between magnesium and cryolite. The reaction of Mg and cryolite will be discussed later. Some Na, K and Cl were also detected in the aluminium beads after refining, which were the entrapped NaCl and KCl according to the detected concentration ratios of Na, K and Cl.

Though the cryolite addition in the salt flux was increased from 5% to 20% during refining, the influence of cryolite addition on final 2024 alloy composition is negligible. The ultrasonic cleaning has also little influence on the composition of recovered Al alloy.

Table 3.3. Composition (%) of Al sheets in GLARE and recovered Al alloy compositions (%) after refining, the additions of cyrolite in 70%NaCl-30%KCl-Na₃AlF₆ are 5, 10, 15 and 20%, respectively. Concentrations of other elements not shown in the table are lower than 0.05%.

Cryolite		Cu	Mg	Mn	Fe	Si	Ti	Na	K	Cl	Al
	5%	4.31	/	0.643	0.136	0.125	0.029	0.109	0.070	0.241	94.19
UC	10%	4.16	/	0.627	0.140	0.139	0.026	0.058	0.022	0.117	94.67
	15%	4.24	/	0.632	0.137	0.174	0.029	0.070	0.133	0.236	93.79
	20%	4.22	/	0.619	0.141	0.142	0.034	0.177	0.085	0.241	94.36
WUC	10%	4.30	/	0.664	0.134	0.094	0.027	0.154	0.109	0.342	94.21
2024 Al alloy in GLARE		4.37	1.13	0.642	0.126	0.165	0.030	/	/	/	93.45

Figure 3.9. XRD patterns of dross after water leaching salt slag which is obtained after re-melting and refining with salt flux 70%NaCl-30%KCl. No additional Na_3AlF_6 in the salt flux.

The dross obtained after water leaching of the salt slag was analyzed with XRD to better understand the behaviour of flux during refining. The phase composition of the dross obtained from 70%NaCl-30%KCl without additional Na_3AlF_6 is presented in Figure 3.9. The main phases in the dross are MgO and $MgAl_2O_4$. The possible reason for the formation of MgO and $MgAl_2O_4$ (spinel) is the reactions between Mg and Al_2O_3, as follows [25-26]:

$$3Mg + Al_2O_3 \rightarrow 2Al + 3MgO \tag{3-1}$$

$$3Mg + 4Al_2O_3 \rightarrow 3MgAl_2O_4 + 2Al \tag{3-2}$$

The Al_2O_3 in equation (3-2) was primarily introduced by the Al alloy scrap. Chlorides were not observed after water leaching because the NaCl and KCl can not react with any alloying element in alloy and the NaCl and KCl dissolved into water during leaching.
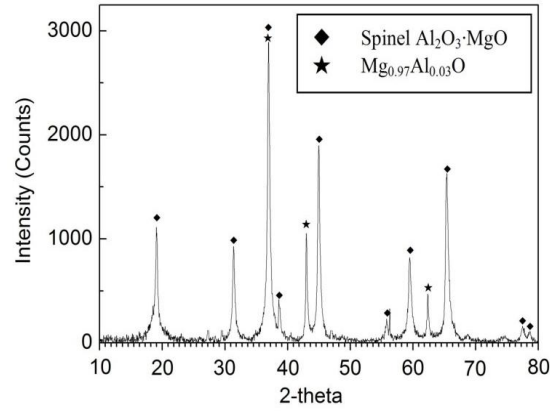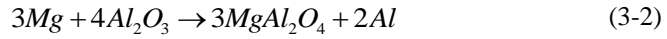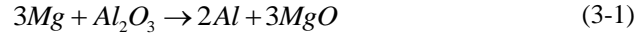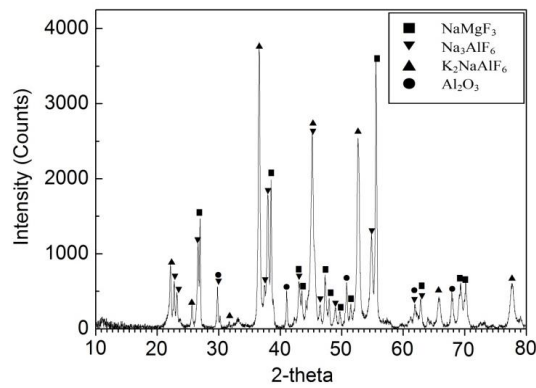

Figure 3.10. XRD patterns of dross after water leaching salt slag which is obtained after re-melting and refining with salt flux 70%NaCl-30%KCl-10% Na_3AlF_6.

NaMgF$_3$, Na$_3$AlF$_6$, elpasolite K$_2$NaAlF$_6$ together with Al$_2$O$_3$ are the major phases in the dross after water leaching of 70%NaCl-30%KCl with additional 10% Na$_3$AlF$_6$ flux, as shown in Figure 3.10. The detected Al$_2$O$_3$ phase was introduced from the initial Al alloy scrap. The formation of NaMgF$_3$ was caused by the reaction between Mg and cryolite at the liquid metal-liquid salt interface during refining. According to the XRD and XRF results, it is clear that all Mg prefers to form NaMgF$_3$ if the amount of crolite in flux is sufficient, and the magnesium oxidation is not preferred. The detected Na$_3$AlF$_6$ phase was the rest of original cryolite addition in the salt flux, and Na$_3$AlF$_6$ phase existed in the dross after water leaching due to its negligible solubility in water. The solubility of Na$_3$AlF$_6$, MgF$_2$ and NaF in water at 20 ^{o}C is 0.36g/l, 0.13g/l and 41g/l, respectively. MgF$_2$ was not found in the dross after XRD analysis though its solubility in water is very low, thus MgF$_2$ should not be formed during reaction between Mg and cryolite. Therefore, the most likely reaction equation between Mg and cryolite can be presented as follows:

$$3Mg + 2Na_3AlF_6 \rightarrow 3NaMgF_3 + 2Al + 3NaF \qquad (3\text{-}3)$$
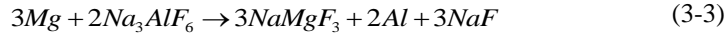
and all generated NaF was dissolved into water during leaching because of its high solubility in water. Equation (3-3) is different with the proposed reaction by Utigard et al. [13]. In Utigard's work, the products are Na, AlF$_3$ and MgF$_2$. Neither MgO nor MgAl$_2$O$_4$ was detected in the dross, indicating that Mg prefers to react with Na$_3$AlF$_6$ rather than with Al$_2$O$_3$.

The possible reason for the formation of elpasolite K$_2$NaAlF$_6$ is the interchange of Na$^+$ and K$^+$ under high refining temperature considering that Na$^+$ and K$^+$ can completely interchange in the binary NaCl-KCl system [27]. Elpasolite K$_2$NaAlF$_6$ was also detected in the dross after water leaching of salt mixture 40.5%NaCl-49.5%KCl-10%KF which had been used as flux for refining of beverage cans [27], and the formation of K$_2$NaAlF$_6$ in dross should be caused by the complicated reactions between Al$_2$O$_3$, chloride and fluoride.

In summary, 10% additional cryolite in 70%NaCl-30%KCl salt flux is preferred considering the quality and yield of the recovered Al alloy together with the economic factor. The yield of big metal beads (> 2 mm) is 96.8%, and the concentrations of major alloying elements and impurity elements in recovered Al alloys are consistent with nomination composition of 2024 alloy except Mg, and the Mg loss is caused by the reaction between Mg and cryolite. Moreover, with the same amount of cryolite in the flux (10%), the metal yield of big beads after refining without ultrasonic cleaning is decreased slightly from 96.8% to 96.0%, but the residues on the surface of Al alloy sheets after delamination have little influence on the final composition of recovered alloy.

Basic salt composition 2: equimolar NaCl-KCl (Experiments 7-11)

The 2024 Al alloys after refining with different cryolite additions in the equimolar NaCl-KCl (44%NaCl-56%KCl) salt mixture are presented in Figure 3.11. Similarly, the result by using flux without cryolite was unsatisfactory. After the addition of cryolite in the salt flux, big metal beads were easily formed even when the additional cryolite was just 5%.
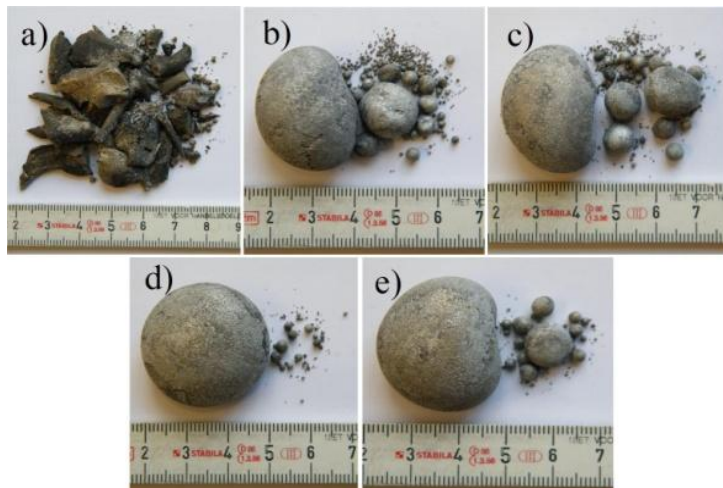
Figure 3.11. Recovered Al alloys after refining with flux 44%NaCl-56%KCl-Na$_3$AlF$_6$. Na$_3$AlF$_6$ addition in flux is a) 0, b) 5, c) 10, d) 15 and e) 20%, respectively.
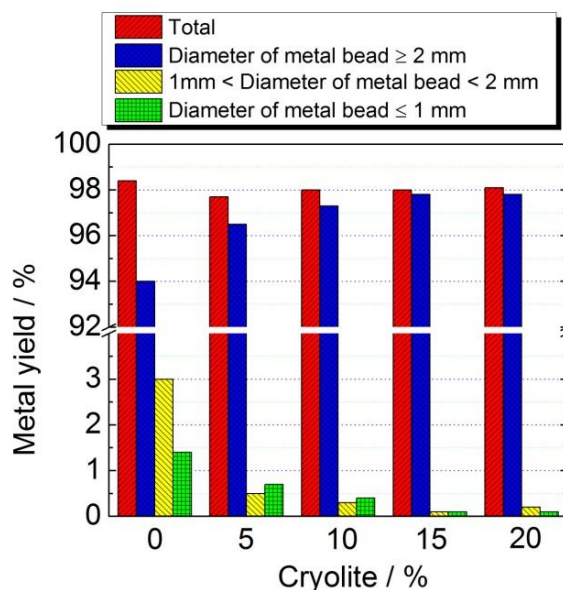
Figure 3.12. Effect of Na$_3$AlF$_6$ addition in flux 44%NaCl-56%KCl-Na$_3$AlF$_6$ on total metal yield and size distribution of metal beads. The additional Na$_3$AlF$_6$ in fluxes is 0, 5, 10, 15 and 20%, respectively.

Effect of cryolite addition on metal yield and size distribution of metal beads is shown in Figure 3.12. Compared with 70%NaCl-30%KCl-Na$_3$AlF$_6$ salt flux, both total yield and the yield of big aluminium beads are increased with the same cryolite addition in the salts. It

was attributed to the lower melting point of equimolar NaCl-KCl system which has a positive influence on the metal coalescence due to the lower viscosity of molten flux. The total yield is 98.4, 97.7, 98.0, 98.0 and 98.1% when the additional cryolite in 44%NaCl-56%KCl salt mixture is 0, 5, 10, 15 and 20%, respectively. The total yield after refining without cryolite addition in the salts is slightly higher than those with cryolite addition because the oxides on the surfaces of aluminium scrap were not removed due to the negligible solubility of alumina in NaCl-KCl system. The yield of big metal beads is 94.0, 96.5, 97.3, 97.8 and 97.8% when the additional cryolite is 0, 5, 10, 15 and 20%, respectively.

It is clear that the yield of big metal beads increased with the cryolite amount in the salt when the addition amount is lower than 10%, but the further increase of cryolite addition becomes ineffective for metal yield improvement when the cryolite addition is higher than 10%. This phenomenon is very similar to the influence of cryolite addition in 70%NaCl-30%KCl system.

The inner morphology of the recovered Al beads is shown in Figure 3.13 (a)-d)). No obvious holes were observed besides some micro holes in the grain boundary caused by the exfoliation of entrapped salts during polish (Figure 3.13 e)), which indicated a good quality of recovered Al alloy. SEM analysis of recovered Al alloy was used to identify its phase composition, as shown in Figure 3.14. The primary phases besides Al matrix are also Al_2Cu and AlCuMnFe, and the absence of Al_2CuMg is caused by the Mg loss during the refining. MgO and Al_2O_3 particles have not been found in the recovered Al alloy.

Figure 3.13. Recovered Al alloy inner morphology. Na_3AlF_6 addition in flux 44%NaCl-56%KCl-Na_3AlF_6 is a) 5, b) 10, c) 15 and d) 20%, respectively. e) is the high magnification picture of b), the holes in the grain boundary are formed because of the exfoliation of entrapped salts during polish.
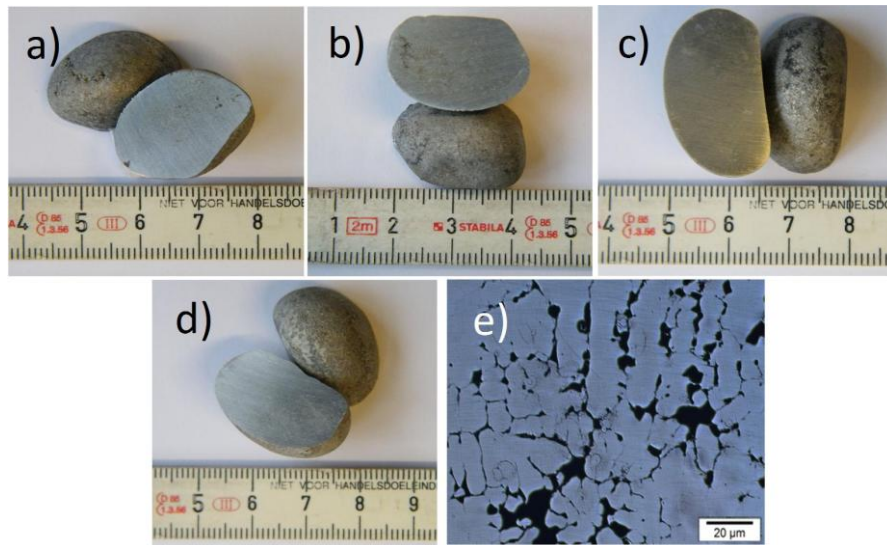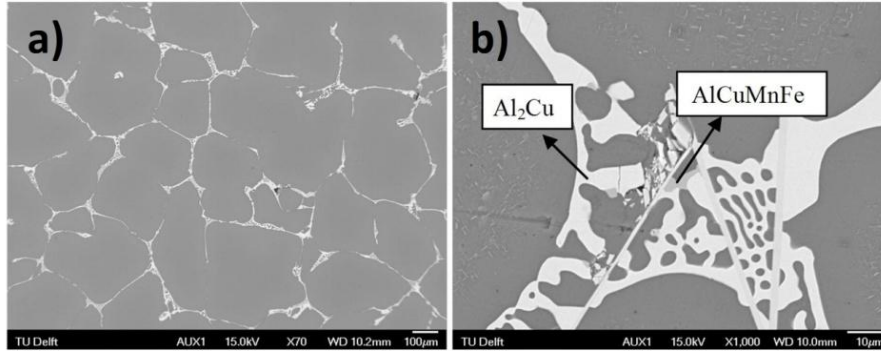
Figure 3.14. SEM patterns of 2024 Al alloy after refining with 44%NaCl-56%KCl salt flux including 10% additional cyolite. a) low magnification (×70) and b) high magnification (×1000).

Compositions of the recovered Al alloys are presented in Table 3.4. All Mg in 2024 Al alloy was removed by cryolite during re-melting and refining, but concentrations of other elements still meet the requirement of nominal composition of commercial 2024 Al alloy. Considering that the entrapped chlorides can easily move to the molten flux layer during industrial scale refining, entrapped NaCl and KCl will not be a problem for reuse of the recovered Al alloy.

Table 3.4. Compositions (%) of the recovered Al alloy, the additions of Na_3AlF_6 in flux 44%NaCl-56%KCl-Na_3AlF_6 are 5, 10, 15 and 20%, respectively. Concentrations of other elements not shown in the table are lower than 0.05%.

Cryolite	Cu	Mg	Mn	Fe	Si	Ti	Na	K	Cl	Al
5%	4.14	/	0.619	0.137	0.157	0.047	0.012	0.033	0.047	94.89
10%	4.15	/	0.644	0.140	0.151	0.030	0.044	0.170	0.236	94.17
15%	4.12	/	0.620	0.126	0.163	0.031	0.096	0.045	0.187	94.66
20%	4.17	/	0.640	0.129	0.144	0.034	0.118	0.106	0.281	94.21

Figure 3.15 is the XRD result of the dross which was obtained after water leaching and filtering the flux including 10% cryolite after refining. The phase composition of the dross is different from that of using 70%NaCl-30%KCl-Na_3AlF_6 system though the addition amount of cryolite is the same. All Na_3AlF_6 has been depleted during refining and $NaMgF_3$ and $KMgF_3$ were formed after the reactions between Mg and molten flux. K_2NaAlF_6 phase which was found in 70%NaCl-30%KCl-Na_3AlF_6 system disappeared completely. The most possible formation mechanism of $KMgF_3$ is that the Na^+ of partial $NaMgF_3$ compounds was completely substituted by the K^+ in the molten flux [27]. Moreover, a small quantity of Na_3AlF_6 decomposed to AlF_3 and NaF during refining. This decomposition is also the reason for $AlF_3 \cdot 3H_2O$ formation in the dross considering that molten Al can not react with NaF, KF or MgF_2 to obtain F^-. The AlF_3 which was provided by Na_3AlF_6 decomposition reacted with H_2O during water leaching and left $AlF_3 \cdot 3H_2O$ phase in the slag after filtering.

Compared with 70%NaCl-30%KCl-Na$_3$AlF$_6$ system, Na$_3$AlF$_6$ is more active in the 44%NaCl-56%KCl-Na$_3$AlF$_6$ which has a lower viscosity, and the diffusion of phases and elements is more convenient to accelerate the reactions due to the improved fluidity of molten flux. Again, MgO and MgAl$_2$O$_4$ were not found in the dross.
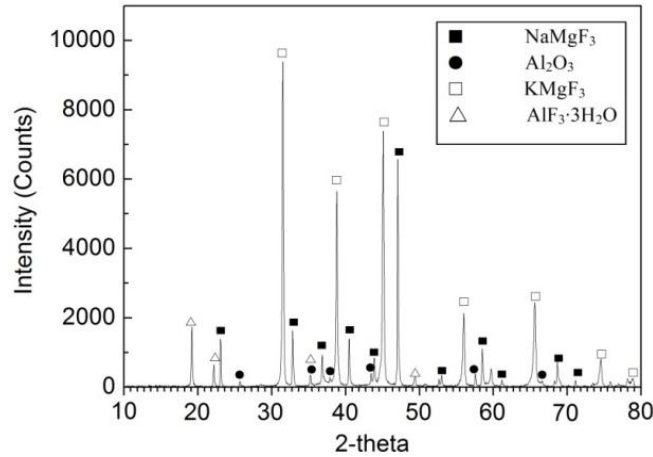
Figure 3.15. XRD patterns of dross after water leaching salt slag which is obtained after re-melting and refining with salt flux 44%NaCl-56%KCl-10%Na$_3$AlF$_6$.

In summary, 10% additional cryolite in equimolar NaCl-KCl salt flux is preferred considering the recovered Al alloy quality together with the economic factor (higher metal yield with less cryolite addtion). The yield of big metal beads (> 2 mm) is 97.3% when the additional cryolite in salts is 10%, which is slightly higher than that of 70%NaCl-30%KCl salt flux with 10% additional cryolite, 96.8%. Equimolar NaCl-KCl gives better metal coalescence than the salt flux composition based on 70%NaCl–30%KCl. The concentrations of major alloying elements and impurity elements in the recovered Al alloys are consistent with nominal composition of 2024 alloy except Mg, and the Mg loss is caused by the reaction between Mg and cryolite.

3.5.1.2 Influence of refining temperature

Refining temperature is an important factor to energy cost and the quality of the aluminium alloy. Lower refining temperature is favourable if the quality of the recovered Al alloy at this temperature can meet the requirement. In order to understand the effect of refining temperature on the metal yield and quality, the refining experiments were also accomplished at 720 ^{o}C and 760 ^{o}C, respectively *(Experiments 12-15)*. To facilitate the comparison with the results from refining at 800 ^{o}C, the salt flux compositions with two different ratios of NaCl to KCl were studied, and the weight ratio of NaCl-KCl salts mixture to Al scrap was set to 2. The additional Na$_3$AlF$_6$ is 10% for all experiments. Similarly, all tests were conducted under nitrogen atmosphere.
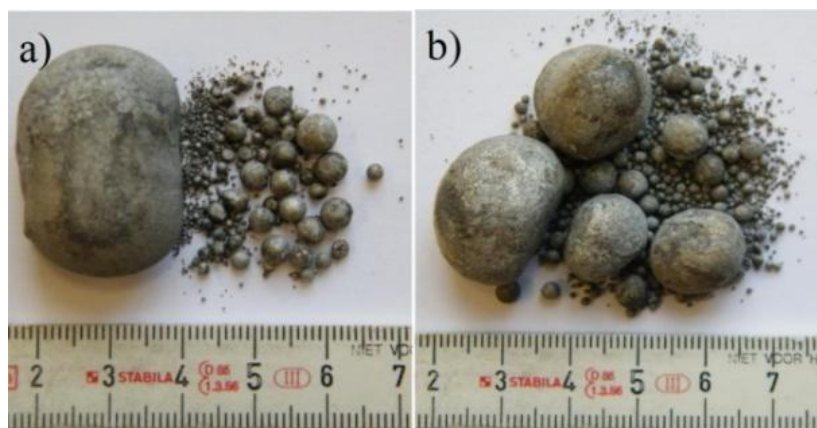
Figure 3.16. Recovered Al alloys after refining at 720 ^{o}C with flux a) 44%NaCl-56%KCl-10%Na$_3$AlF$_6$ and b) 70%NaCl-30%KCl-10%Na$_3$AlF$_6$.
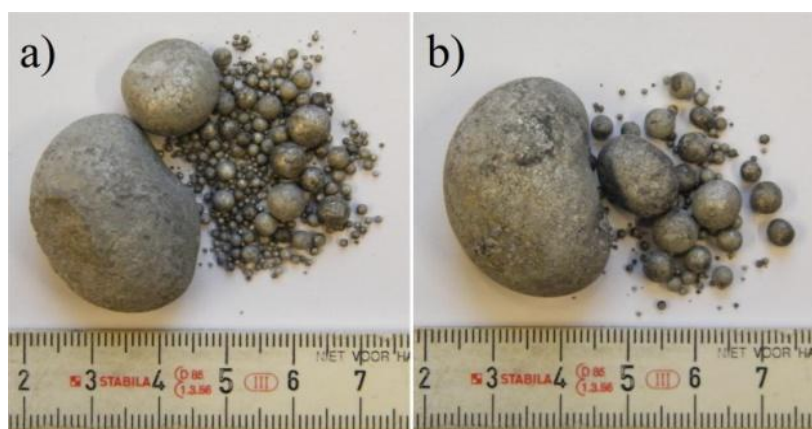
Figure 3.17. Recovered Al alloys after refining at 760 ^{o}C with flux a) 44%NaCl-56%KCl-10%Na$_3$AlF$_6$ and b) 70% NaCl-30% KCl-10% Na$_3$AlF$_6$.

The Al alloys after refining were presented in Figure 3.16 and 3.17. The effect of weight ratio of NaCl to KCl in salt flux on metal coalescence was obvious especially for the refining results at 720 ^{o}C, which is similar to the refining results at 800 ^{o}C. One big metal bead together with a small quantity of small beads were obtained after using flux based on equimolar NaCl-KCl system, as shown in Figure 3.16 a). But a few metal beads with smaller size were formed during refining with flux based on 70%NaCl-30%KCl because of relatively weakened metal coalescence ability, as shown in Figure 3.16 b). The similar situation occurred in the refining at 760 ^{o}C, as we can see in Figure 3.17.
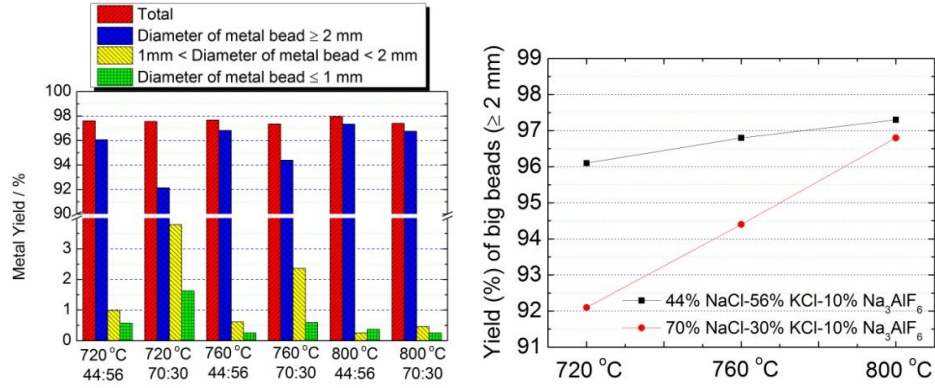
Figure 3.18. Metal yields after refining at different temperatures. All additional cryolites in fluxes 44%NaCl-56%KCl-Na$_3$AlF$_6$ and 70%NaCl-30%KCl-Na$_3$AlF$_6$ are 10%.

The effect of refining temperature on metal yield is shown in Figure 3.18. Though the total metal yields are very close to each other, the difference between the yields of big metal beads which is one of important criteria for refining quality is visible. The yield of big metal beads after refining with 44%NaCl-56%KCl-10%Na$_3$AlF$_6$ flux system is 96.1, 96.8 and 97.3% when the refining temperature is 720 ^{o}C, 760 ^{o}C and 800 ^{o}C, respectively. For 70%NaCl-30%KCl-10%Na$_3$AlF$_6$ flux system, the yield of big size beads is lower, 92.1% at 720 ^{o}C, 94.4% at 760 ^{o}C and 96.8% at 800 ^{o}C. The influence of refining temperature on the yield of big size beads was more significant for flux based on 70%NaCl-30%KCl system where the yield increment is 5.7% when the refining temperature increases from 720 ^{o}C to 800 ^{o}C. But the yield increment was only 1.2% when the temperature changes from 720 ^{o}C to 800 ^{o}C for flux based on 44%NaCl-56%KCl system.

To estimate the viscosity of molten salt, Vogel-Fulcher-Tamman-Hesse (VFTH) equation is usually used which reads η(T)=A×exp(Q/RT), where η(T) is the viscosity, A is a constant, Q is the activation energy, R is the universal gas law constant and T is the absolute temperature [28]. It indicates that the viscosity of molten salt is increased with decreasing temperature. Flux fluidity decreased with decreasing temperature, drop in fluidity of flux will cause the formation of salt inclusions in molten metal which directly and/or indirectly cause the pore formation. The metal coalescence of metal droplets in the flux also decreased with increasing viscosity.

In this research, where the scrap is clean after delamination and ultrasonic cleaning, the important factor for refining quality (especially for metal yield) is the fluidity of the metal droplets in flux. Higher temperature is beneficial to the fluidity of liquid metal and molten salts, and can accelerate the coalescence of metal droplets, this is the reason for yield increases with refining temperature. The effect of the ratio of NaCl to KCl in salt mixture was also caused by the lower melting point of equimolar NaCl and KCl system, which is helpful to metal coalescence during refining.

The compositions of recovered Al alloys at different refining temperatures are shown in Table 3.5. Mg was removed from Al alloy to salt flux by the reaction between Mg and cryolite, the same as refining results at 800 ^{o}C. Other alloying elements were well kept in the aluminium alloy. Just a small amount of chlorides was entrapped, but it is easily removed during industrial scale refining.

Table 3.5 Compositions (%) of obtained 2024 Al alloys after refining with NaCl-KCl-10% Na$_3$AlF$_6$ fluxes at different refining temperatures, and the weight ratio of NaCl to KCl is 70:30 and 44:56, respectively. Concentrations of other elements not shown in the table are lower than 0.05%.

	NaCl:KCl	Cu	Mg	Mn	Fe	Si	Ti	Na	K	Cl	Al
720 ^{o}C	70:30	4.45	/	0.656	0.139	0.162	0.026	0.071	0.060	0.165	94.32
	44:56	4.55	/	0.701	0.144	0.166	0.029	0.085	0.069	0.190	93.24
760 ^{o}C	70:30	4.50	/	0.666	0.159	0.159	0.024	0.071	0.063	0.172	93.23
	44:56	4.42	/	0.660	0.143	0.173	0.027	0.019	0.142	0.159	93.72

3.5.1.3 Influence of refining atmosphere

The effect of refining atmosphere on the refining result especially for the metal yield was studied (***Experiments 16-17** were carried out under air atmosphere)*. The salt flux compositions with the same two different ratios of NaCl to KCl were employed, and the weight ratio of NaCl-KCl salts mixture to Al scrap was again set to 2. The additional Na$_3$AlF$_6$ in the slats is 10% for all experiments, which were all conducted at 800 ^{o}C.

The recovered Al alloys are shown in Figure 3.19. The refining atmosphere has little influence on metal coalescence, and the recovered alloy consists of one big size metal bead with and some small metal beads for both salt fluxes.
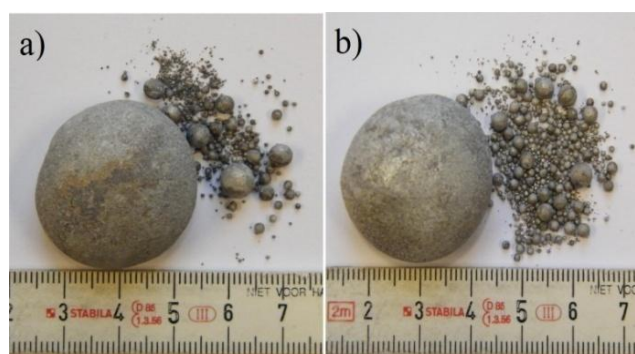
Figure 3.19. 2024 Al alloys after refining at 800 ^{o}C under air atmosphere, the used flux is a) 70%NaCl-30%KCl-10%Na$_3$AlF$_6$ and b) 44%NaCl-56%KCl-10%Na$_3$AlF$_6$, respectively.
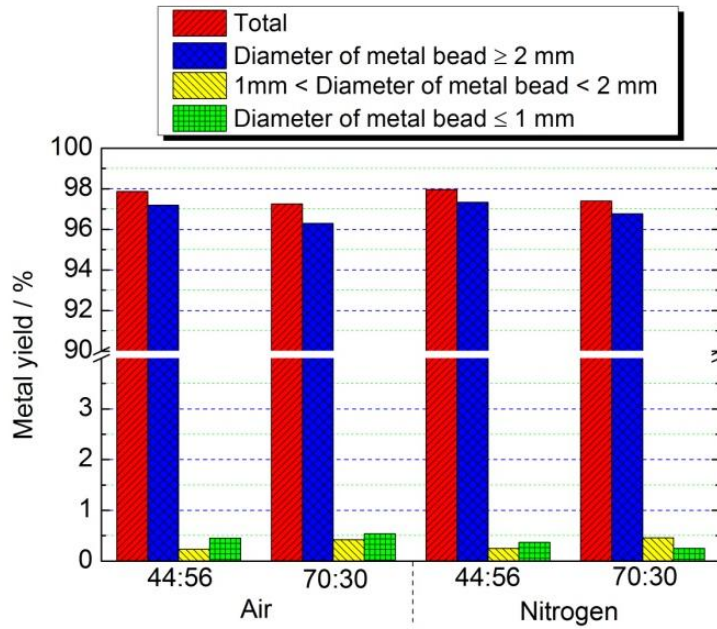
Figure 3.20. Metal yields after refining at 800 ^{o}C under air and nitrogen atmosphere. All additional cryolites in fluxes 44%NaCl-56%KCl-Na$_3$AlF$_6$ and 70%NaCl-30%KCl-Na$_3$AlF$_6$ are 10%.

The yield of big beads after refining under air is 97.2 and 96.3% when the used fluxes are 44%NaCl-56%KCl-10%Na$_3$AlF$_6$ and 70%NaCl-30%KCl-10%Na$_3$AlF$_6$, respectively, as shown in Figure 3.20. The decrement for big metal beads yield is 0.1 and 0.5%, respectively, compared to refining results under nitrogen atmosphere. The satisfying yield after refining without nitrogen protection is attributed to the ample salt flux. The molten salt flux has a lower density than liquid aluminium alloy, and will stay on the top and cover the molten aluminium alloy, which can significantly prevent the oxidation behaviour in air under high temperature. The ample salt flux plays a similar role as nitrogen atmosphere during refining.

Table 3.6. Compositions (%) of 2024 Al alloys after refining with NaCl-KCl-10% Na$_3$AlF$_6$ fluxes at 800 ^{o}C under air atmosphere, the weight ratio of NaCl to KCl is 70:30 and 44:56, respectively. Concentrations of other elements not shown in the table are lower than 0.05%.

Weight ratio of NaCl to KCl	Cu	Mg	Mn	Fe	Si	Ti	Na	K	Cl	Al
70:30	4.38	/	0.656	0.145	0.158	0.023	0.104	0.128	0.279	93.43
44:56	4.15	/	0.638	0.136	0.162	0.035	0.075	0.036	0.159	94.61

The compositions of recovered Al alloys are listed in Table 3.6. Similar to refining result under nitrogen atmosphere, all Mg was lost because of the reaction between Mg and

cryolite, and other alloying elements were well controlled. A small quantity of NaCl and KCl was entrapped, but it is easily removed during industrial scale refining. Combining with the results of metal yield, it can be concluded that the inert atmosphere is not absolutely essential when the weight of salt to alloy is sufficiently high in refining. But for the case of using rotary furnace, the Al melt may be exposed to furnace atmosphere, the situation will be different from our experiments.

3.5.1.4 Influence of Al scrap size

It was reported in the literature that the size of Al scrap has an important influence on refining result, and both the metal yield and the product (metal beads) size distribution are highly affected by the size distribution of Al scrap [19]. Three different scrap sizes were selected in this work to quantify this correlation and to gain more insight into the melting behaviour in relation to the scrap size *(Experiments 18-20)*. As shown in Figure 3.21, three different sizes of Al scrap are 20 mm×15 mm, 10 mm×10 mm and 5 mm×5 mm with the same thickness of about 0.4 mm, respectively.

The selected salt flux composition was 44%NaCl-56%KCl-10%Na$_3$AlF$_6$, and the weight ratios of NaCl-KCl salts mixture to Al scrap were 2, all tests were executed in nitrogen atmosphere at 800 ^{o}C.
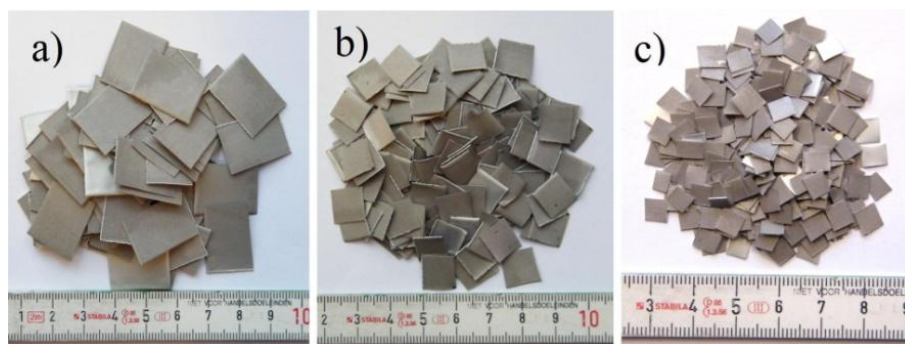
Figure 3.21. 2024 Al alloy scrap with different sizes. a) 20×15 mm, b) 10×10 mm and c) 5×5 mm.

The recovered Al alloys are shown in Figure 3.22. The coalescence situation of metal droplets in refining of 5 mm×5 mm scrap is obviously worse than others and more small size beads were generated. Difference of coalescence ability between 20 mm×15 mm and 10 mm×10 mm scrap refining is small. The metal yields are obtained after sieving, which is presented in Figure 3.23. Though the total metal yields are very close to each other, the yields of big metal beads (> 2 mm) are 97.1 (20 mm×15 mm), 97.0 (10 mm×10 mm) and 95.5% (5 mm×5 mm), respectively. While the big metal beads yield after refining of 35×25 mm Al scrap is 97.3%, just a little higher than that of refining of 20 mm×15 mm Al scrap. The discrepancy of big metal beads yield is distinct, especially for the 5 mm×5 mm scrap. Both the weight fractions of metal beads with 1-2 mm size and smaller than 1 mm size are increased with decreasing of initial scrap size. The lower metal yield for the

smaller size scrap refining is mainly due to more oxides on the higher specific surface area. This effect increases with the reduction in metal scrap size. According to the results, the scrap size bigger than 10 mm ×10 mm should be selected.
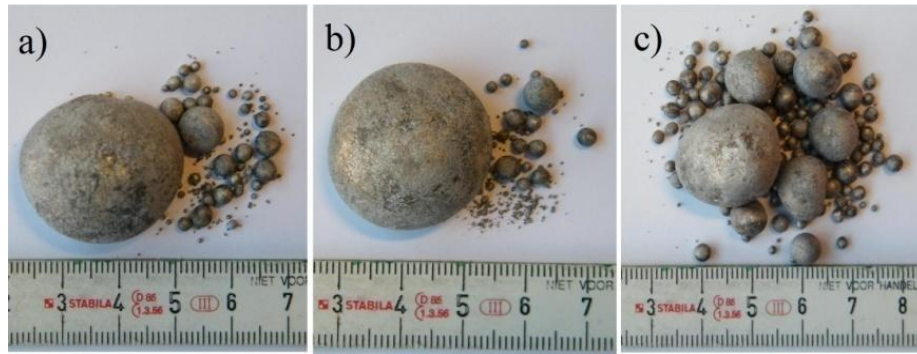
Figure 3.22. 2024 Al alloys after refining with different scrap size. a) 20 mm×15 mm, b) 10 mm×10 mm and c) 5 mm×5 mm.
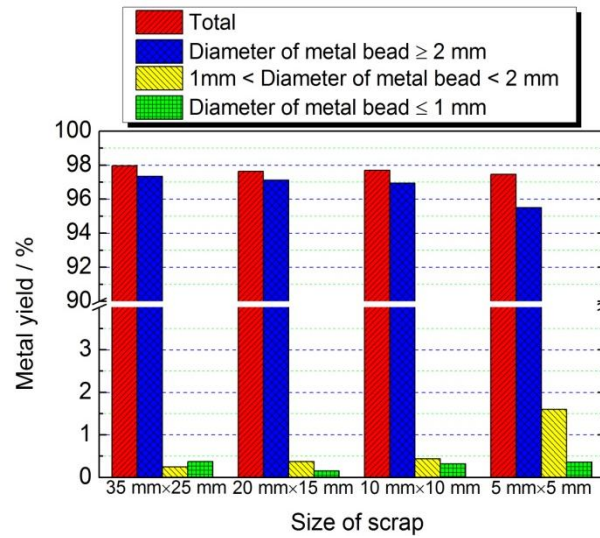
Figure 3.23. Metal yields after refining of different sizes 2024 Al scrap.

The inner morphology of the recovered Al alloy is shown in Figure 3.24. No obvious defects were observed even for the scrap size of 5 mm×5 mm, which indicated a good quality of recovered Al alloy.
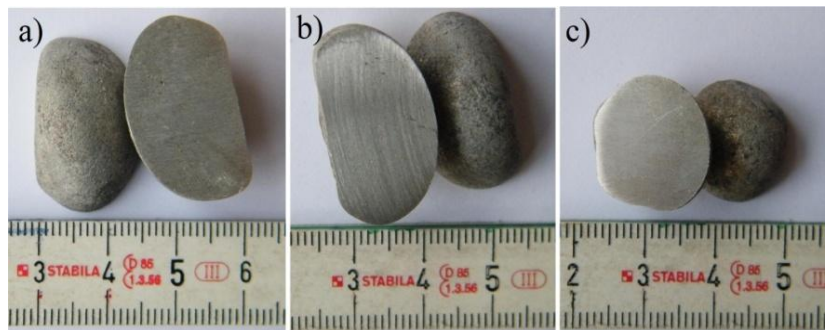
Figure 3.24. The inner morphology of recovered 2024 Al alloys. Al alloy scrap size: a) 20 mm×15 mm, b) 10 mm×10 mm and c) 5 mm×5 mm during refining.

Compositions of Al alloys after refining of different size scrap are listed in Table 3.7. Mg in Al scrap was consumed by cryolite but other alloying elements such as Mn and Cu were well controlled. The concentrations of impurity elements Fe, Si and Ti in recovered Al alloys also meet the nominal composition requirements of commercial 2024 Al alloy. Moreover, the results indicated that the entrapped chloride amount in recovered Al alloy was decreased with the scrap size.

Table 3.7 Compositions (%) of 2024 Al alloys after refining of different sizes Al alloy scrap. Concentrations of other elements not shown in the table are lower than 0.05%.

Size of Al scrap (mm ×mm)	Cu	Mg	Mn	Fe	Si	Ti	Na	K	Cl	Al
5×5	4.44	/	0.659	0.148	0.155	0.03	0.024	0.018	0.057	94.42
10×10	4.26	/	0.640	0.132	0.165	0.032	0.042	0.040	0.105	94.63
20×15	4.42	/	0.677	0.143	0.157	0.030	0.051	0.072	0.145	94.14

3.5.1.5 Influence of ratio of NaCl-KCl salt mixture to Al scrap

The ratio of salt flux to metal is a critical factor for the quality of recovered Al alloy, which is also important for economic cost and environment protection. Thus it is preferred to obtain high quality recovered aluminium with satisfied metal yield by using salts as little as possible. The composition of used salt flux was 44%NaCl-56%KCl-10%Na$_3$AlF$_6$ and three different weight ratios of NaCl-KCl salts mixture to Al scrap were selected in this study: 1.5, 1.0 and 0.5 **(Experiments 21-23)**. The size of Al scrap is 10 mm ×10 mm. All tests were conducted in nitrogen atmosphere at 800 $^{\circ}$C.

Figure 3.25. 2024 Al alloys after refining with flux 44%NaCl-56%KCl-10%Na$_3$AlF$_6$, and the weight ratio of NaCl-KCl salts mixture to 2024 Al scrap is a) 1.5:1, b) 1:1 and c) 0.5:1, respectively.

Figure 3.25 shows the obtained 2024 Al alloys after refining with different amounts of salt flux. As can be seen from Figure 3.25, the weight ratio of small size metal beads is increased with the decreasing salts amount, indicating that the aggregation ability of liquid metal is reduced with the salts amount. The ample salt flux can provide more opportunities for salt/oxide interaction. On the other hand, the concentration of dissolved oxides and coating residues in the flux decreased with the increasing salt flux. Lower oxide concentration is in favour of the fluidity of salt flux which is important to metal coalescence.
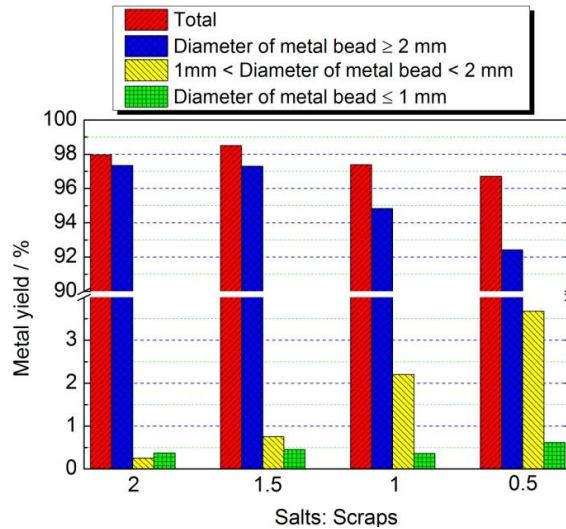
Figure 3.26. 2024 Al alloys yields after refining with flux 44%NaCl-56%KCl-10% Na$_3$AlF$_6$, and the weight ratio of NaCl-KCl salts mixture to 2024 Al scrap is 2:1, 1.5:1, 1:1 and 0.5:1, respectively.

The metal yields after refining are listed in Figure 3.26. Both total metal yield and the yield of big metal beads (>2 mm) are obviously decreased with decreasing the amount of salt

flux. The big metal beads yield is 97.1, 94.8, and 92.4% when the weight ratio of salt flux to Al scrap is 1.5, 1.0 and 0.5, respectively. The big metal beads yield is 97.3% when the weight ratio of salt flux to Al scrap is 2, as mentioned above. The metal yield was drastically decreased when the weight ratio of salt flux to Al scrap was lower than 1.5. The metal yield decreased with the salt flux amount is attributed to the reduced fluidity of salt flux and decreased metal coalescence capacity. It should be pointed out that the selection of salts amount heavily depends on the contamination situation of scrap.

Figure 3.27. 2024 Al alloy inner morphology after refining with flux 44%NaCl-56%KCl-10%Na₃AlF₆, and the weight ratio of NaCl-KCl salts mixture to 2024 Al scrap is 1.5:1, 1:1 and 0.5:1, respectively.

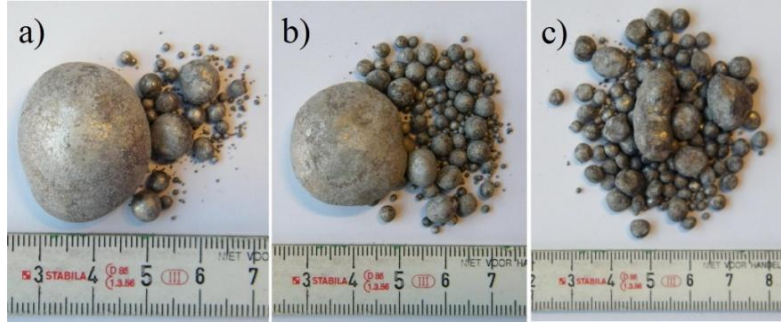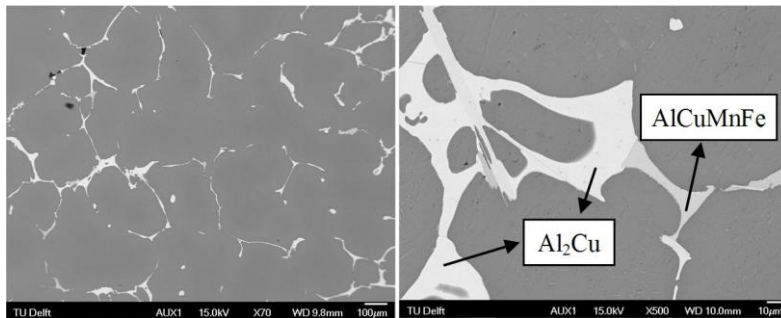*Figure 3.28. SEM patterns of obtained 2024 Al alloys after refining with flux 44%NaCl-56%KCl-10%Na₃AlF₆, and the weight ratio of NaCl-KCl salts mixture to 2024 Al scrap is 1.5:1, 1:1 and 0.5:1 respectively.*

The inner morphology and SEM patterns of the recovered Al alloys are presented in Figure 3.27 and 3.28. The inner quality of recovered Al alloy is generally acceptable even the ratio of flux to scrap was only 0.5. The major phases besides Al matrix are Al_2Cu and AlCuMnFe, the absence of AlCuMg ternary phase was caused by the Mg loss during refining, as mentioned before.

The compositions of recovered Al alloys are listed in Table 3.8. Some Mg was kept in the recovered Al alloy when the weight ratio of salts to scrap is 0.5, which is caused by the insufficient cryolite. Assuming that all cryolite has reacted with Mg during re-melting and

refining, the depleted Mg mass ratio can be calculated based on the reaction equation (3-3), and the calculated Mg loss is 0.87% when the weight ratio of salts to scrap is 0.5. Thus the remaining Mg is about 0.26% which is close to the measured value of 0.30%. Other alloying elements such as Mn and Cu were similar to the original content, and the concentrations of impurity elements Fe, Si and Ti in the recovered Al alloys also meet the nominal composition requirements of the commercial 2024 Al alloy. But again, a small amount of NaCl and KCl was entrapped.

Table 3.8 Compositions (%) of obtained 2024 Al alloys after refining with flux 44%NaCl-56%KCl-10%Na$_3$AlF$_6$, with different weight ratios of NaCl-KCl salts mixture to scrap.

Ratio of salts to scrap	Cu	Mg	Mn	Fe	Si	Ti	Na	K	Cl	Al
1.5	4.35	/	0.650	0.135	0.142	0.033	0.081	0.027	0.152	94.55
1	4.21	/	0.650	0.134	0.160	0.029	0.066	0.089	0.207	94.28
0.5	4.02	0.30	0.633	0.124	0.158	0.029	0.135	0.039	0.249	93.97

3.5.2 Refining with flux NaCl-KCl-MgF$_2$

Since Mg was lost from the reaction between the alloy scrap and cryolite during the refining. MgF$_2$ was selected as additional fluoride in the NaCl-KCl salts mixture to prevent Mg loss. Though the influence of MgF$_2$ on metal coalescence capacity is lower than that of cryolite, SrF$_2$, BaF$_2$, LiF and CaF$_2$, its positive influence on metal yield is attractive.

3.5.2.1 Influence of MgF$_2$ amount in the salt

The size of 2024 Al scrap for refining is 35 mm×25 mm with a thickness of 0.4 mm. The refining temperatures for all tests *(Experiments 24-27)* were 800 ^{o}C, and all tests were conducted under nitrogen atmosphere. Flux based on equimolar NaCl-KCl was selected, and the weight ratio of salt to Al scrap was set to 2. The additional MgF$_2$ in the salt mixture is 5, 10, 15 and 20%.

The recovered Al alloys are illustrated in Figure 3.29. Different with the influence of cryolite on metal aggregation behaviour, the increase of MgF$_2$ leads to formation of more small size beads, indicating that the metal coalescence capacity is reduced with increasing the amount of MgF$_2$ in the salt flux. The possible reason for that is the viscosity of the molten slat flux is increased with MgF$_2$ amount and the high viscosity is unfavourable for the movement of aluminium droplets and the separation from the salt. Comparing with the refining by using cryolite addition in the salt flux, the disadvantage of MgF$_2$ addition on coalescence capacity is visible and many pits caused by the neighbouring beads were found on the surface of recovered metal beads, indicating that the neighbouring droplets cannot aggregate completely to one big bead.
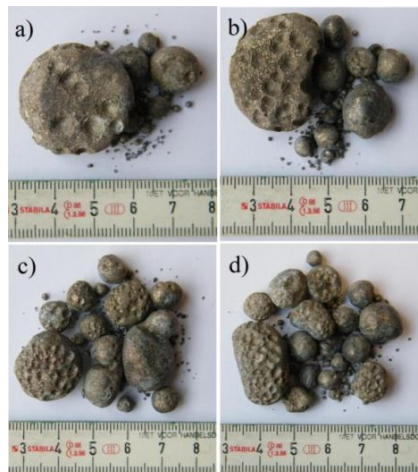
Figure 3.29. Al alloy after refining with the ratio of NaCl to KCl is 44:56 in salts. a) 5% MgF_2, b) 10% MgF_2, c) 15% MgF_2 and d) 20% MgF_2.

The total metal yields are very close though the MgF_2 addition amounts are different, all total metal yields are about 98.5%, as we can see from Figure 3.30. The obtained results are different with the research results of Van Linden et al. [17] who found that the metal yield was increased with the increase of MgF_2 concentrations up to 10%. The big beads yield is 97.8, 97.7, 97,2 and 96.8% when the additional MgF_2 in salt flux is 5, 10, 15 and 20%, respectively. Big metal beads yield in this work was also decreased with MgF_2 addition amount, especially when the amount is greater than 5%, which is also attributed to the increased viscosity with increasing amount of MgF_2 in flux.
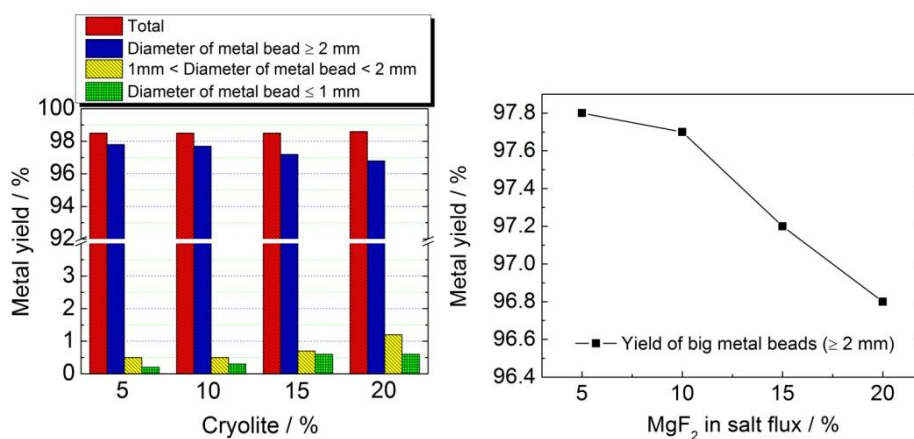
Figure 3.30. Metal yields of recovered Al alloys after refining with flux 44%NaCl-56%KCl-MgF_2. MgF_2 addition in the flux is 5, 10, 15 and 20%, respectively.

79
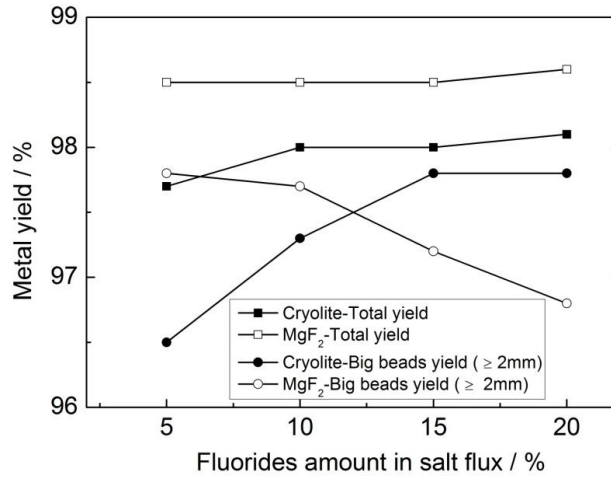
Figure 3.31. Metal yields after Al alloy scrap refining by using 44%NaCl-56%KCl salt flux with additional cryolite (Na₃AlF₆) or MgF₂.

The comparison of metal yields after using cryolite or MgF_2 as additional fluorides in the salt flux was shown in Figure 3.31. The total metal yields in the case of MgF_2 addition are obviously higher than those of cryolite addition. The big beads yields with MgF_2 addition are also higher than those with cryolite addition when the fluoride addition amount is lower, but the situation is reversed when the fluoride addition amount is increased to a higher level, as shown in Figure 3.31.

For total metal yields, comparing with cryolite addition, the yield increment with MgF_2 addition is 0.8, 0.5, 0.5 and 0.5%, respectively when the fluoride addition is 5, 10, 15 and 20%. Mg was kept in recovered alloys after using MgF_2 as additional fluorides, while Al in Na_3AlF_6 was substituted by Mg during refining with additional cryolite in salt flux. The Al alloy weight loss of 0.28% caused by the reaction between Mg and cryolite (equation 3-3) can be calculated after considering that all lost electrons from Mg were obtained by the Al^{3+} in Na_3AlF_6 while assuming that all 1.13% Mg in 2024 Al scrap is completely lost. Therefore, the MgF_2 has similar performance as cryolite on the salt/oxide interaction, most of aluminium enclosed by oxide layers on surface of Al scrap has been recovered.

For big beads yield, the increment is about 1.3% when 5% cryolite is replaced by MgF_2 in the flux, but this increment is decreased to 0.31% when the fluoride addition is 10%. Above this content, the big beads yield with MgF_2 addition becomes lower than that with cryolite addition. The discrepancy is 0.6 and 1.0% when the fluoride addition is 15 and 20%, respectively. Considering that 0.28% Al alloy mass loss caused by reaction between Mg and cryolite, thus it can be concluded that influence of MgF_2 addition on improvement of metal coalescence capacity is slightly inferior compared to cryolite addition when the addition amount is higher than 10%. The reason for this is the significantly increased viscosity of molten flux when the MgF_2 addition in salt flux is higher than 10%.

Table 3.9 Compositions (%) of 2024 Al alloy after refining. The additions of MgF_2 in equimolar NaCl-KCl salts are 5%, 10%, 15% and 20%. Concentrations of other elements not shown in the table are lower than 0.05%.

MgF_2 addition	Cu	Mg	Mn	Fe	Si	Ti	Na	K	Cl	Al
2024 in Glare	4.37	1.13	0.642	0.126	0.165	0.030	/	/	/	93.45
5%	3.94	1.02	0.592	0.114	0.143	0.030	0.006	0.013	0.043	94.16
10%	4.05	0.99	0.618	0.128	0.148	0.027	0.012	0.022	0.110	93.92
15%	3.97	1.00	0.590	0.113	0.135	0.038	/	0.032	0.066	94.03
20%	4.07	1.04	0.602	0.121	0.154	0.032	0.010	0.018	0.036	93.97

The compositions of recovered Al alloys with using MgF_2 as the additional fluoride in the salt flux are listed in Table 3.9. Mg and other alloying elements were well controlled, and the concentrations of impurity elements Fe, Si and Ti in the recovered Al alloys also meet the nominal composition requirements of commercial 2024 Al alloy. The amount of entrapped salts is slightly lower than that of cryolite addition, indicating that salt flux with MgF_2 addition has a higher metal/salt interfacial tension which is consistent with previous research [3]. But the higher viscosity of the flux with MgF_2 addition inhibits the coalescence of droplets, leading to a lower coalescence ability compared to the flux with cryolite addition.
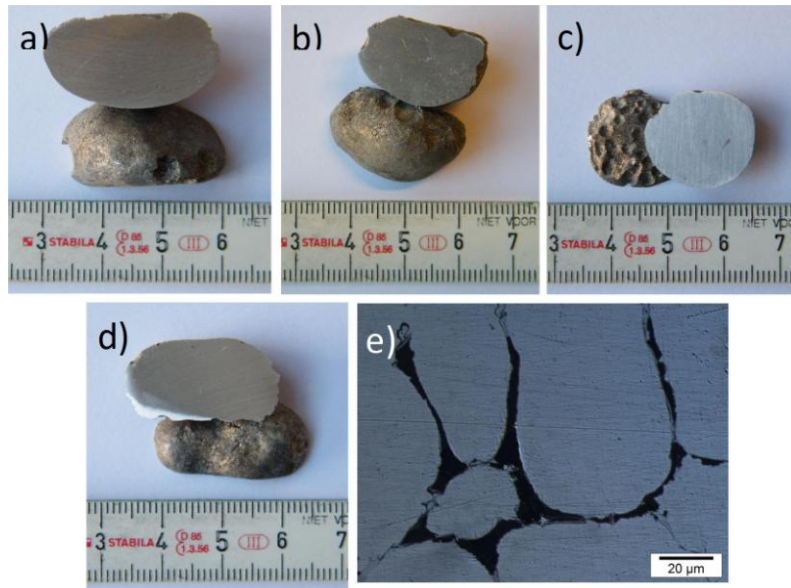
Figure 3.32. Inner morphology of the recovered Al alloys. MgF_2 addition in flux 44%NaCl-56%KCl-MgF_2 is a) 5, b) 10, c) 15 and d) 20%. e) is the high magnification picture of a), the holes in the grain boundary are formed because of the exfoliation of entrapped salts during polish.
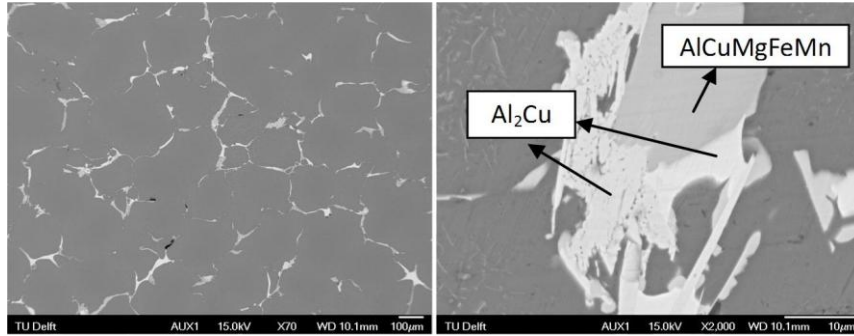
Figure 3.33. SEM photos of 2024 Al alloy after refining with 44%NaCl-56%KCl-5%MgF$_2$. a) low magnification (×70) and b) high magnification (×2000).

The inner morphology and SEM photos of obtained 2024 Al alloys after refining with 44%NaCl-56%KCl-MgF$_2$ were shown in Figure 3.32 and 3.33. No obvious defects were observed besides some micro holes in the grain boundary caused by the exfoliation of entrapped salts during polish (Figure 3.32 e)). The primary phases besides Al matrix were Al$_2$Cu and AlCuMgFeMn. Inclusions such as MgO and Al$_2$O$_3$ particles have not been found in the recovered Al alloy.
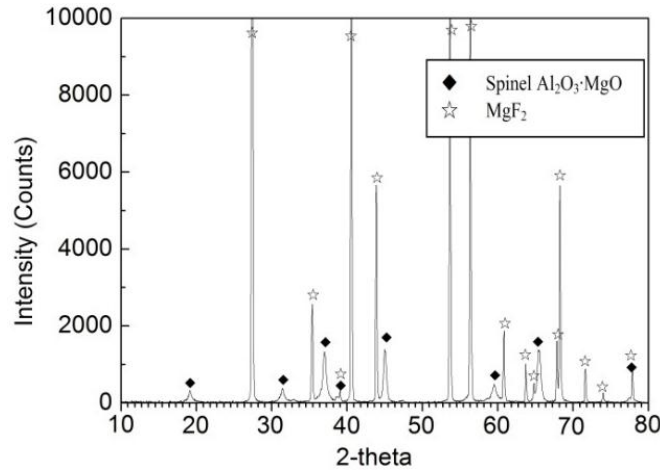
Figure 3.34. XRD patterns of the dross after water leaching of salt slag which is obtained after re-melting and refining with salt flux 44%NaCl-56%KCl-5%MgF$_2$.

The dross obtained after water leaching of the salt slags was analyzed by XRD to better understand the behaviour of the flux during refining. The phase composition of the dross obtained from 44%NaCl-56%KCl with additional 5% MgF$_2$ is presented in Figure 3.34. The main phases in the dross are MgF$_2$ and MgAl$_2$O$_4$. Plently of MgF$_2$ was detected because of its low solubility (0.13 g/l) in water. As mentioned before, the formation of MgO and MgAl$_2$O$_4$ (spinel) was caused by the reactions between Mg and Al$_2$O$_3$. The Al$_2$O$_3$ in the

$MgAl_2O_4$ (spinel) was primarily introduced by the Al alloy scrap. Chlorides were not observed after water leaching because the NaCl and KCl cannot react with any alloying element in alloy and the NaCl and KCl dissolved into water during leaching. Mg and other alloying elements in Al scrap cannot react with MgF_2 during refining, and thus no other fluoride was found in the dross.

3.5.2.2 Influence of weight ratio of NaCl-KCl mixture to Al scrap

The effect of weight ratio of NaCl-KCl salts to Al scrap on Al refining was investigated. The weight ratio of 0.5 had unsatisfied metal coalescence capacity and metal yield when cryolite was added in salt flux, two different weight ratios of 1.5 and 1.0 are selected for MgF_2 addition system **(Experiments 28-29)**. The size of the used Al scrap is 35 mm$\times$25 mm. All tests were executed in nitrogen atmosphere at 800 ^{o}C, and the salt flux composition was equimolar NaCl-KCl salts with 5% additional MgF_2.

Figure 3.35 shows the obtained Al alloys after refining with different weight ratios of salts to Al scrap. As we can see from Figure 3.35, both the recovered Al alloys consist of plenty of small size metal beads though the weight ratios are 1.5 and 1. The metal coalescence capacity was obviously decreased compared to the refining with weight ratio of 2.

Figure 3.35. 2024 Al alloys after refining with flux 44%NaCl-56%KCl-5%MgF₂, and the weight ratio of salts to scrap is a) 1.5:1 and b) 1:1.

The metal yields after refining are illustrated in Figure 3.36. Both total metal yield and big metal beads yield ($\geq$ 2 mm) are close to each other for weight ratio of 1.5 and 1.0, the total metal yield is about 98.5% and the big metal beads yield is about 96.5% for both cases. Compared with the refining result with weight ratio of 2, the total metal yield is the same, but the decrement of big beads yield is about 1.2%. The concentration of the dissolved oxides and coating residues in flux decreased with the increasing salt flux, lower oxides concentration is in favour for the fluidity of salt flux which is important to metal coalescence. Thus the decreased big beads yield is attributed to the decreased metal coalescence capacity.
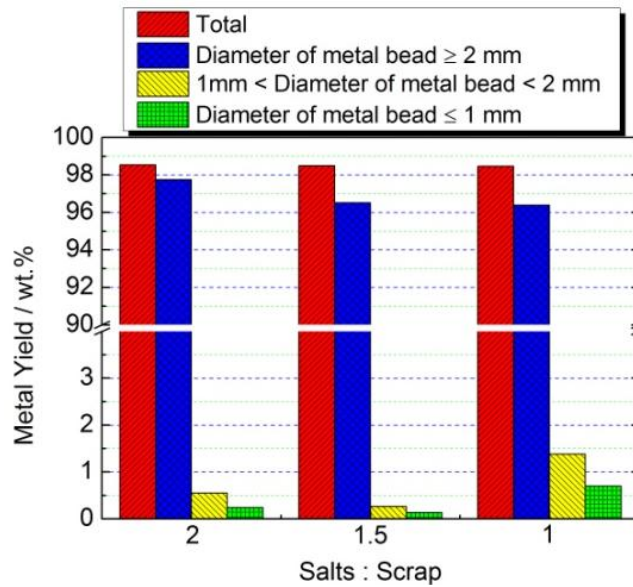
Figure 3.36. 2024 Al alloys yields after refining with flux 44%NaCl-56%KCl-5%MgF₂, and the weight ratio of salt mixture to scrap is 2:1, 1.5:1 and 1:1.

The inner morphology of recovered Al alloys is presented in Figure 3.37. No obvious defects were found and the inner quality of recovered Al alloy is attractive.

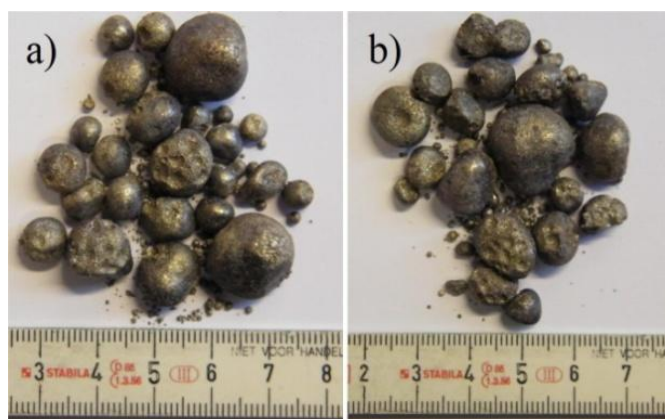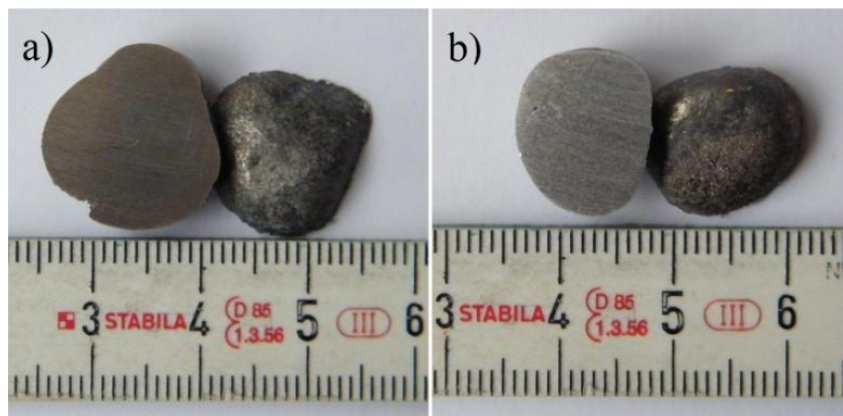*Figure 3.37. 2024 Al alloy inner morphology after refining with flux 44%NaCl-56%KCl-5%MgF₂, and the weight ratio of salt to scrap is a) 1.5:1 and b) 1:1.*

The compositions of the recovered Al alloys are listed in Table 3.10. Alloying elements Mg, Cu and Mn were well kept in the recovered Al alloy for both weight ratios. Similarly, small amount KCl and NaCl were entrapped in the recovered Al alloy.

Table 3.10 Compositions (%) of obtained 2024 Al alloys after refining with flux 44%NaCl-56%KCl-5%MgF$_2$, and the weight ratio of NaCl-KCl salts mixture to 2024 Al scrap is 1.5:1 and 1:1 respectively. Concentrations of other elements not shown in the table are lower than 0.05%.

Ratio of salt to scrap	Cu	Mg	Mn	Fe	Si	Ti	Na	K	Cl	Al
1.5	4.01	0.92	0.607	0.124	0.133	0.036	0.008	0.018	0.040	94.11
1	4.15	1.00	0.557	0.123	0.150	0.035	0.012	0.013	0.067	93.76

3.6 End-of-Life GLARE recycling

Previous chapters focus on new GLARE scrap refining, but fasteners for fuselage assembly are inevitably involved in the recycling of End-of-Life GLARE (old scrap) when the plates are out of service. The effect of the fasteners on the GLARE recycling is important to final Al alloy composition and should be well evaluated. Hi locks served as fasteners (see Figure 3.38 [29]), are usually used in the fuselage assembly because of its excellent properties such as controlled preload or clamp-up, minimum size and weight, simple, quiet and rapid installation [30]. The final Al alloy composition can be calculated according to Hi lock composition and the weight ratio of Hi lock to 2024 Al alloy.

Figure 3.38. Hi locks [29].

3.6.1 Simulation based on synthetic EOL GLARE scrap

Amount of Hi lock for GLARE joining

The weight of Hi locks depends on the material type and amount of Hi lock used for GLARE joining. 27 GLARE plates are employed in each fuselage of Airbus A380, and the

total area is 485 m^2 [31]. But the size details about the 27 GLARE planes have never been reported, therefore an assumption is made that each GLARE plate is square and has the same size to simplify the evaluation. Based on this assumption, the calculated size for each GLARE plate is 4.25 m × 4.25 m. Three rows Hi locks are always used for two neighbour GLARE plates joining [32] and the schematic diagram for joining are illustrated in Figure 3.39, the spacing between two adjacent columns of Hi lock is 25.4 mm (an inch) [33].

Thus, the total perimeter P_T is

$$P_T = 4.25 \times 4 \times 27 = 459 \ m = 459000 \ mm \tag{3-4}$$

Two edges are joined by 3 rows of Hi locks, and therefore 1.5 rows Hi lock is required for each edge. The calculation for Hi locks amount now is possible by combining total perimeter of 27 GLARE planes and the spacing between two adjacent Hi lock columns. The amount of Hi locks ($N_{Hi\ lock}$) used in fuselage of Airbus A380 should be

$$N_{hi\ lock} = 1.5 \times \frac{459000}{25.4} - N_{corner} = 27106 - N_{corner} = 27000 \tag{3-5}$$

N_{corner} is Hi lock amount caused by double counting in each corner of GLARE plates which depends on the arrangement of 27 GLARE plates. It should be subtracted though N_{corner} is very small compared to the total amount of Hi lock. The given value of N_{corner} is 106 in this work, which should be close to the reality.
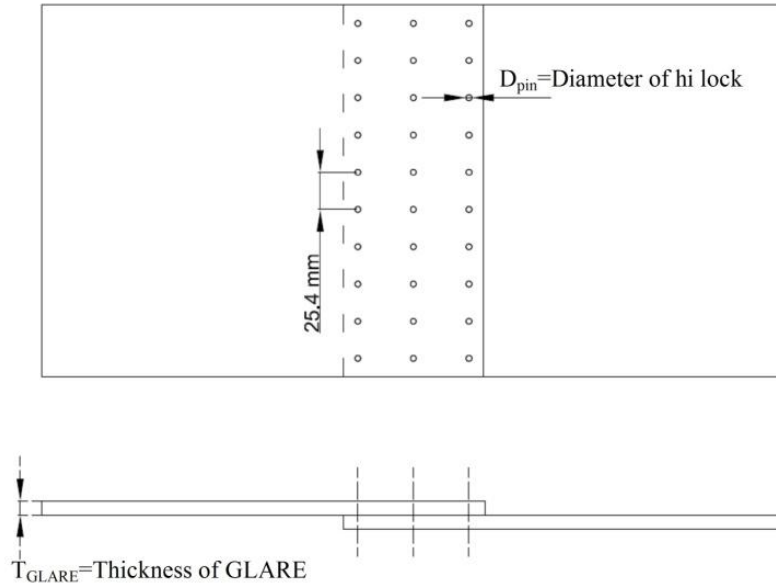
Figure 3.39. Schematic diagram of Hi lock distribution in GLARE.

Hi lock type

The diameters of holes for fasteners are always employed in GLARE plate with sizes of 0.397 cm (5/32 inch) and 0.476 cm (6/32 inch) [32]. Therefore two different diameters for pin of Hi lock are discussed in this evaluation, 5/32 and 6/32 inch, respectively.

Ti-6Al-4V shear Hi lock is frequently used material in the fuselage joining. HL 10 and HL 379 of Hi-Shear Corporation are selected in this evaluation as the pin and collar which are made of material Ti-6Al-4V. The shapes of HL 10 and HL 379 are described in the Figure 3.40.
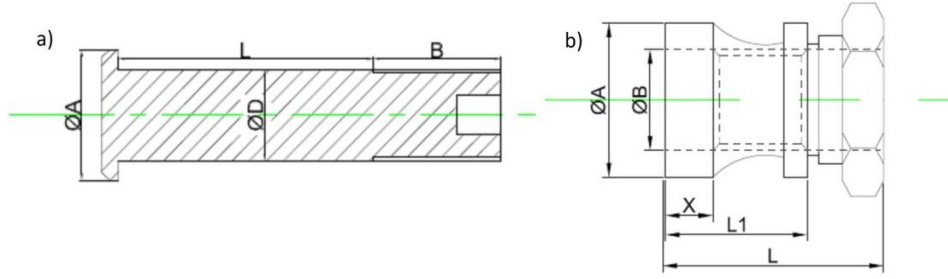
Figure 3. 40. Hi lock. a) Pin HL 10 and b) Collar HL 379 [34].

Total weight of Hi locks

The shape of HL 10 was simplified to a standard cylinder, the volume of pin head can compensate the hole at the end of pin. Similarly, the shape of HL 379 can be simplified to a torus, the diameter of outer circle is $(A_{collar}+B_{collar})/2$ and the diameter of inner circle is B_{collar}. After the simplification treatments, the volumes of HL 10 and HL 279 can be easily obtained. Therefore, the weight of one Hi lock can be approximatively calculated as follows:

$$W_{hl} = W_{pin} + W_{collar} = \pi \times (\frac{D_{pin}}{2})^2 \times (L_{pin} + B_{pin}) \times d_{Ti-6Al-4V} +$$

$$\pi \times \left(\left(\frac{\left(\frac{A_{collar} + B_{collar}}{2} \right)}{2} \right)^2 - \left(\frac{B_{collar}}{2} \right)^2 \right) \times L_{collar} \times d_{Ti-6Al-4V} \tag{3-6}$$

The density of Ti-6Al-4V is 4.44 g/cm^3. The total weight of Hi locks for GLARE joining in fuselage is $27000 \times W_{hl}$. The dimensions of collar and pin are listed in Table 3.11, and

L_{pin} is decided by the total thickness of two GLARE plates for joining and is selected as 0.92 cm (total thickness of two GLARE 3-8/7-0.4 plates) in this evaluation. The calculated total Hi lock weight used for GLARE joining is 40.5 and 52.2 kg when Hi lock with D_{pin} of 5/32 and 6/32 inch is used, respectively.

Table 3.11. Dimensions of pin and collar for different Hi locks (cm).

D_{pin}	Pin			Collar		
	B_{pin}	L_{pin}		A_{collar}	B_{collar}	L_{collar}
0.397 (5/32 inch)	0.792	0.920		0.719	0.422	1.085
0.476 (6/32 inch)	0.826	0.920		0.770	0.528	1.110

Weight of 2024 Al alloy in fuselage

Assuming that all GLARE used in the fuselage is GLARE 3-8/7-0.4 with the thickness of 0.46 cm, the total volume of GLARE plates V_{GLARE} can be obtained as follows:

$$V_{GLARE} = S_{GLARE} \times T_{GLARE} = 4850000 \times 0.46 = 2231000 \ cm^3 \tag{3-7}$$

The weight save of GLARE is 10% compared to bulk 2024 Al alloy [35], therefore the ratio of GLARE density to that of 2024 alloy is 90%, namely 2.5 g/cm^3. By weighting the initial mass of GLARE and the mass of 2024 Al alloy after completely delamination and ultrasonic cleaning, the weight ratio of 2024 Al alloy in GLARE can be obtained, as 67.3%. Now, the total weight of 2024 Al alloy used in the fuselage can be calculated as below:

$$W_{2024Al} = V_{GLARE} \times d_{GLARE} \times R_{2024Al} = 2231000 \times 2.5 \times 67.3\% = 5577500 \ g = 5577.5 \ kg \tag{3-8}$$

Hence, the weight ratios of Hi lock to 2024 alloy are 0.73% and 0.94% when Hi lock with D_{pin} of 5/32 and 6/32 inch is used, respectively.

Evaluation of Al alloy composition after EOL recycling

The final Al alloy compositions after EOL recycling of GLARE can be obtained according to the total weight ratios of Hi lock to 2024 Al alloy, as listed in Table 3.12. The results show that there is a large amount Ti concentration increment in final recovered Al alloy compared to 2024 Al alloy in GLARE, and the Ti concentration in final Al alloy obviously

exceeds the nominal Ti concentration of 2024 Al alloy, max 0.05%. Ti concentration difference caused by Hi lock size is 0.185%. The V content of final Al alloy is consistent with the nominal concentration of 2024 Al alloy where the impurity element concentration in 2024 Al alloy is required to be lower than 0.05%.

Table 3.12. Initial 2024 Al alloy composition in GLARE and final Al alloy composition after EOL recycling (%).

Hi lock size	Al	Cu	Mg	Mn	Fe	Si	Ti	V	Others
5/32 inch	92.82	4.34	1.12	0.637	0.125	0.164	0.682	0.029	0.086
6/32 inch	92.64	4.33	1.12	0.636	0.125	0.163	0.867	0.027	0.086
2024 Al in GLARE	93.45	4.37	1.13	0.642	0.126	0.165	0.030	/	0.087

3.6.2 Experiments

In order to better understand the effect of Ti-6Al-4V fasteners on a refining behaviour of 2024 Al scrap during EOL recycling, the refining experiments of mixture consists of Ti-6Al-4V alloys and 2024 Al alloy sheets were conducted, and the weight ratios of Ti-6Al-4V to 2024 Al alloy is 0.73% and 0.94%, respectively. The size of 2024 Al alloy sheet is 35 mm×25 mm. Equimolar NaCl-KCl with additional 5% MgF_2 salt system is used as flux in refining, the weight ratio of salts to alloy mixture is 1:1, and the refining experiments are also executed at 800 °C for 2 hours under N_2 atmosphere.
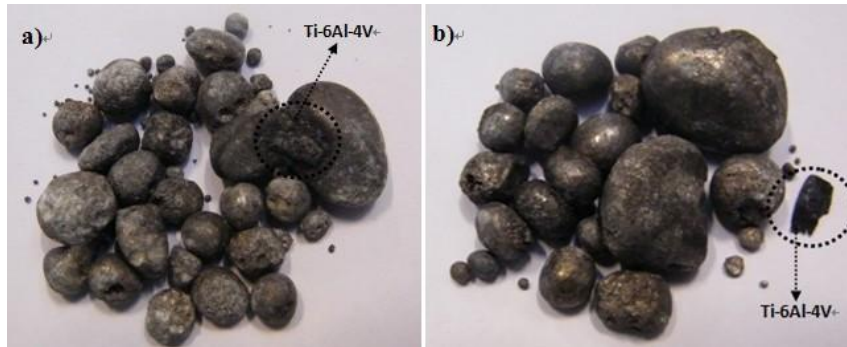
Figure 3.41. Recovered Al alloys after EOL recycling experiments. The employed D_{pin} of Hi lock for GLARE joining is a) 5/32 and b) 6/32 inch respectively.

The recovered Al alloys are shown in Figure 3.41. The Ti-6Al-4V alloy remains completely undissolved into 2024 Al after refining due to the high melting point of 1600-1660 °C, as we can see in Figure 3.41. As shown in Figure 3.41 b), the Ti alloy was completely separated from 2024 Al beads, indicating 2024 Al melt did not enwrap the Ti

alloy during solidification. Though Ti alloy and two 2024 Al beads are adhered in Figure 3.41 a), but Ti alloy did not dissolve either. The sizes of the two Al beads are bigger than others, so the Ti alloy with higher density of 4.5 g/cm^3 has settled down to the bottom of the crucible during refining because the larger size beads always form at the bottom of crucible.

Thus, the experiment results indicated that Ti-6Al-4V Hi locks will settle down to the bottom of liquid Al layer during refining and has a little influence on the composition of recovered 2024 Al alloy.

A single Ti-6Al-4V bulk alloy was employed in the refining experiments, in fact the Ti-6Al-4V alloy is not a unity but includes a lot of small size Hi locks in the real industrial scale situation, thus it is possible that small amount Ti alloys will dissolve into 2024 Al melt because of the small size during long time holding, which should be further studied.

3.7 Conclusion

After thermal delamination of GLARE, the well separated 2024 Al sheets were recycled by *Refining method with salt flux*. NaCl-KCl-Na$_3$AlF$_6$ and NaCl-KCl-MgF$_2$ were employed as fluxes during the 2024 Al refining.

* Effect of weight ratio of NaCl to KCl in NaCl-KCl-Na$_3$AlF$_6$ flux (35 mm×25 mm, 800 ^{o}C, NaCl-KCl-Na$_3$AlF$_6$, 2, N$_2$)

For NaCl-KCl-Na$_3$AlF$_6$ flux, the efficiency of two different ratios of NaCl to KCl, 70%NaCl-30%KCl and 44%NaCl-56%KCl, were investigated. 10% additional cryolite is preferred for both fluxes considering the recovered Al alloy quality together with the economic factor. But, the yield of big metal beads (> 2 mm) after Al alloy scrap (35×25 mm) recycling with 44%NaCl-56% KCl-10%Na$_3$AlF$_6$ is slightly increased compared to 70%NaCl-30%KCl-10%Na$_3$AlF$_6$ (97.3% vs. 96.8%). It was attributed to the lower melting point of equimolar NaCl-KCl system which has a positive influence on the metal coalescence due to the lower viscosity of molten flux. The concentrations of major alloying elements and impurity elements in recovered Al alloys are consistent with the nominal composition of 2024 alloy except for Mg. The Mg loss is caused by the reaction between Mg and cryolite.

* Effect of refining temperature (35 mm×25 mm, NaCl-KCl-Na$_3$AlF$_6$, 2, N$_2$)

The fluidity of flux and Al melt is decreased with the decreasing refining temperature, the decreased fluidity is deleterious to metal droplets aggregation, resulting in a lower metal yield. The yield of big metal bead after Al alloy scrap (10 mm×10 mm) refining with 44%NaCl-56%KCl-10%Na$_3$AlF$_6$ flux system is 96.1, 96.8 and 97.3% when the refining temperature is 720 ^{o}C, 760 ^{o}C and 800 ^{o}C, respectively. For 70%NaCl-30%KCl-10%Na$_3$AlF$_6$ flux system, the yield of big size bead is lower, 92.1% at 720 ^{o}C, 94.4% at 760 ^{o}C and 96.8% at 800 ^{o}C.

◆   Effect of the size of Al scrap (800 ^{o}C, 44%NaCl-56%KCl-10%Na$_3$AlF$_6$, 2, N$_2$)

The lower metal yield for the smaller size scrap recycling is mainly due to more oxides on the higher specific surface area and more contaminations which were caused during shredding and packaging. The experimental results indicated that the scrap size of bigger than 10 mm×10 mm should be preferred.

◆   Effect of weight ratio of salt to scrap (10 mm×10 mm, 800 ^{o}C, 44%NaCl-56%KCl-10%Na$_3$AlF$_6$, N$_2$)

The yield of big metal beads is obviously decreased with decreasing the amount of salt flux. For 44%NaCl-56%KCl-10%Na$_3$AlF$_6$ flux, the obtained yields of big metal beads after Al alloy scrap recycling is 97.1%, 94.8%, and 92.2% when the weight ratio of NaCl-KCl salt flux to Al scrap is 1.5, 1.0 and 0.5, and the yield of big metal beads is 97.0% when the weight ratio is 2. The yield of big metal beads is drastically decreased when the weight ratio of salt flux to Al scrap was lower than 1.5. The reduction of metal yield is attributed to the reduced fluidity of salt flux and decreased metal coalescence capacity.

◆   Refining with NaCl-KCl-MgF$_2$ flux (35 mm×25 mm, 800 ^{o}C, 44%NaCl-56%KCl-MgF$_2$, 2, N$_2$)

For 44%NaCl-56%KCl-MgF$_2$ flux, the big beads yield after Al alloy scrap (35 mm×25 mm) recycling is 97.8, 97.7, 97,2 and 96.8% when the additional MgF$_2$ in salt flux is 5, 10, 15 and 20%, respectively. Big metal beads yield is decreased with MgF$_2$ addition amount, especially when the amount is bigger than 10%. The yields of big beads with MgF$_2$ addition are higher than those with cryolite addition when the fluoride addition amount is lower, but the situation is reversed when the fluoride addition amount is increased to a higher level. Different with the influence of cryolite addition amount on metal aggregation behaviour, the increase of MgF$_2$ leads to the formation of more small size beads, indicating that the metal coalescence capacity reduced with the increasing amount of MgF$_2$ in salt flux. The possible reason for that is the viscosity of molten slats flux increased with MgF$_2$ addition amount while the high viscosity is unfavorable for the movement of aluminium droplets.

◆   Evaluation of EOL GLARE recycling

The effect of Ti-6Al-4V shear Hi lock in fuselage on the GLARE End-of-Life recycling was evaluated. The calculation result shows that the weight ratios of Ti alloy Hi lock to 2024 alloy in GLARE are 0.73% and 0.94% when Hi lock with D_{pin} of 5/32 and 6/32 inch is used, respectively, which after complete melting and mixing will lead to unsatisfied Ti concentration of 0.682% and 0.876% in final recovered 2024 Al alloy, respectively.. Fortunately the experimental results indicated that the Ti-6Al-4V Hi lock did not dissolve into Al melt but settles down to the bottom of crucible due to the higher melting point and bigger density of Ti-6Al-4V alloy compared to 2024 Al. Thus, the Ti concentration in the recovered Al alloy within the range of 2024 Al alloy nominal composition can be obtained after refining.

References

[1]   Totten GE, Mackenzie DS. Handbook of Aluminium: Volume 2-Alloy production and materials manufacturing. New York: Marcel Dekker publisher (2003).

[2]   http://www.crct.polymtl.ca/fact/phase_diagram.php?file=KCl-NaCl.jpg&dir=FTsalt

[3]   Ho FK, Sahai Y. Interfacial phenomena in molten aluminium and salt systems. In: International symposium recycling of metals and engineered materials, 2, Warrendale, 1990, Proceedings, TMS, (1990) 85.

[4]   Roy RR, Sahai Y. Interfacial tension between aluminium alloy and molten salt flux. Materials Transactions JIM 38 (1997) 546.

[5]   Martin-Grain L, Dinet A, Hicter JM. Liquid-liquid interfacial tension measurements applied to molten Al-halide systems. Journal of Materials Science 14 (1979) 2366.

[6]   Ho FK, Sahai Y. Interfacial tension in molten aluminium and salt system. Light Metals 1990, The Minerals, Metals & Materials Society (1990) 717.

[7]   Roy RR, Sahai Y. Interfacial tension in molten aluminium alloys and salt systems. Light Metals 1993, The Minerals, Metals & Materials Society (1992) 1067.

[8]   Roy RR, Sahai Y. Wetting behavior in aluminium-alumina-salt systems. Materials Transactions JIM 38 (1997) 571.

[9]   Peterson RD. Effect of salt flux additives on aluminium droplet coalescence. In: International symposium recycling of metals and engineered materials, 2, Warrendale, 1990, Proceedings, TMS, (1990) 69.

[10]   Tenório JAS, Carboni MC, Espinosa DCR. Recycling of aluminium: effect of fluoride additions on the salt viscosity and on the alumina dissolution. Journal of Light Metals 1 (2001) 195.

[11]   Roy RR, Ye J, Sahai Y. Viscosity and density of molten salts based on equimolar NaCl-KCl. Materials Transactions, JIM 38 (1997) 566.

[12]   Tenório JAS, Delgado F. Optimization of salt composition in the recycling of aluminium cans. In: Light Metals 1997, Orlando, FL, TMS (1997) 505.

[13]   Utigard TA, Friesen K, Roy RR, Lim J, Silny A, Dupuis C. The properties and uses of fluxes in molten aluminium processing. JOM 11 (1998) 38.

[14]   Ye J, Sahai Y. Role of molten salt flux in melting of used beverage container (UBC) scrap. In: International symposium recycling of metals and engineered materials, 3, Warrendale, 1995, Proceedings, TMS (1995) 639.

[15]   Hryn JN, et al. Products from salt cake residue-oxide. In: International symposium recycling of metals and engineered materials, 3, Warrendale, 1995, Proceedings, TMS (1995) 905.

[16]   Rossel H. VAW recycling research center-recycling techniques for postconsumer packaging. In: International symposium recycling of metals and engineered materials, 3, Warrendale, 1995, Proceedings, TMS (1995) 663.

[17]   Van Linden JHL, Stewart Jr. DL. Molten salt flux composition effects in aluminium scrap remelting. Light Metals (1988) 391.

[18] Johnston TJ, Peterson RD. The role of magnesium in fluxing UBC. In: International symposium on recycle and secondary recovery of metals and fall extractive and process metallurgy meeting, Fort Lauderdale, 1985, Proceedings, AIME (1985) 417.

[19] Xiao Y, Reuter MA. Recycling of distributed aluminium turning scrap. Minerals Engineering 15 (2002) 963.

[20] Schlesinger ME. Aluminium recycling. CRC Press, New York: Taylor & Francis Group, 2007.

[21] Smith MR. The present status of the Dereham process for magnesium removal in secondary aluminium smelting. Conservation and Recycling 6 (1983) 33.

[22] Xiao Y, Reuter MA, Boin U. Aluminium recycling and environmental issues of salt slag treatment. Journal of Environmental Science and Health 40 (2005) 1861.

[23] Reynolds RM, Olper M. Effect of salt flux additives on aluminiumd droplet coalescence. In: International symposium recycling of metals and engineered materials, 2, Warrendale, 1990, Proceedings, TMS, 1990;69.

[24] Narayanan R, Sahai Y. Chemical interactions of dross with water and water vapor in aluminium scrap remelting. Materials Transactions 38 (1997) 85.

[25] Xie G, Ohashi O, Yamaguchi N, Song M, Mitsuishi K, Furuya K, Noda T. Behavior of oxide film at interface between particles of Al-Mg alloy powder compacts prepared by pulse electric current sintering. Jpn. J. Appl. Phys. 42 (2003) 4725.

[26] Scherm F, Völkl R, Van Smaalen S, Plamondon P, L'espérance G, Bechmann F, Glatzel U. Microstructural characterization of interpenetrating light weight metal matrix composites. Mater. Sci. Eng. A 518 (2009) 118.

[27] Masson DB, Taghiei MM. Interfacial reactions between aluminium alloys and salt flux during melting. Materials Transactions 30 (1989) 411.

[28] Ojovan MI, Travis KP, Hand RJ. Thermodynamic parameters of bonds in glassy materials from viscosity-temperature relationships. Journal of Physics: Condensed Matter 19 (2007) 415107.

[29] http://www.alcoa.com/fastening_systems/aerospace/en/product.asp?cat_id=216&prod_id=1135

[30] http://www.hi-shear.com/brochures/Hilok_Hitigue_Installation.PDF

[31] http:// www.fokker.com/Innovations-GLARE

[32] Müller RPG. An experimental and analytical investigation on the fatigue behavior of fuselage riveted lap joints. PhD thesis, Delft University of Technology (1995).

[33] Rans CD, Alderliesten RC, Straznicky PV. Assessing the effects of riveting induced residual stresses on fatigue crack behaviour in lap joints by means of fractography. International Journal of Fatigue. 31 (2009) 300.

[34] http://www.lisi-aerospace.us/fastener_hl_stds.htm

[35] Vlot A, Gunnink JW. Fibre Metal Laminates: An Introduction. Dordrecht: Kluwer Academic Publishers (2001).

Chapter 4 Si removal from Al melt

It is well-known that silicon is one of the main impurities that should be strictly controlled in the high strength Al-Cu-Mg (2xxx) and Al-Zn-Mg-Cu (7xxx) alloys. At present, commercial pure aluminium has to be added into secondary aluminium to ensure that the impurity silicon and iron content are within limits. With the fast growth of secondary aluminium industry, a direct method for removal of impurity silicon from aluminium melt is highly demanded. However, unfortunately, up to now, no practical solution has been found for the removal of impurity silicon from Al alloy in industry.

In this chapter, an attempt for impurity Si removal based upon compound formation was made. Ti was selected as the most promising potential alloying element to form Si-rich phases with high melting point in Al melt, whereupon the Si-rich compound with high melting point can be removed from the Al melt by filtration or sedimentation. $(Al,Si)_3Ti$ is the only stable compound at the refining temperature that is useful for Si removal. The effects of holding time, initial impurity Si concentration, holding temperature and amount of Ti addition on the Si purification efficiency were investigated and discussed. The results indicate that the Si purification efficiency is lower than 20% due to the low Si concentration in $(Al,Si)_3Ti$ phase.

The maximum Si solubility and the Si diffusivity in Al_3Ti which are significant to evaluate the potential of Ti addition for impurity Si removal from Al alloy (Si < 0.5 wt%), are still unknown. The Si diffusivity is related to the diffusion constant D_0, the formation energy of vacancy and the migration energy of Si in Al_3Ti. It is obvious that site preference of doped atom and the point defect formation have a significant impact on doping behaviour especially for the diffusion behaviour of doped atom. In this chapter, the intrinsic physical mechanism of Si substitution in Al_3Ti was studied by using first-principles calculations to evaluate the potential of Ti addition for impurity Si removal from Al, where Si site preference solubility in Al_3Ti, point defects formation energies, and the migration mechanism of vacancy in clean and Si-doped Al_3Ti were investigated in detail.

4.1 Introduction

Silicon is a very important alloying element in aluminium alloys, which improves the fluidity, tensile strength and corrosion resistance of Al-Si casting alloys and forms disperse precipitate particles to enhance the strength and toughness of Al-Si-Mg wrought alloys [1-2]. However, for high strength Al-Cu-Mg (2xxx) and Al-Zn-Mg-Cu (7xxx) alloys, silicon together with Al and other impurity elements such as iron, forms a Si-rich phase that is brittle and has a Young's modulus and expansion coefficient different from the α-Al matrix. The brittle phases act as stress raisers and points of weak coherence, leading to a reduction in the mechanical properties, especially for fracture toughness [3-4]. Therefore, silicon is one of the main impurities that should be strictly controlled in such alloys. At present, commercial pure aluminium has to be added to secondary aluminium to ensure that the impurity silicon and iron content remains within the limit. With the fast growth of the secondary aluminium industry, a direct method for removal of impurity silicon from aluminium melt is highly demanded.

Impurity silicon removal from Al was investigated by several methods, including directional solidification, alloying method and external field method. But none of these methods is used successfully for removal of impurity silicon from Al alloy in industry.

The directional solidification method is usually applied for the purification of high purity aluminium, but with low efficiency and high costs. This purification method is also not suitable for wrought alloys because of a few other alloying elements.

An alloying method which adds alloying elements to form Si-rich compounds in liquid metal was studied [5]. However, the chemical similarity of Al and Si, together with the much lower activity of Si compared to Al lead to difficulties in the removal of Si at low concentration (<1 wt%). Calcium was chosen to form intermetallic compounds containing silicon, Ca_2Si and $CaSi_2Al_2$, which can be separated from an Al melt by filtration [5]. Although this method is effective for Al alloys with high Si concentration, at low Si concentration ($<$1 wt%) Al alloys need vast calcium additives to form Ca_2Si and $CaSi_2Al_2$, which is not considered economically feasible [3].

Application of an external electromagnetic field in laboratory-scale was also employed to study the efficiency of Si removal from Al alloy. The separation of Si and Cu from an Al-1 wt% Si-1 wt% Cu melt was also investigated by using an electromagnetic centrifugal solidification method. The results indicated that the distribution of Si is irregular after the introduction of electromagnetic and centrifugal forces [6] due to the similarities of density and physical properties between Al and Si.

4.1.1 Selection of alloying elements for Si purification experiments

In this research, all chemical elements of the periodic table were evaluated to select feasible elements which can react with low concentration Si in Al melts and form binary or ternary phases with a high melting point which can be easily removed to decrease impurity Si concentration. Herein, only ternary Al-Si-X (X is the candidate element) phase diagrams were considered, due to complexity and data shortage for quaternary and multi-

elements phase diagrams. After thorough evaluation of the potential candidate elements, purification experiments were conducted by using the selected elements to investigate the Si removal efficiency.

The Al corner phase compositions of Al-Si-X ternary phase diagrams were evaluated to find out the suitable alloying element X which can form a Si-rich phase in an Al alloy melt and then impurity Si (<1 wt%) can be removed by removing those Si-rich phases. Most of regular elements were evaluated, and the conclusion is listed in Table 4.1. There are several criteria to determine the feasible alloying elements, the criteria are as follows:

◆ To facilitate removal of impurity Si from Al melt, the alloying element should react with Si (or Si together with Al) in Al melt to form Si-rich compounds with higher melting point than Al or Al alloys

◆ The alloying element should be cheap and abundant for economic reason

◆ The residual alloying element should be little harmful to the properties of Al or Al alloy

At first, noble gasses (He, Ne, Ar, Kr, Xe, Rn) are not considered because of their extreme stability. Radioactive elements (Po, At, Fr, Ra, Ac, Th, Pa, U) were excluded due to the potential risk. Moreover, Halogen elements (F, Cl, Br, I) were excluded considering that no Si-rich phase is formed when Cl_2 is used as refining gas. the synthetic elements (Tc, Pm, Np, Pu, Am, Cm, Bk, Cf, Es, Fm, Md, No, Lr, Rf, Db, Sg, Bh, Hs, Mt, Ds, Rg, Cn, Uut, Fl, Uup, Lv, Uus, Uuo) were also excluded.

After evaluation of Al-Si-X phase diagrams, the excluded elements which do not meet the criteria mentioned before are classified and listed as follows:

◆ No Si-rich phase formation at temperature higher than the melting point of Al or Al alloy

(1) Not any binary or ternary phase is formed
Be [3-7], Bi [3], Cd [3], Ga [3], Ge [3], H [3], In [3], Sn [3], Zn [8]

(2) No Si-rich phase is formed
B [9-10], C, N [11-12], P [13], S [3], V [14], Co [15], Ni [16], Cu [17-18], Se [3], Zr [3], Sb [19].

(3) Si-rich phases are formed at lower temperature than the melting point of Al alloy
Li [20], Na [3], K, Mg [21-22], Ca [23], Cr [24-25], Mn [26-27], Sr [28], Y [29], Ba [30], Ce [31], La [3]

◆ Rare or expensive elements

Rh, Ru, Pt, Au, Re, Pd, Ir, Os, Ag, Hf, Ta, Te, Sc, Tl, Ho, Er, Tm, Yb, Lu, Rb, Cs, and partly rare earth elements (Dy, Eu, Gd, Nd, Sm, Pr, Tb)

◆ Input of new unfavourable impurity element

O, Fe [32-36], Nb, Mo, W, As, Hg, Pb

Table 4.1. The classification of elements in the periodic table.

H																	He
Li	Be											B	C	N	O	F	Ne
Na	Mg													P	S	Cl	Ar
K	Ca	Sc	Ti	V	Cr	Mn	Fe	Co	Ni	Cu	Zn	Ga	Ge	As	Se	Br	Kr
Rb	Sr	Y	Zr	Nb	Mo	Tc	Ru	Rh	Pd	Ag	Cd	In	Sn	Sb	Te	I	Xe
Cs	Ba	*	Hf	Ta	W	Re	Os	Ir	Pt	Au	Hg	Tl	Pb	Bi	Po	At	Rn
Fr	Ra	**	Rf	Db	Sg	Bh	Hs	Mt	Ds	Rg	Cn	Uut	Fl	Uup	Lv	Uus	Uuo

*	La	Ce	Pr	Nd	Pm	Sm	Eu	Gd	Tb	Dy	Ho	Er	Tm	Yb	Lu
**	Ac	Th	Pa	U	Np	Pu	Am	Cm	Bk	Cf	Es	Fm	Md	No	Lr

★ *Not considered*

★ *No Si-rich phase formation at temperature higher than the melting point of Al or Al alloy*

★ *Rare or expensive elements*

★ *Input of new unfavourable impurity element*

★ *Possible candidate*

The Al-Ti-Si system was studied by Raman and Schubert [37], and the isothermal section reported at 700 ^{o}C indicated that two ternary phases around the compositions $\tau_1(Ti_7Al_5Si_{14})$ and $\tau_2(Ti_3Al_2Si_5)$ exist. A third ternary phase mentioned by Raman and Schubert [37] is probably inside the homogeneity range of τ_1. For the binary Al_3Ti phase a solubility up to 15 at.% Si on the Al-sublattice is stated. After that, a partial liquidus surface near the Al-Si binary eutectic was determined by Zakharov et al. [38], and the literature about Al-Si-Ti system was reviewed by Perrot [39].

Based on previous work [37-39], the Al-Si-Ti phase diagram was calculated by Gröbner [10]. The calculated results indicated that Ti can react with Al and Si to form Al_3Ti and TiSi compounds in the Al melt with 1 wt% Si, as shown in Figure 4.1. But, the TiSi phase is not formed when the Si concentration is decreased to 0.5 wt%, and the Si-rich phase $\tau_1(Ti_7Al_5Si_{14})$ is formed at a temperature lower than the Al melting point, as shown in Figure 4.2. That Si can substitute Al in Al_3Ti also has been verified by Zeren and Karakulak [40], 0.1~10 wt% Ti was added into near-eutectic Al-Si alloy, the main Si-rich phases are eutectic Si and $(Al,Si)_3Ti$, but no TiSi phase has been found in the alloys.

According to research mentioned above, Ti is a promising alloying element to remove low concentration impurity Si (<1 wt%) from an Al melt. Ti can react with Si to form the high melting point compound TiSi when Si concentration in Al is around 1 wt%, and Si can dissolve into Al_3Ti to form the high melting point compound $(Al,Si)_3Ti$ if TiSi phase can not be formed when the Si concentration is lower than 1 wt%. Moreover, Ti solubility in an Al melt at 720 ^{o}C is about 0.26 wt% while residual Ti is hardly harmful to the properties of Al alloy.
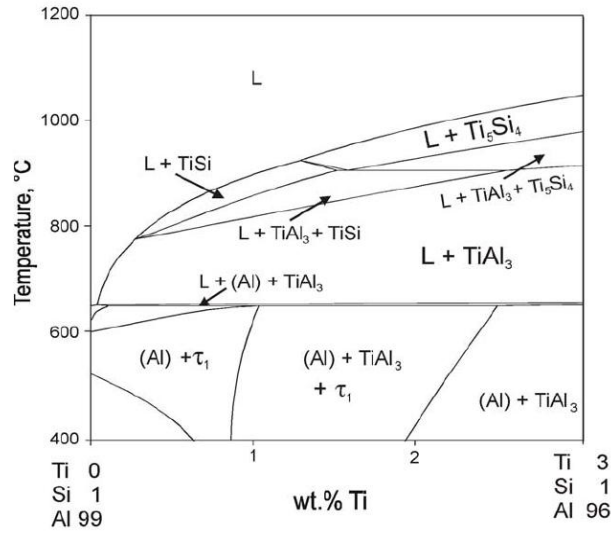
Figure 4.1. Vertical section for Al-Ti-Si system at 1 wt% Si [10].
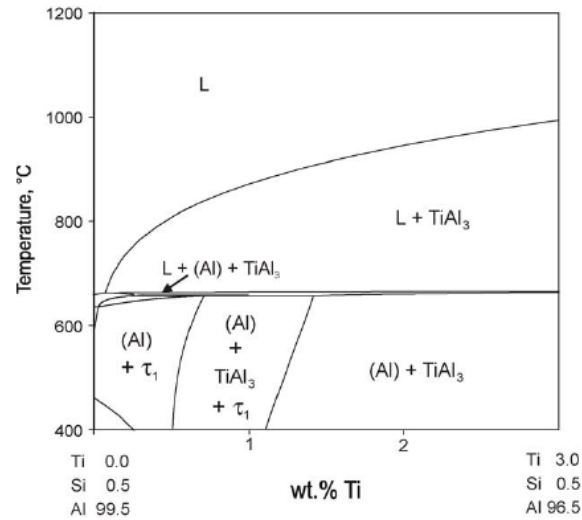
Figure 4.2. Calculated Al-rich part of vertical section in the Al-Si-Ti system at constant 0.5 wt% Si [10].

Therefore, in the first part of this chapter, the experiments for Si removal were performed by the addition of Ti in Al-Si melt to investigate the Si removal efficiency. The initial Si content in Al melt is lower than 1 wt% for all experiments. The effects of holding time, initial impurity Si concentration, holding temperature and Ti addition amount on the Si purification efficiency were investigated and discussed.

4.1.2 Si substitution behaviour in Al$_3$Ti - First-principles study

The calculated Al-rich part of vertical section of Al-Si-Ti phase diagram (Si content is 0.5 wt% and Ti content is lower than 3 wt%) [10] combined with previous experimental results [37, 40] indicated that the most probable Si-containing phase is (Al,Si)$_3$Ti at temperatures higher than the melting point of Al-Si alloy when the Si content is lower than 0.5 wt%.

The Si diffusivity in Al$_3$Ti which is significant to evaluate the potential of Ti addition for impurity Si removal from Al alloy (Si < 0.5 wt%) is still unknown. It is obvious that site preference of doped atom (in this case Si) and the point defect formation have a significant impact on doping behaviour especially for the diffusion behaviour of doped atom. In this research, the intrinsic physical mechanism of Si substitution in Al$_3$Ti was studied by using first-principles calculations to evaluate the potential of Ti addition for impurity Si removal from Al, where Si site preference and point defects formation energies in Al$_3$Ti, and the migration mechanism of a vacancy in clean and Si-doped Al$_3$Ti were investigated in detail.

First-principles calculations were used to understand and predict properties of materials and structural stability. Over the years, researchers had investigated the substitution behaviour of alloying additions theoretically based on first-principles calculations. The site preference of W in B2-TiAl and L1$_0$-TiAl were studied by Lu et al. [41]. The electronic structure and total energies were calculated using the full-potential linearized augmented plane-wave method [42], the result indicated that W was predicted to occupy Al sites in the B2 TiAl, but Ti sites were preferred in the L1$_0$ TiAl. An Al atom in L1$_0$ TiAl has eight Ti and four Al nearest-neighbours, where as a Ti atom has eight Al and four Ti nearest neighbors. Since there is a strong bonding between W and Ti, it is expected intuitively that W should occupy the Al site in L1$_0$ TiAl so as to maximize the Ti-W bonding effect. However, the calculated heats of formation reveal that W prefers to occupy Ti sites. From the electron density maps, it is found that this can be attributed to the difference between the in-plane and the inter-plane W-Ti bonding. The site preference of Zr in Ti$_3$Al was also investigated by Ravi et al. [43], the values of equilibrium lattice parameters and heat of formation were calculated to determine the site preference of Zr, which were calculated by using the tight-binding linear muffin-tin orbital method [44]. The results indicated that Zr atoms prefer to occupy the Ti sites. Sluiter et al. [45-46] have studied the site preference of ternary additions in Ni$_3$Al. A simple site preference parameter S was introduced and results for a large numbers of ternary additions were discussed, Ti and Sc were found to substitute preferentially for Al [15], whereas Fe has no site preference and Co was found to have a weak preference for the Ni sites [16]. The first-principles method does not rely on any experimental data and therefore is truly predictive.

Point defects formation in binary and ternary systems has been intensively studied by using first-principles calculations. The spin polarized density functional theory has been used to study the formation energies and the structural properties of vacancies and Al substitutional defects in δ-TiN [47]. The formation of vacancies and aluminium substitutional impurities in δ-TiN under two different conditions, N-rich and Ti-rich, are separately discussed because the Gibbs free energy of Ti or N atom in the reservoir is distinct under different compositions. The formation energy results indicated that among the studied point defects the V$_N$ (N vacancy) with the formation energy of -0.47 eV is the only probable one at Ti-

rich compositions, while both V_{Ti} (Ti vacancy) and Al_{Ti} (Al occupies Ti site) defects are seen to be likely at N-rich compositions, the formation energy is 0.20 and 1.87 eV for V_N and Al_{Ti}, respectively. The energetic and electronic structure of vacancies, anti-sites, and atomic X (B, C, and N) defects in FeAl alloys was also investigated by first-principles study to understand the effect of stability of these structure defects on bonding [48].

$D0_{22}$-Al_3Ti has a similar site distribution with $L1_2$-Ni_3Al, and both $D0_{22}$ and $L1_2$ structures are A_3B-type ordered structures based on the fcc lattice. The diffusion behaviours of vacancies and alloying elements in $L1_2$-Ni_3Al have been extensively investigated by using molecular dynamics simulations with empirical interatomic potentials and first-principles calculation where the first nearest-neighbour diffusion mechanism, second nearest-neighbour diffusion mechanism and sublattice diffusion mechanism have been discussed [49-52]. Moreover, other diffusion mechanisms have also been considered in the literature. Höglund et al. [53] indicated that Zn in p-type GaP and InP diffuses by a substitutional-interstitial mechanism containing the dissociative mechanism and the kick-out mechanism. The six-jump cycle [54] and the triple defect mechanism [55-56] were also discussed in addition to vacancy migration mechanisms of intermetallic compounds. It is well known that point defects have a significant impact on doping behaviour especially for the diffusion behaviour, and have been studied extensively in other doping systems. Point defects play an important role in diffusion mechanism of doped atoms and atomic self diffusion in intermetallics [49, 57]. Only few theoretical data have been reported on the point defects formation in Al_3Ti. Thus a systematic theoretical investigation of point defect formation, Si site preference and Si diffusion mechanism in Al_3Ti is conducted in this research, which will be useful to obtain more fundamental insights into the substitution and diffusion behaviour of Si in Al_3Ti, and understand the potential of Ti addition for Si removal in Al melt. Therefore, in the second part of this chapter, Si site preference, the formation energies of point defects, and the migration mechanisms of doped Si and point defects in $D0_{22}$-Al_3Ti have been investigated by first-principles calculations. The first nearest-neighbour diffusion mechanism, the second nearest-neighbour diffusion mechanism and the sublattice diffusion mechanism were considered to evaluate the migration paths and energy barriers for vacancies, and a plausible two-defect migration mechanism for Ti vacancy in Al_3Ti was proposed. Moreover, the effects of Si doping on the vacancy formation and migration were discussed, and the migration of doped Si atom in Al_3Ti was also investigated.

4.2 Si purification experiment

4.2.1 Materials

Commercial pure aluminium was melt together with pure Si particles to prepare Al-Si alloys. The composition of commercial pure aluminium and the prepared Al alloys for the present study is given in Table 4.2. Ti can be introduced into Al melt in the form of pure Ti particles, Al-Ti master alloys or Ti salts. K_2TiF_6 powders are chosen in this study considering the economic cost. K_2TiF_6 has been used together with KBF_4 to provide the source of Ti for the formation of Al_3Ti and TiB_2 particles to refine Al grain [58-59]. The reaction between K_2TiF_6 and Al is as follows [60]:

$$13Al + 3K_2TiF_6 \rightarrow 3Al_3Ti + 3KAlF_4 + K_3AlF_6 \qquad (4\text{-}1)$$

K_2TiF_6 is usually added into Al melt at 800 $^{\circ}$C. Ti solubility in Al melt is about 0.45 wt% at 800 $^{\circ}$C according to the Al-Ti binary phase diagram and the vertical section of Al-Ti-Si phase diagrams (Figure 4.1 and 4.2). Thus, all Al_3Ti generated by the reaction between Al and K_2TiF_6 dissolves into Al melt if the Ti addition is lower than 0.45 wt%, but the excess Al_3Ti forms in the Al melt when the Ti addition is larger than 0.45 wt%. The dissolved Ti provides the source of Ti for the formation of TiSi phase if TiSi compounds can be formed following the calculated phase diagram presented in Figure 4.1.

Table 4.2. Initial compositions (wt%) of the commercial pure Al and the prepared Al alloys used in this study, and the rest is Al.

Impurity elements	Si	Fe	B	Ca	Na	Cu
Commercial pure Al	0.08	0.14	0.0136	0.0122	0.0076	0.0060
Alloy 1	0.14	0.14	0.0132	0.0125	0.0080	0.0051
Alloy 2	0.20	0.14	0.0135	0.0122	0.0078	0.0064
Alloy 3	0.38	0.13	0.0136	0.0132	0.0081	0.0062
Alloy 4	0.77	0.14	0.0135	0.0126	0.0074	0.0054
Alloy 5	1.04	0.13	0.0134	0.0124	0.0075	0.0061

4.2.2 Experimental procedure

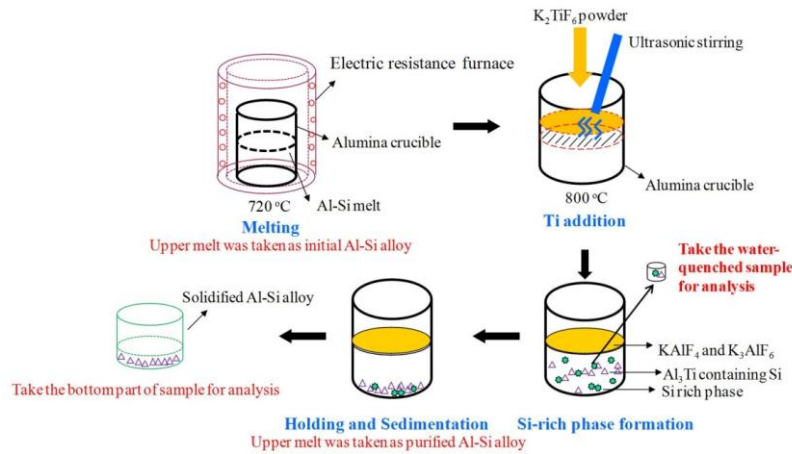*Figure 4.3. Schematic diagram of the procedure of Si purification experiment*

The schematic diagram of experimental procedure is shown in Figure 4.3. Nearly 400 g clean and dried aluminium was melted in an electric resistance furnace (Carbolite company) using an alumina crucible with size of Φ80×80 mm. The crucible was heated up to a pre-set temperature of 800 $^{\circ}$C after the aluminium completely melted. K_2TiF_6 powders

were added to the melt at this temperature with ultrasonic stirring for 1 min to accelerate Ti absorption. Then the melt was held at 800 $^{\circ}$C for half hour to facilitate the reaction between K_2TiF_6 and Al, and the transfer efficiency of Ti from K_2TiF_6 to molten Al was higher than 95% in this work. Then, some Al melt was quickly taken after mechanical stirring for SEM analysis, to identify if Si-rich phase has been formed. After that, the melt temperature was decreased to a pre-set value and the holding time is 60 min. At last, the surface slag ($KAlF_4$ and K_3AlF_6) was skimmed away, and the upper melt was taken as a purified sample with a 20 ml alumina crucible for composition analysis. The bottom sample of the solidified aluminium in the crucible was taken for metallographic observations and microscopic analysis.

The metallographic specimens were polished mechanically and then etched with 0.5% HF reagent. The microstructure was observed by using Scanning Electron Microscopy (JEOL JSM 6460 SEM), and constitution of phases were analyzed using an Energy Dispersive Spectroscopy (EDS) attached to the SEM equipment. Phases of the bottom sample were detected with an X-ray diffractometer (BRUKER D8 DISCOVER X-Ray Diffractometer). The chemical compositions of the purified aluminium samples were detected by Inductively Coupled Plasma Atomic Emission Spectrometry (ICP-AES).

4.2.3 Results and discussion

To identify the possible Si-rich phases which are formed in Al-Si after the addition of Ti, a purification experiment was conducted according to the calculated phase diagram Figure 4.1. The initial Si concentration in Al melt is 1.04 wt% (Alloy 5), and the addition of Ti is 1 wt% (equivalent to 5 wt% K_2TiF_6). The experiment is carried out at 800 $^{\circ}$C with a total holding time of 2 hours.

To avoid the phase transition of Si-rich phase during solidification of Al melt, the water-quenched sample was taken from Al melt after Ti addition, to identify if Si-rich phase has been formed. The SEM photo of water-quenched sample is shown in Figure 4.4. A few particulates were found in the water-quenched sample.
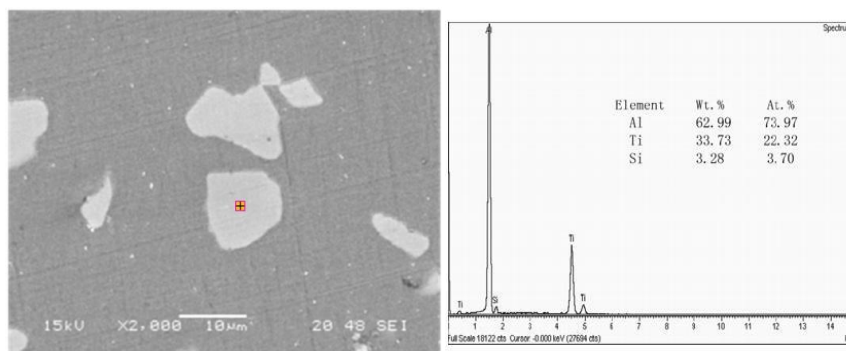

Figure 4.4. SEM pattern of water-quenched sample of Al-1.04wt% Si alloy after Ti addition. The composition of the particulate was analyzed by using EDS and the measure was made in the red boxed area.

The composition of the particulate was analyzed, and the main chemical elements in the particulate is Al, Ti and small amount of Si (3.70 at.%). The atomic concentration ratio of Al and Ti is close to 3. The formation of $(Al_{1-x},Si_x)_3Ti$ was certified when a small amount of Ti was added in Al-Si alloy to form Al_3Ti which was used as grain refiner in Al-Si alloy [60] or used as reinforced particulates in Al alloy metal-matrix composite [61]. Thus, the particulate should be $(Al_{1-x},Si_x)_3Ti$. But, neither TiSi phase nor another Si-rich phase was found in Al melt after Ti addition according to the SEM and XRD analysis.

The morphology of the bottom sample was also analyzed and the SEM photo is shown in Figure 4.5. We can see that many fine particulates gathered in the bottom of the aluminium melt and the height of the sedimentation layer is close to 4 mm while the total height of Al in Φ80 mm×80 mm crucible is about 40 mm, which indicates that particulates were precipitated from the aluminium melt and settled down to the bottom during the holding time.
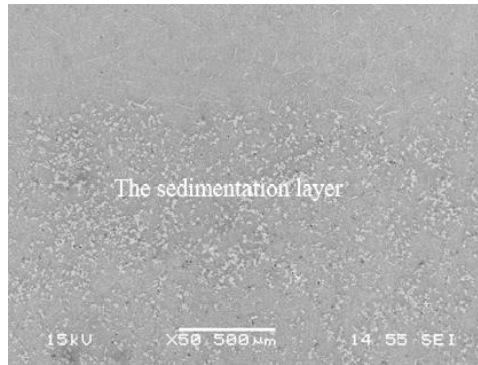

Figure 4.5. The metallographic picture of bottom sample after purification (etched by 0.5% HF).

The particulates uniformly disperse in the bottom Al matrix and exhibit a predominantly blocky morphology and the sizes of the particulates are between 10-30 μ m, as we can see in Figure 4.6.
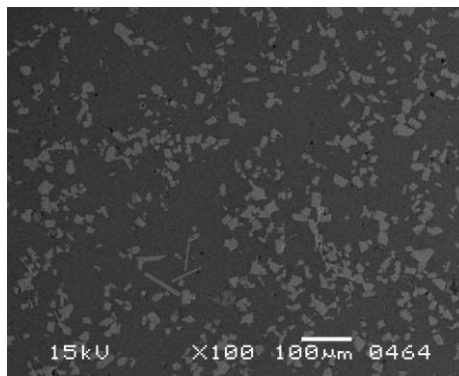
Figure 4.6. SEM pattern of bottom sample of Al-1.04wt% Si alloy after purification.

Figure 4.7 is the XRD pattern of the bottom aluminium sample. The main phases are α-Al and Al_3Ti, but TiSi phase presented in the Al-Si-Ti ternary diagram (Figure 4.1) was not found. It is noted that there exists a small deviation of diffraction angle θ between the particulates and referenced Al_3Ti phase during phase identification. This deviation is caused by the doping of Si in Al_3Ti which changed the lattice constant of Al_3Ti.
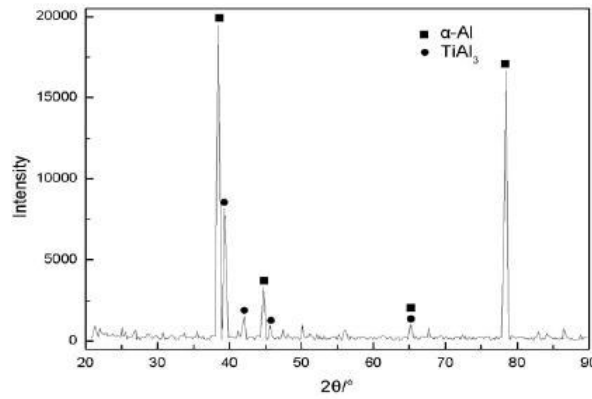
Figure 4.7. XRD pattern of bottom sample in Al-1.04 wt% Si alloy after purification.

However, the phase compositions of the particulates in bottom sample were detected with EDS, as shown in Figure 4.8. The particulate in bottom sample is also $(Al_{1-x},Si_x)_3Ti$. The sedimentation of the $(Al_{1-x},Si_x)_3Ti$ particulates then takes place due to its higher density than Al melt. Neither TiSi phase nor any other Si-rich phase was found in the bottom of the sample which is consistent with the result of water-quenched sample.
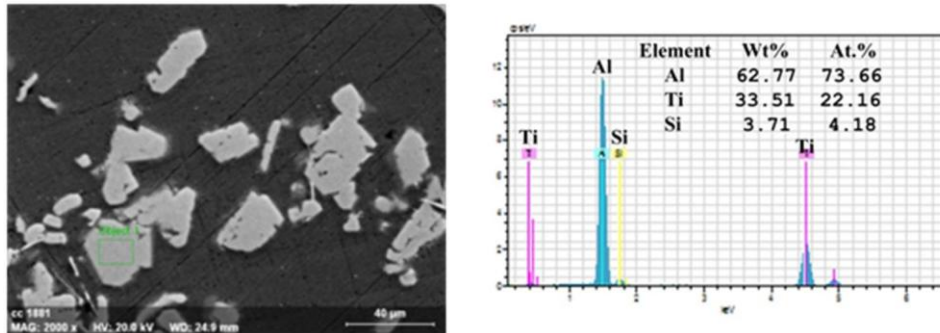
Figure 4.8. EDS analysis of the particulates in bottom sample of Al-1.04 wt% Si alloy after purification. The measure was made in the green boxed area.

The Si concentration in Al melt is decreased from 1.04 wt% to 0.82 wt% after purification, and the residual Ti in purified Al melt is 0.45 wt%. In summary, the reduction of Si concentration in Al is completely attributed to the Si substitution behaviour in Al_3Ti. No

TiSi or other Si-rich phases are found after the addition of Ti at 800 $^{\circ}$C. Therefore, the Si substitution behaviour in Al$_3$Ti is the key point for Si removal from Al melt, and Si concentration in Al$_3$Ti is the essential factor for Si purification efficiency. During Si purification, Si concentration in Al$_3$Ti is closely related to the initial Si concentration in Al melt, and the chemical potential of Si in Al$_3$Ti should be equivalent to the chemical potential of Si in Al melt at the equilibrium state of system. Moreover, the Ti addition, holding temperature and holding time also have important influences on the Si concentration in Al$_3$Ti.

The Si purification efficiency under various conditions is discussed in the following sections. Considering that Ti solubility in Al melt is decreased with temperature and no TiSi is formed at 800 $^{\circ}$C, most of purification experiments are conducted at 720 $^{\circ}$C to decrease the residual Ti in Al melt. The residual Ti (Ti solubility in Al melt) at 720 $^{\circ}$C is about 0.26 wt% according to Al-Ti phase diagram which is lower than the residual Ti of 0.45 wt% at 800 $^{\circ}$C.

4.2.3.1 Influence of holding time

Figure 4.9 shows the variation of Si concentration of purified aluminium samples taken from the upper part of the melt with different holding time at 720 $^{\circ}$C and Ti addition in Al-Si alloys are 1 wt% for all tests. The Si concentrations were stable when the holding time exceeded 60 min for both Al melt with initial Si concentration of 0.14 wt% and 1.04 wt%. This indicates that 60 min is enough to complete the whole Si dissolution process in Al$_3$Ti particulates. The required dissolution time of Si was shorter when the original Si content in Al melt is 0.14 wt% compared to that for the melt with initial Si concentration of 1.04 wt%. This phenomenon should be attributed to the higher Si concentration in Al$_3$Ti when the initial Si concentration in Al melt is 1.04 wt%, and the diffusion behaviour of Si in Al$_3$Ti requires longer time.
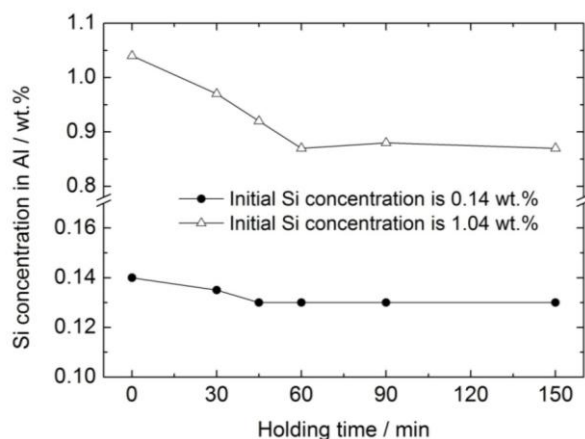

Figure 4.9. The relationship between the initial Si concentration and the holding time during Si purification at 720 $^{\circ}$C.

4.2.3.2 Influence of initial Si concentration

The comparison of Si concentration in the upper part of the melt before and after purification with 5 wt% K_2TiF_6 (1 wt% Ti) at 720 ^{o}C for 60 min is shown in Figure 4.10 (a). The decrease of Si content in Al melt is attributed to the formation and sedimentation of Si-rich phase $(Al_{1-x},Si_x)_3Ti$. The Si concentration decrease is only 0.01 wt% and 0.02 wt%, respectively, when the initial Si concentration is 0.14 wt% and 0.20 wt%. However, the purification efficiency is better with higher initial Si content, e.g., the content of Si reduced from 0.77 wt% to 0.67 wt% and from 1.04 wt% to 0.87 wt%, respectively. The Si purification efficiency is 7.1%, 10.0%, 10.5%, 11.8% and 13.5% when the initial Si concentration is 0.14 wt%, 0.20 wt%, 0.38 wt%, 0.77 wt% and 1.04 wt%, respectively, as shown in Figure 4.10 (b). According to the reaction equation (4-1), the Al loss caused by the reaction between Al and K_2TiF_6 is only 2.44 wt% when 5 wt% K_2TiF_6 was added, thus the effect of Al loss on the Si concentration after purification is negligible.
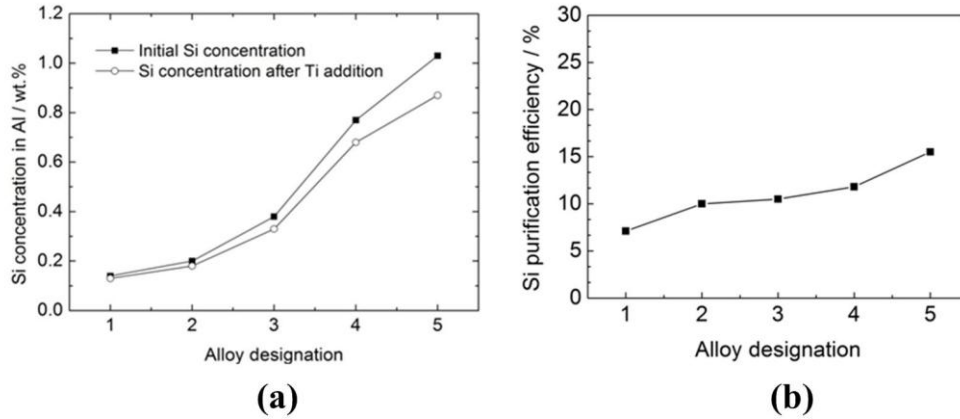
Figure 4.10. (a) Si concentration variation and (b) the Si removal efficiency after the purification of Al melt containing different initial Si concentration at 720 ^{o}C, and the Ti addition is 1 wt%.

The measured Si content in the $(Al,Si)_3Ti$ phase of different alloys based on EDS analysis is shown in Table 4.3. The Si concentration in Al_3Ti increases with the initial Si content in the Al melt, indicating that the driving force of the Si substitution enhances with increased Si concentration.

According to the decrease of Si content in Al melt, the real atomic percent of the Si concentration in the Al_3Ti can be calculated. Considering the solubility of Ti in the Al melt at 720 ^{o}C, the amount of Ti which can be used to form Al_3Ti was less than 1 wt%.

The solubility of Ti in the Al melt could be calculated by [62].

$$\log_{10}[Ti]_{pct} = \frac{-3996}{T} + 3.435 \qquad (4-2)$$

where $[Ti]_{pct}/100$ is the weight percent of Ti solubility in the Al melt and T is the absolute temperature of the melt. Thus, the solubility of Ti in the Al melt is 0.257 wt% at 720 ^{o}C,

which should be excluded from the effective Ti concentration which can form Al$_3$Ti phase. As a result, the weight percent of Al$_3$Ti formed in the melt can be obtained as:

$$[Al_3Ti]_{wt} = ([Ti]_{wt}^{total} - 0.257) \times \frac{M_{Al_3Ti}}{M_{Ti}}$$
(4-3)

The real atomic percent of the Si concentration in Al$_3$Ti can be calculated as:

$$[Si]_{at} = \frac{[\Delta Si]_{wt} / M_{Si}}{4 \times [Al_3Ti]_{wt} / M_{Al_3Ti}} \times 100\%$$
(4-4)

where *[Al$_3$Ti]$_{wt}$* is the weight percent of Al$_3$Ti formed in the Al melt, Ti_{wt}^{total} is the total weight percent of Ti concentration in the Al melt, M_{Al_3Ti}, M_{Ti} and M_{Si} is the molar mass of Al$_3$Ti, Ti and Si respectively, *Si$_{at}$* is atomic percent of the Si concentration in Al$_3$Ti, $[\Delta Si]_{wt}$ is the measured reduction of weight percent of Si concentration in the Al melt.

According to the variation of Si concentration and the Ti addition, the converted real Si concentration in Al$_3$Ti to is also shown in Table 4.3. By comparison, it is higher than the measured one, especially for Al$_3$Ti particles which are formed in Al melt with high initial Si concentration. The discrepancy may be caused by poor accuracy of EDS test. The calculated result shows that the Si concentration in Al$_3$Ti is enhanced to 9.12 at.% when initial Si concentration is 1.04 wt%, this value is close to Raman and Schubert's result of 15 at.% [37].

Table 4.3. Si concentration in Al$_3$Ti phase.

Initial Si Concentration / wt%	0.14	0.20	0.38	0.77	1.04
Measured by EDS / at.%	0.62	0.88	2.69	3.70	4.50
Converted / at.%	0.57	1.14	2.87	5.13	9.12

The mass changes of Si, Al, Ti and Fe after purification were calculated, as shown in Figure 4.11. The total mass decrease is mainly attributed to the consumption of Al. A few Al was reacted with K$_2$TiF$_6$ to form Al$_3$Ti particulates, which will be removed from Al melt. The mass decrease is 5.09 g, 5.05 g, 4.97 g, 4.71 g and 4.42 g when the initial Si concentration in Al melt is 0.14%, 0.20%, 0.38%, 0.77% and 1.07%, respectively. At the same temperature, considering that Si concentration is low and has limited influence on the Ti solubility, the Ti solubility in different Al-Si melts should be very close. Therefore, the Al loss which is caused by the formation of Al$_3$Ti should be the same. The discrepancy of the mass change of Al is basically attributed to that different Al atoms in Al$_3$Ti were substituted by Si and the substituted Al atoms are returned to Al melt, while the Si concentration in Al$_3$Ti is increased with increasing initial Si concentration in Al melt.
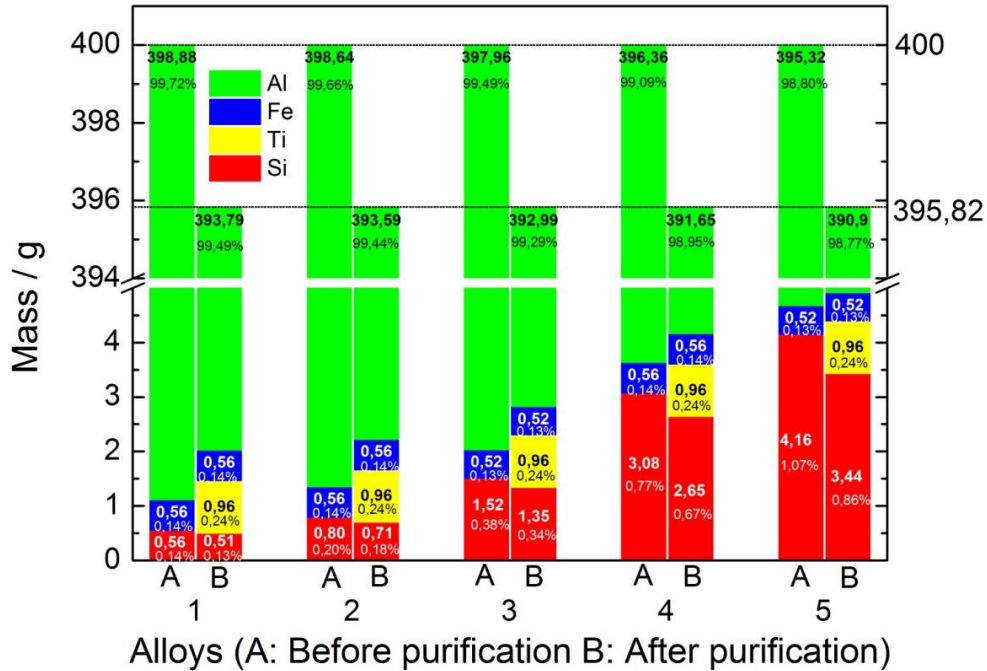
Figure 4.11. Mass of element in Al melts before and after Si purification

The mass reduction of Si is increased with increasing initial Si concentration in Al melt because of the different Si concentration in Al_3Ti. Although Si concentration decrease with 4 g Ti addition is limited especially for Al melts containing very low Si concentration, 30.77 g, 44.44 g, 47.06 g, 59.7 g and 83.72 g pure Al is required to achieve the same decrease of Si concentration for Al melt containing 0.14%, 0.20%, 0.38%, 0.77% and 1.07% Si, respectively.

The remaining Ti in Al melt is 0.96 g (0.24%) after purification for all Al melts. The upper limit of Ti in the nominal composition of 7075 and 2024 is 0.20% and 0.15%, respectively. Though the remaining Ti is hardly harmful to the properties of high strength Al alloy compared to impurity Si, the residual Ti in the purified Al melt exceed the Ti upper limit of 7075 Al alloy and 2024 Al alloy. But, the residual Ti in the purified Al melt can be decreased with the decreasing holding temperature. Fe concentration in Al melt did not change due to the small change of total mass.

4.2.3.3 Influence of holding temperature

The selected holding temperatures were 700 ^{o}C, 720 ^{o}C, 760 ^{o}C and 800 ^{o}C to investigate the influence of holding temperature on the Si purification efficiency. In all tests, the holding time was 60 min, the used Ti addition was 1 wt% and the initial Si concentration was 0.21 wt%. The Si contents after purification at different holding temperatures are shown in Figure 4.12. The decrease of Si concentration is almost constant at 0.02%

though the temperature is increased from 720 ^{o}C to 760 ^{o}C, and just improved to 0.03% when the temperature is 800 ^{o}C. The measured residual Ti in the upper part of Al melt (purified Al without (Al,Si)$_3$Ti particulates) is 0.18 wt%, 0.24 wt%, 0.32 wt% and 0.39 wt% when the holding temperature is 700 ^{o}C, 720 ^{o}C, 760 ^{o}C and 800 ^{o}C respectively. Considering that the solubility of Ti in the Al melt is increased with the temperature according to equation (4-2), the amount of precipitated Al$_3$Ti particle should be correspondingly reduced at 800 ^{o}C, while more Si was removed from Al melt, indicating that the concentration of Si in Al$_3$Ti was increased at 800 ^{o}C. The Si concentration in Al$_3$Ti is increased from 1.08 at.% to 1.31 at.% when the holding temperature is increased from 700 ^{o}C to 800 ^{o}C. But the influence of temperature on the purification efficiency is very limited when the initial Si concentration in Al melt is lower than 0.2 wt%.
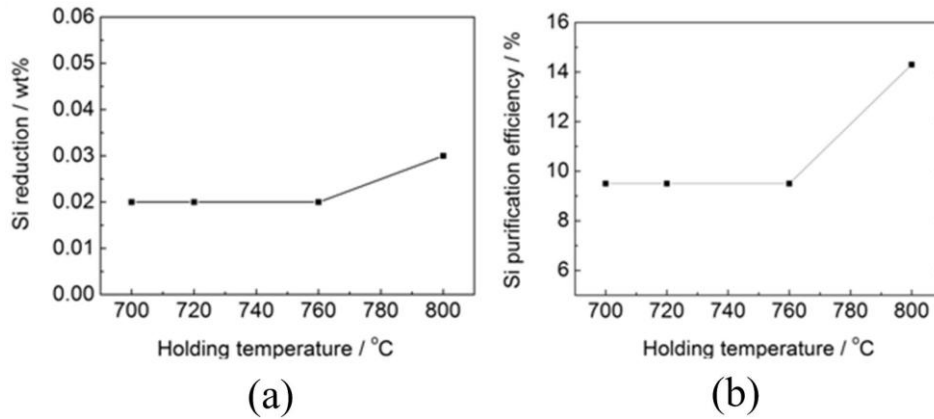
Figure 4.12. Purification results of Al melt containing 0.21 wt% Si at different holding temperatures, with 1 wt% Ti addition. (a) The decrease of Si concentration and (b) the Si purification efficiency.

4.2.3.4 Influence of K$_2$TiF$_6$ addition amount

Different amounts of Ti (0.5 wt% and 2 wt%) were added to Al melt at different temperatures. The purification efficiency and Si concentration variation in Al$_3$Ti are shown in Table 4.4. The holding time was different but apparently enough to accomplish the substitution process of Si in Al$_3$Ti, as the detected Si concentration in the upper part of Al melt has not been changed in the extended time.

Table 4.4. The Si concentration in Al$_3$Ti and the purify efficiency with different addition of Ti at different temperatures.

Initial Si Concentration / wt%	Ti concentration / wt%	Holding temperature / ^{o}C	Holding time / min	Measured Si concentration in Al$_3$Ti by EDS / at.%	Si concentration after purification / wt%	Si purification efficiency / %
0.21	0.5	800	90	1.65	0.190	9.5
0.21	2	800	120	1.02	0.170	19
0.21	2	720	120	0.77	0.175	16

The Si concentration in Al$_3$Ti is generally decreased with increasing Ti concentration at the same temperature because the quantity of Al$_3$Ti particles increases with a higher Ti addition. Si concentration after purification with 2 wt% Ti addition maintains a small fluctuation when the holding temperature was increased from 720 °C to 800 °C, indicating that the effect of temperature on purification efficiency is limited when the initial Si concentration in Al melt is low. But, the removed Si concentration from Al melt under 720 °C slightly increased from 0.02 to 0.04 wt% when the Ti addition amount is enhanced from 0.5 to 2 wt%. Neither TiSi phase nor any other Si-rich phase was found in Al melt with 2 wt% Ti addition.

The measured residual Ti in the purified Al melt is 0.23 wt% and 0.39 wt% when the holding temperature is 720 °C and 800 °C respectively, which is similar to the residual Ti of purified Al melt after purification with 1 wt% Ti addition.

4.2.4 Conclusion

All elements of the periodic table were considered for the selection of feasible elements which can react with low concentration Si in Al melt and form binary or ternary phases with a high melting point, meanwhile, the phases can be easily removed to decrease impurity Si concentration. Titanium is found to be the probable candidate after the evaluation of Al-Si-X ternary phase diagrams.

The Si purification experiment with Ti addition in the form of K$_2$TiF$_6$ indicated that Si can substitute Al in Al$_3$Ti phase and form a high melting point particle (Al$_{1-x}$,Si$_x$)$_3$Ti, but no TiSi or other Si-rich binary phases were found after purification with 2 wt% Ti addition. Si concentration can be decreased by removing (Al$_{1-x}$,Si$_x$)$_3$Ti phase from Al melt, but Si purification efficiency is closely related to the initial Si concentration in Al melt. With the addition of 1 wt% Ti in Al-Si melt, the decrease of Si concentration is only by 0.01 wt% when the initial Si concentration is 0.14 wt%. However, the decrease of Si concentration is increased to 0.17 wt% for Al melt when the initial Si concentration is 1.04 wt%. The Si concentration in Al$_3$Ti is increased with increasing initial Si concentration in Al melt. The calculation results based on 1 wt% Ti addition amount and Si concentration decrease indicate the Si concentration in Al$_3$Ti was increased from 0.57 to 9.12 at.% when the initial Si concentration in Al melt is enhanced from 0.14 to 1.04 wt%.

The holding temperature has almost no influence on Si purification efficiency when the Si initial concentration in Al melt is lower than 0.20 wt%. Though the increase of Ti addition amount can slightly improve the Si removal from Al melt containing 0.2 wt% Si, but will consume more Al. Hence, the Si purification efficiency by alloying method with Ti addition is poor for Al melt with low Si initial concentration.

4.3 Si substitution behaviour in Al₃Ti - first-principles study

4.3.1 Methods

First-principles calculations were performed in order to study the intrinsic physical mechanism of Si substitution in Al_3Ti as well as the potential of Ti addition for impurity Si removal from Al The calculations presented in this paper were accomplished using the CASTEP (Cambridge Sequential Total Energy Package) code, which is based on density-functional theory (DFT), and a plane-wave basis set was employed for expansion of the electronic wave-function [63]. In this method, interactions of core and valence were represented by ultra-soft pseudopotentials (USP) [64] and the exchange-correlation energy was treated by the generalized gradient approximation (GGA) of Perdew et al. (PW91) [65]. For a 32-atom Al_3Ti supercell, a $3\times3\times3$ Monkhorst-Pack k-point mesh was used for Brillouin zone integrations [66]. The crystal structures were fully optimized by independently modifying lattice parameters and internal atomic coordinates. The Broyden–Fletcher–Goldfarb–Shanno minimization scheme [67] was used to minimize the total energy and interatomic forces. A generalized synchronous transit method was used for locating transition state structures or first-order saddle point [68]. The LST/QST algorithm combines the linear (LST) or quadratic synchronous transit (QST) methods with conjugate gradient (CG) refinements. Searching of the transition state began by performing an LST/optimization calculation, followed by a QST/maximization calculation. From the point thus obtained, CG minimization was performed to refine the saddle point geometry. The cycle was repeated until a stationary saddle point (transition state) was located [69]. The setting of calculation parameters and the convergence have been verified by comparing the obtained formation energy of Al_3Ti (-1.56 eV) with those of previous research works [70-71]. The calculations of total energies were carried out at 0 K without the entropic contributions. In this chapter, our conclusions are valid for higher temperatures only as long as the effect of the entropy of system studied is sufficiently small.

The influence of interaction between defects in neighbouring cells is also evaluated and the difference of vacancy formation energy or vacancy migration energy between 128 atoms Al_3Ti system and 32 atoms Al_3Ti system is less than 0.02 eV (error band), which indicated that a 32-atom system is big enough to evaluate vacancy formation and migration energy in this research work.

4.3.2 Models

$D0_{22}$-Al_3Ti crystallizes in the I4/mmm space group, the lattice constants were fixed at the values of a=b=0.3851 nm, c=0.8611 nm in previous experimental studies [72-74]. There are six Al atoms located at two kinds of non-equivalent locations (denoted as Al1 and Al2) and two Ti atoms in one Al_3Ti unit cell, which is shown in Figure 4.13. The employed models in first-principles calculations were built up by using $2\times2\times1$ supercells (containing 32 atoms).
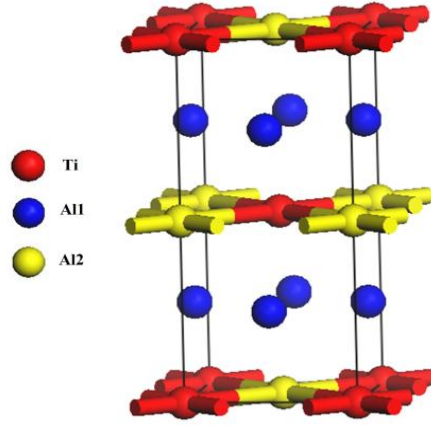
Figure 4.13. The unit cell of D0$_{22}$ structure Al$_3$Ti.

4.3.2.1 Si Site preference

The given Si doping concentrations are 3.125 at.%, 6.25 at.%, 12.5 at.%, 18.75 at.% and 25 at.% respectively in this research. The total energy minimization optimization was conducted to obtain the heats of formation of clean Al$_3$Ti and Al$_3$Ti with doped Si. The Si site preference was gained by comparing the calculation results of supercells where different concentrations of Al1, Al2 and Ti sites are occupied by Si atoms.

Our calculation results indicated that the total energy of Al$_3$Ti configuration where doped Si atoms were loosely distributed is lower compared to that of Al$_3$Ti configuration where doped Si atoms were compactly distributed (Si atoms group together). The difference is 0.07 eV when the Si doping concentration is 12.5 at.%. Therefore, doped Si atoms locations are chosen to make the distance between doped Si atoms as far as possible in our configuration, to minimize the interaction between doped Si atoms. The Al$_3$Ti configurations containing 12.5 at.% Si are shown in Figure 4.14.
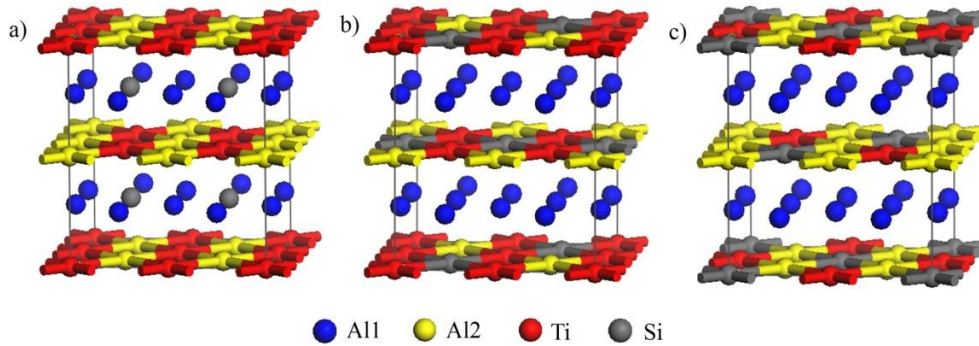
Figure 4.14. Models of D0$_{22}$-Al$_3$Ti doped 12.5 at.% Si. a) Si atoms occupy Al1 sites, b) Si atoms occupy Al2 sites and c) Si atoms occupy Ti sites.

113

4.3.2.2 Point defects formation

● Al1   ○ Al2   ● Ti   ○ Vacancy
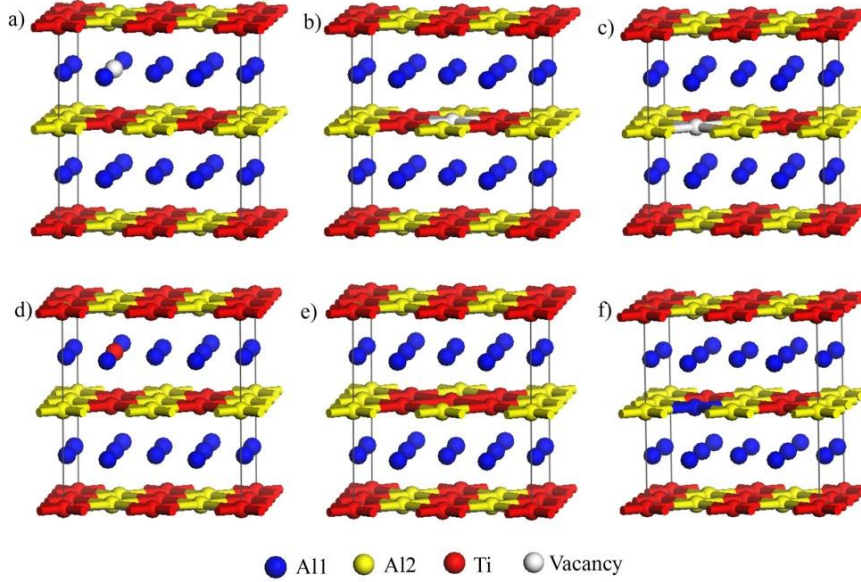
Figure 4.15. Models of Al₃Ti containing various point defects. a) Al1 vacancy, b) Al2 vacancy, c) Ti vacancy, d) Ti occupies Al1 site, e) Ti occupies Al2 site, and f) Al occupies Ti site.

The vacancy configuration was represented by a $2\times2\times1$ supercell containing 31 atoms, i.e., one Al or Ti atom has been removed. The antisite configuration was also built in a $2\times2\times1$ supercell containing 32 atoms ($Al_{25}Ti_7$ or $Al_{23}Ti_9$). All concentrations of point defects in the calculations are 3.125 at.%. The figurations of Al₃Ti containing various point defects are presented in Figure 4.15.

The relative position between a doped Si atom and a vacancy has a crucial influence on the formation energy of that vacancy. In this research, we did not discuss all relative positions between doped Si atom and vacancy, and we placed the vacancy on the site nearest to the doped Si atom in our configurations, to strengthen the effect of doped Si on vacancy formation. The doped Si site was fixed first, and then we placed the vacancy on the Al1 site, Al2 site and Ti site respectively nearest to the doped Si atom. The formation energies of Al1, Al2 and Ti vacancies were calculated in Al₃Ti supercells where Si occupies Al1, Al2 and Ti site respectively. Both vacancy concentration and doped Si concentration are 3.125 at.%.

4.3.2.3 Diffusion mechanism of vacancies and doped Si in Al₃Ti

The possible migration paths of Al1, Al2 and Ti vacancies are shown in Figure 4.16.

Figure 4.16. Migration paths for the first nearest-neighbour hop, the second nearest-neighbour hop and the intra sublattice hop of Al1, Al2 and Ti vacancy in D0$_{22}$-Al$_3$Ti. The arrows represent the migration paths.

The first and second nearest-neighbour hops as well as the intra sublattice hops were considered, and the migration distances are listed in Table 4.5.

Table 4.5. Migration paths of Al1, Al2 and Ti vacancy and the migration distances (in Å) of vacancies in different hop behaviour. a *(3.851 Å) and c (8.611 Å) are the lattice constants of Al$_3$Ti unit cell.*

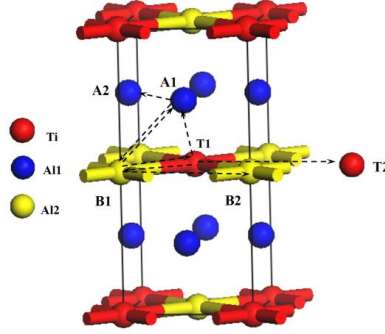|	First nearest-neighbour hop		Second nearest-neighbour hop		Intra sublattice hop	
	Migration path	distance	Migration path	distance	Migration path	distance
V_{Al1}	A1→A2	$\frac{\sqrt{2}}{2}a$	A1→B1	$\sqrt{\left(\frac{c}{4}\right)^2+\left(\frac{a}{2}\right)^2}$	A1→A2	$\frac{\sqrt{2}}{2}a$
V_{Al2}	B1→T1	$\frac{\sqrt{2}}{2}a$	B1→A1	$\sqrt{\left(\frac{c}{4}\right)^2+\left(\frac{a}{2}\right)^2}$	B1→B2	a
V_{Ti}	T1→B1	$\frac{\sqrt{2}}{2}a$	T1→A1	$\sqrt{\left(\frac{c}{4}\right)^2+\left(\frac{a}{2}\right)^2}$	T1→T2	a

For Al1 vacancy (A1 in Figure 4.16), there are four symmetry equivalent paths via which it can hop to the nearest-neighbour sites, e.g. A1→A2 as shown in Figure 4.16. The hops are also intra sublattice hops. There are two kinds of second nearest-neighbour hops for A1 vacancy, A1→B1 and A1→T1, which have the same migration distance, but A1→T1 hop will create antisite Ti$_{Al}$. Both A1→B1 and A1→T1 hops have four symmetry equivalent paths. The migration energy barriers of the two different hops were calculated by application of CASTEP, and the results indicate that the migration energy barrier of A1→T1 hop is about two times higher than that of A1→B1 hop. Therefore, the research was focused on this kind of A1→B1 hop in second nearest-neighbour hops which is obviously more possible to occur. For Al2 vacancy (B1 in Figure 4.16), the first and second nearest-neighbour hops are B1→T1 hop and B1→A1 hop, which have four and eight symmetry equivalent paths, respectively. The migration distances of Al2 vacancy are the same as that of Al1 vacancy in the first and second nearest-neighbour hops. Besides, the intra sublattice hops B1→B2 for Al2 vacancy were also considered, which have four symmetry equivalent paths. Antisites are formed in both the first and second nearest-

neighbour hops of Ti vacancy (T1 in Figure 4.16). The intra sublattice hop of Ti vacancy is shown in Figure 4.16, and T2 atom is located at the neighbouring unit cell. There are four, eight and four symmetry equivalent paths for T1→B1, T1→A1 and T1→T2 hops, respectively.

To study the effect of Si doping on the vacancy migration, we firstly placed a doped Si atom on one of the lattice sites (Al1, Al2 or Ti), then a vacancy (Al1, Al2 or Ti) nearest to the doped atom was created. For the vacancies in the Si-doped Al$_3$Ti, we examined all possible first and second nearest-neighbour hops as well as intra sublattice hops as done for pure Al$_3$Ti. Moreover, all migration paths via which Si hops to the nearest Al1, Al2 or Ti vacancy were calculated to reveal its diffusion behaviour mediated by vacancies.

4.3.3 Results and discussion

4.3.3.1 Si site preference

The calculation of the heat of formation was carried out to facilitate a comparison of the site preference, phase stability, and bonding [75-76]. In order to determine the heat of formation, we first obtained the total energy per atom in fcc Al, hcp Ti, and diamond Si. The difference between total energy of the compound and the concentration-weighted sum of the total energy of the constituent elements gives the heat of formation, the formula as follows [77]

$$\Delta H_{(P=0)}^{F} = E_{total}^{Al_{n_{Al}}Ti_{n_{Ti}}Si_{n_{Si}}} - n_{Ti}E_{total}(Ti) - n_{Al}E_{total}(Al) - n_{Si}E_{total}(Si) \qquad (5\text{-}1)$$

where $\Delta H_{(P=0)}^{F}$ is the heat of formation of $Al_{n_{Al}}Ti_{n_{Ti}}Si_{n_{Si}}$ system, $E_{total}^{Al_{n_{Al}}Ti_{n_{Ti}}Si_{n_{Si}}}$ is the total energy of Al$_3$Ti system containing doped Si atom, $E_{total}(i)$ (i=Al, Ti, Si) is total energy per atom in i bulk phase, n_i is the i atomic concentration.

In order to facilitate comparison, the obtained heats of formation of 4-atom supercells which are converted from the total formation energy of 32-atom supercells are shown in Figure 4.17. The heats of formation of supercells where Si occupies an Al site were always smaller than those of supercells where Si occupy Ti sites at the same Si concentration level, which indicated that the supercells where Si occupies an Al site were more stable than the supercells where Si occupies a Ti site. The calculated results are consistent with experimental results that Si has preference for Al sites. Hence, we mainly focused on the heat of formation of supercells where Si atom occupies Al sites. The curves show that the heats of formation of supercells where Si atom occupies Al2 site are always smaller than those of supercells where Si occupies Al1 site at the same Si doped concentration level. But, the heat of formation of supercell where Si occupies Al1 is very close to that of supercell where Si occupies Al2 at low Si doping concentration (Si<3.125at.%). Therefore, Si atom generally prefers to occupy an Al2 site but both Al1 and Al2 site are preferred at low Si doping concentration (Si<3.125at.%).
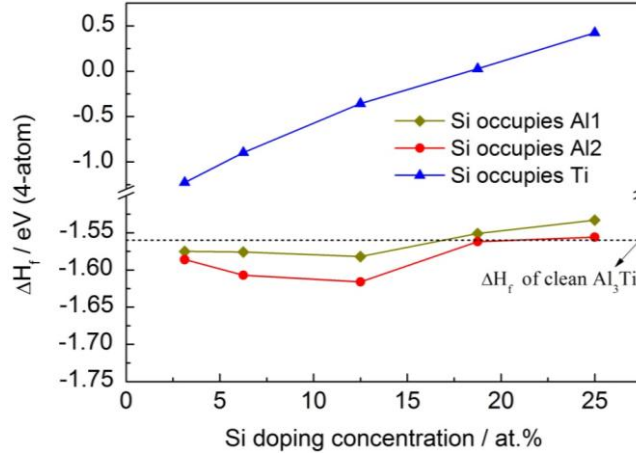
Figure 4.17. The heats of formation of Al$_3$Ti with different doped Si concentrations.

In summary, the site preference of Si in Al$_3$Ti is studied by using the first-principle calculation. All the heats of formation of supercells where Si occupy Al2 sites are lower than other substitution ways, thus Si atom generally has a clear preference to substitute Al2 atom due to the relationship between system energy and stabilization. But, both Al1 and Al2 site are preferred at low Si doping concentration (Si<3.125at.%).

4.3.3.2 Point defects formation

Lattice constants

The lattice constants of fully relaxed systems containing one vacancy obtained by application of CASTEP are listed in Table 4.6. Almost all lattice constants of systems are decreased after the occurrence of vacancies but the lattice constant "a" of the system containing one Ti vacancy. The lattice constant "a" of the system with one Al1 vacancy is 3.846 Å, having a largest variation of 0.005 Å. But the largest shrinkage for constant "c" of 0.036 Å occurs in the system with one Ti vacancy and the c/a ratio is decreased from 2.236 to 2.224. The values of c/a ratio of the systems with one Al1 and Al2 vacancy are 2.237 and 2.232, respectively, deviating slightly from the ideal value.

Table 4.6. Lattice constants of ideal (32-atom) and fully relaxed (fr) (31-atom) Al$_3$Ti.

	a (Å)	c (Å)	c/a
Ideal	3.851	8.611	2.236
V_{Al1} (fr)	3.846	8.605	2.237
V_{Al2} (fr)	3.850	8.594	2.232
V_{Ti} (fr)	3.855	8.575	2.224

Vacancy formation energies of point defects in Al₃Ti

The vacancy formation energy is defined as the energy required moving one atom on the lattice site into an atomic reservoir of the same species [79]. Lower formation energy means the related system is more stable, and the vacancy is more likely to occur. According to references [49, 79-80], the vacancy formation energy of species j, denoted as $E_v^F(j)$, can be calculated as follows

$$E_v^F(j) = \Delta E(j) + \mu_j \tag{5-2}$$

$$\Delta E(j) = E_{total}^v + E_{total}(j) - E_{total} \tag{5-3}$$

μ_j is the chemical potential of the j-species solid in the reservoir [79]. $\Delta E(j)$ is the vacancy formation energy under j-species rich condition, i.e., μ_j is zero (as shown in Figure 4.18). E_{total} and E_{total}^v are the total energies of the perfect Al₃Ti crystal and the crystal containing one j-species vacancy, respectively. $E_{total}(j)$ is the total energy per atom in j-species solid.

Based on the vacancy formation energy calculation formulas, similarly we can calculate the antisite formation energy as follows

$$E_{anti}^F(j) = \Delta E(j) + (\mu_2 - \mu_1) \tag{5-4}$$

$$\Delta E(j) = E_{total}^{anti} + E_{total}(2) - E_{total} - E_{total}(1) \tag{5-5}$$

where μ_1 and μ_2 are the chemical potential per substitutional and substituted atom in the reservoir, respectively. $\Delta E(j)$ is the antisite formation energy ignoring the difference of chemical potentials between substitutional and substituted atom in the reservoir. E_{total} and E_{total}^{anti} are the total energies of the perfect Al₃Ti crystal and the crystal containing one antisite, respectively. $E_{total}(1)$ and $E_{total}(2)$ are the total energies per atom of substitutional and substituted atom species solid, respectively.

For calculating the defect formation energy, the chemical potential of j atom in the reservoir needs to be determined. To do this, the equilibrium conditions, i.e., the formation enthalpy of Al₃Ti is equal to the sum of chemical potentials of these constitution atoms, can be considered firstly as follows [79]

$$3\mu_{Al} + \mu_{Ti} = \Delta H(Al_3Ti) \tag{5-6}$$

where ΔH (Al₃Ti), the formation enthalpy of formula unit Al₃Ti, is given by

$$\Delta H(Al_3Ti) = E_{total} - 3E_{total}(Al) - E_{total}(Ti) \tag{5-7}$$

Moreover, to avoid the precipitation of unwanted secondary phase (elemental solid), the energy of an atom in reservoir should not be bigger than that in the secondary phase [79] which means

$$\mu_{Al} \leq 0, \ \mu_{Ti} \leq 0 \tag{5-8}$$

Using equations (5-6) and (5-8), μ_{Al} and μ_{Ti} can be determined as follows:

$$\frac{\Delta H(Al_3Ti)}{3} \leq \mu_{Al} \leq 0, \quad \Delta H(Al_3Ti) \leq \mu_{Ti} \leq 0 \tag{5-9}$$

The calculated $\Delta H(Al_3Ti)$ is -1.563 eV. So, in the Ti-rich condition, i.e., $\mu_{Ti} \approx 0$ eV, $\mu_{Al} \approx \dfrac{\Delta H(Al_3Ti)}{3} = -0.521$ eV; while in the Al-rich condition, i.e., $\mu_{Al} \approx 0$ eV, $\mu_{Ti} \approx \Delta H(Al_3Ti) = -1.563$ eV, as shown in Figure 4.18.
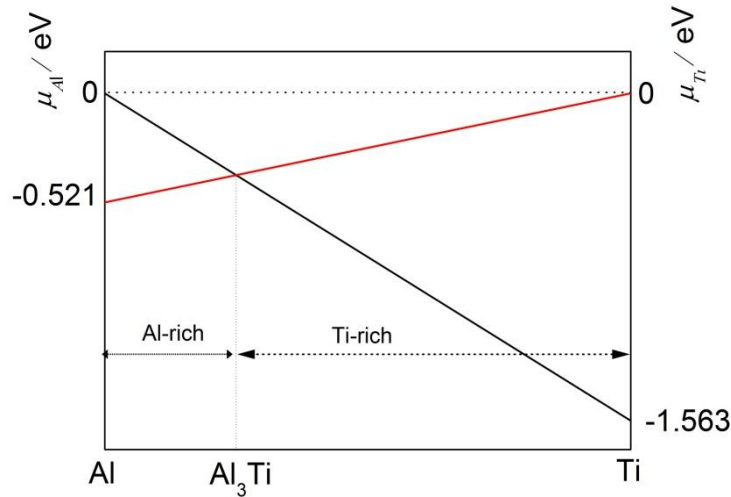
Figure 4.18. The range of the chemical potential of Al and Ti in the reservoir under two extremes, Al-rich and Ti-rich conditions.

The calculated formation energies of various point defects are shown in Figure 4.19. It is found that the formation energies of Ti-poor point defects (Al_{Ti} and V_{Ti}) are lower than those of Al-poor point defects (V_{Al1}, V_{Al2}, Ti_{Al1} and Ti_{Al2}) under Al-rich condition, but on the contrary, higher than those of Al-poor point defects under Ti-rich condition. For Ti-poor point defects, the formation of antisite Al_{Ti} is more probable than V_{Ti} under Al-rich condition but more difficult than V_{Ti} under Ti-rich condition. For Al-poor point defects, the formation energies of Ti_{Al1} and Ti_{Al2} are lower than those of V_{Al1} and V_{Al2} over the whole range of the Ti chemical potential, respectively. The calculation shows that Al_{Ti} is most

119

likely to occur under Al-rich condition while the formation of Ti_{Al2} is most probable under Ti-rich condition. As vacancies, the formation energies of Al1, Al2 and Ti vacancies under Al-rich condition are 2.55 eV, 2.35 eV and 0.83 eV, respectively, which reveals that Ti vacancy is more likely to form than Al1 and Al2 vacancies in the practical Si purification experiment, where Al-rich condition is obviously satisfied. Only in a small range near the ultimate Ti chemical potential, Al1 and Al2 vacancies are more probable to appear than Ti vacancy.
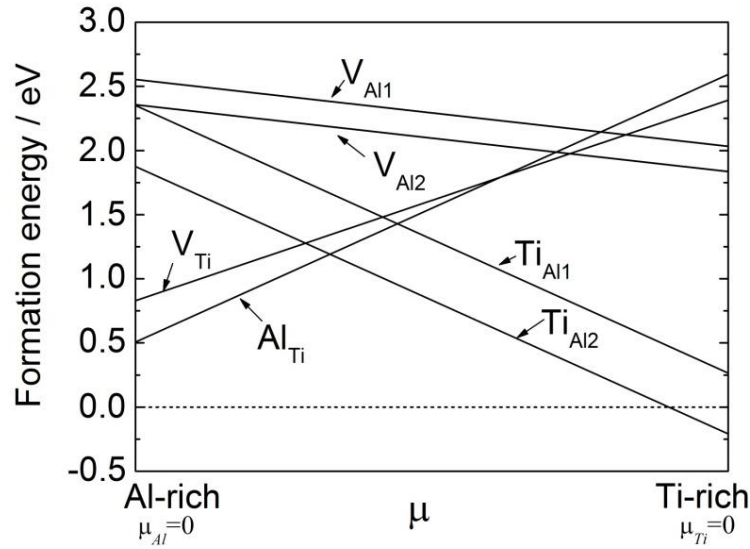
Figure 4.19. The ranges of formation energies of different point defects under two extremes, Al-rich and Ti-rich conditions.

Effect of doped Si on vacancy formation in Al₃Ti

The formation energies of Al1, Al2 and Ti vacancies were calculated in Al₃Ti supercells where Si occupies Al1, Al2 and Ti site, respectively. The vacancy formation energy is defined as the energy required to moving an atom from the host solid into the atomic reservoir of the same species [79]. Lower formation energy means the system is more stable, and the vacancy is more likely to occur.

The vacancy formation energy can be calculated by the equation below [49, 79-80]:

$$E_v^F (Si, j) = E_{total}^{(Si+v)} + E_{total}(j) - E_{total}^{(Si)} + \mu_j \tag{5-10}$$

where $E_v^F (Si, j)$ is the vacancy formation energy and μ_j is the chemical potential of the j-species solid in the reservoir. $E_{total}^{(Si)}$ is the total energy of Al₃Ti system containing one doped Si atom. $E_{total}^{(Si+v)}$ is the total energy of Al₃Ti system containing one doped Si atom

and one j-species vacancy simultaneously. $E_{total}(j)$ is the total energy per atom in j-species solid. As mentioned above (Figure 4.18), in the case of Ti-rich condition, $\mu_{Ti} \approx 0$ eV, $\mu_{Al} \approx \dfrac{\Delta H(Al_3Ti)}{3} = -0.521$ eV, , and $\mu_{Al} \approx 0$ eV and $\mu_{Ti} \approx \Delta H(Al_3Ti) = -1.563$ eV under Al-rich condition.

Considering that the Si removal process was conducted under Al-rich condition, vacancy formation energies in pure and Si-doped Al$_3$Ti under Al-rich condition are calculated, and the results are shown in Figure 4.20. The formation energies of Al1 vacancies are decreased after Si doping. The formation energy decrements are 0.1 eV, 0.16 eV and 0.63 eV when Si occupies Al1 site, Al2 site and Ti site, respectively. Therefore, Si doping can promote the formation of Al1 vacancy. The same is true for the formation of Al2 vacancy, and the formation energy decrements are 0.28 eV and 0.14 eV when Si occupies Al1 and Al2 sites, respectively. The formation energy of Al2 vacancy is negative (-0.36 ev) when Si occupies Ti site, which indicates that the system where Si occupies Ti is not stable, it is consists with Si site preference. The formation energy of Ti vacancy is also slightly decreased from 0.83 eV to 0.71 eV when Si occupies Al1 site. The formation of Ti vacancy is a little difficult when Al2 site or Ti site is occupied by Si.
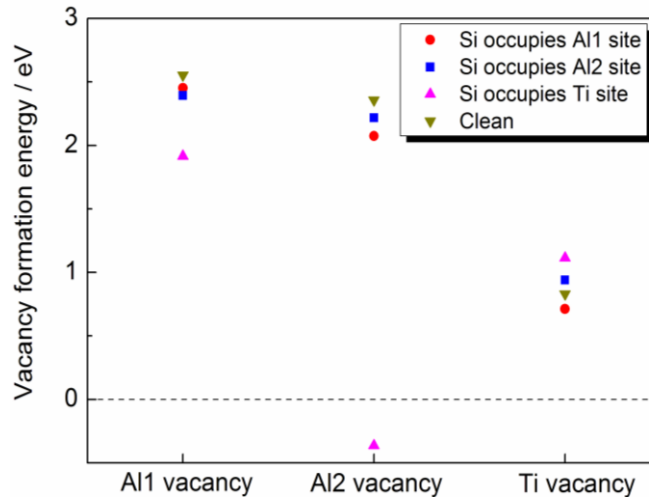
Figure 4.20. Formation energies of vacancies in pure and Si-doped Al$_3$Ti under Al-rich condition.

4.3.3.3 Diffusion mechanism of vacancies and doped Si in Al$_3$Ti

Vacancy migration in pure Al$_3$Ti

The calculated migration barriers are listed in Table 4.7. For the migration paths of Al1 vacancy, A1→A2 hop is not only the first nearest-neighbour hop, but also intra sublattice hop for Al1 vacancy. As mentioned above, A1→B1 and A1→T1 are two types of second

nearest-neighbour hops for Al1 vacancy, which have the same migration distance. The migration energy barrier of A1→T1 hop is about two times higher than that of A1→B1 hop. Therefore, A1→B1 hop was selected as the second nearest-neighbour hop which is more likely to occur. The migration energy barrier of A1→A2 hop is 0.54 eV, which is approximately 0.33 eV lower compared with that of the second nearest-neighbour hop, A1→B1. Thus, Al1 vacancy prefers to diffuse by jumping to the first nearest-neighbour site, which indicates that the diffusion of Al1 atom is most likely to occur on its own sublattice. Moreover, the migration path A1→B1 is also a choice for Al1vacancy because of the lower migration energy of 0.87 eV, it is therefore probable that Al2 atom diffuses to the nearest Al1 site mediated by Al1 vacancy.

Table 4.7. The migration energies (in eV) for vacancy diffusion.

Migration energy					
Al1 vacancy		Al2 vacancy		Ti vacancy	
A1→A2	0.54	B1→T1	1.13	T1→B1	1.41
A1→B1	0.87	B1→A1	1.10	T1→A1	1.97
A1→T1	1.70	B1→B2	4.01	T1→T2	5.89

For Al2 vacancy, the migration energy for sublattice hop (B1→B2) is higher than 4 eV, and it is therefore improbable for Al2 vacancy to diffuse within Al2 sublattice, which indicates that it is impossible for Al2 atom to diffuse on its own sublattice. The migration energies of B1→T1 hop and B1→A1 hop are 1.13 eV and 1.10 eV, respectively, which indicates that both first nearest-neighbour hop and second nearest-neighbour hop are possible for Al2 vacancy. However, considering that B1→T1 hop will cause the disorder of Al_3Ti phase, so the most possible migration path for Al2 vacancy is via the second nearest-neighbour hop. It is therefore possible that Al1 and Ti atoms will diffuse to the nearest Al2 site mediated by Al2 vacancy. But considering that the migration energy of B1→A1 hop is 1.10 eV, Al1 atom is more likely to diffuse via nearest Al1 site mediated by Al1 vacancy (A1→A2 hop) because of the lower migration energy of 0.54 eV.

Ti vacancy cannot jump effectively via intra sublattice hop (T1→T2) due to the high migration energy of 5.89 eV, as given in Table 4.7. It is therefore impossible that Ti atom will diffuse on its own sublattice. From the energy point of view, the most possible hop is the first nearest-neighbour hop (T1→B1), which has a lower migration energy of 1.41 eV compared with the second nearest-neighbour hop (T1→A1). But this kind of hop will cause the disorder of Al_3Ti phase. So, it is difficult for Al1 atom to diffuse via nearest Ti site mediated by Ti vacancy because of the high migration energy, 1.97 eV. Although it is possible for Al2 atom to diffuse via nearest Ti site mediated by Ti vacancy, but considering that the migration energy of T1→B1 hop is 1.41 eV, Al2 atom is more likely to diffuse via nearest Al1 site mediated by Al1 vacancy (A1→A2 hop) because of the lower migration energy of 0.87 eV.
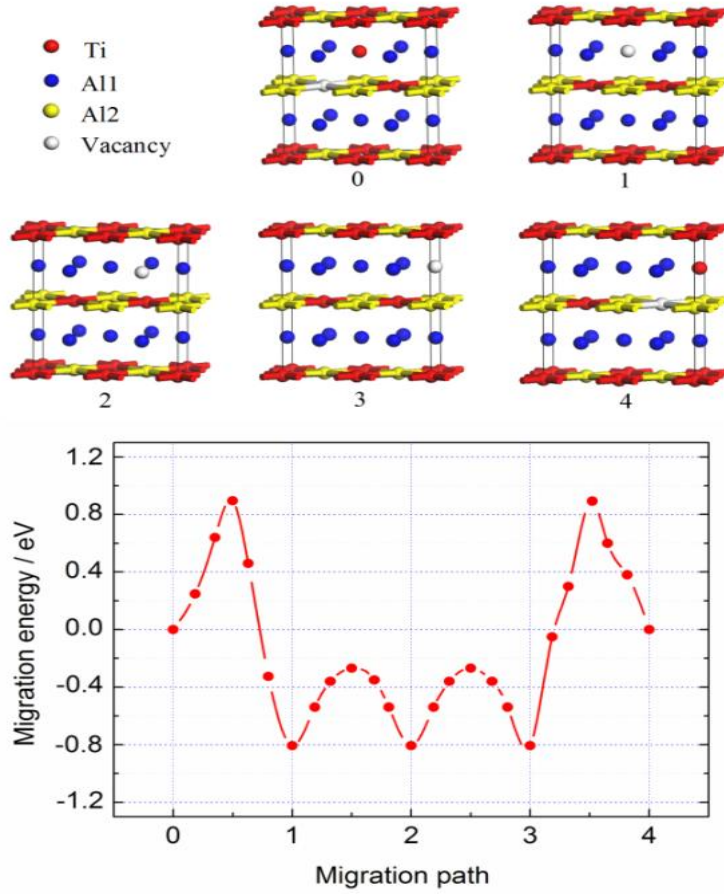
Figure 4.21. Ti vacancy intra sublattice migration paths and migration energies in double-defect Al₃Ti configuration.

Considering the high migration energy of intra sublattice hop for Ti vacancy, a diffusion mechanism involving the net migration of a two-defect complex which consists of a Ti vacancy and an antisite Ti_{Al1} in a $2\times2\times1$ supercell was considered for the migration of Ti vacancy. The migration sequence includes four hops separated by three intermediate configurations. The final result of a two-defect complex migration sequence is the intra sublattice hop of Ti vacancy and the migration of an antisite Ti_{Al1}. The migration details are presented in Figure 4.21, and five concise 16-atom configurations were employed to clearly describe the migration paths instead of the real 32-atom configurations. The migration path in fact consists of one second nearest-neighbour hop of Ti vacancy (0→1), two first nearest-neighbour hops of Al1 vacancy (1→2 and 2→3) and one second nearest-neighbour hops of Al1 vacancy (3→4). The four hops are chosen based on the obtained migration energies of vacancies which are listed in Table 4.7. The migration energies of first and second nearest-neighbour hop of Al vacancy are lower than that of intra sublattice hop.

123

Though the migration energy of second nearest-neighbour hop of Ti vacancy is slightly higher than that of first nearest-neighbour hop, but it is much lower compared to the migration energy of the intra sublattice hop. To simplify the diffusion mechanism of Ti vacancy, other complex diffusion mechanisms are not discussed.

The largest migration energy barrier of 1.70 eV for this two-defect complex hop sequence occurs in the 3→4 hop, and it is decreased with a significant amount compared with the migration energy of direct intra sublattice hop for Ti vacancy. However, the equilibrium concentration of the two defects has an important influence on this kind of migration mechanism.

Vacancy migration in Si doped Al$_3$Ti

Various migration paths of vacancies were examined to study the effect of Si doping on the vacancy migration. The calculated migration energies are presented in Table 4.8. By comparing the migration energies, it is clear that the most possible migration paths of Al2 and Ti vacancy in Si-doped Al$_3$Ti are B1→A1 hop and T1→B1 hop, respectively, which are consistent with the calculated results in pure Al$_3$Ti. The most possible migration paths for Al1 vacancy are also consistent with that in pure Al$_3$Ti when Si occupies Al1 or Al2 site. However, the preferred migration path of Al1 vacancy is A1→B1 hop when Si occupies Ti site.

Table 4.8. Vacancy migration energies (in eV) in Si-doped Al$_3$Ti.

Migration path		Migration energy		
		Si occupies Al1 site	Si occupies Al2 site	Si occupies Ti site
V_{Al1}	A1→A2	0.46	0.36	0.66
	A1→B1	0.78	0.77	0.53
V_{Al2}	B1→T1	1.06	1.11	1.00
	B1→A1	1.01	0.89	0.72
	B1→B2	4.06	3.57	1.88
V_{Ti}	T1→B1	1.45	0.97	0.83
	T1→A1	1.83	1.66	1.12
	T1→T2	5.99	3.47	3.59

For Al$_3$Ti where Si occupies Al1 site, most of the migration energies were slightly decreased, but the migration energies for B1→B2 hop, T1→B1 hop and T1→T2 hop are slightly increased compared with those of pure Al$_3$Ti. All the variations of migration energies are small (no more than 0.15 eV), therefore, Si doping has little influence on migration energy of vacancy when Si occupies Al1 site in Al$_3$Ti.

For Al$_3$Ti where Si occupies Al2 site, all migration energies of vacancies are decreased compared with those of pure Al$_3$Ti, especially the migration energies for intra sublattice

hops of Al2 and Ti vacancies and the preferred migration path of Ti vacancy, T1→B1 hop. Comparing to migration energies of pure Al_3Ti, the migration energy decrements of B1→B2 hop, T1→B1 hop and T1→T2 hop are 0.44 eV, 0.44 eV and 2.42 eV, respectively

For Al_3Ti where Si occupies Ti site, the migration energy is elevated by 0.12 eV for intra sublattice hop of Al1 vacancy compared with that in pure Al_3Ti. The other migration energies of vacancies are decreased, and almost all decrements are larger than those in Al_3Ti where Si occupies Al sites. Our previous calculated results [81] indicated that Si prefers to occupy Al site than Ti site, the lower migration energies of vacancies in Al_3Ti where Si occupies Ti site may be caused due to the fact that the influence of the Ti atom substituted by Si on migration process is weakened. Both A1 and A2 atoms are not in the same lattice plane with Si_{Ti} and the effect of Si_{Ti} on A1→A2 hop is finite. This might be the reason that the variation of migration energy of A1→A2 hop is small when Si occupies Ti site compared with that in pure Al_3Ti.

In summary, most of migration energies of vacancies are decreased in Al_3Ti with Si doping, and Si doping is basically favourable to the migration of vacancies in Al_3Ti, especially in Al_3Ti where Al2 site was occupied.

Doped Si atom migration

The diffusion energies of doped Si atoms mediated by vacancies are listed in Table 4.9.

Table 4.9. Migration energies (in eV) of doped Si atom in Al_3Ti.

Migration path	Migration energy		
	Si occupies Al1 site	Si occupies Al2 site	Si occupies Ti site
Mediated by V_{Al1}	0.45	0.62	/
Mediated by V_{Al2}	0.98	3.24	/
Mediated by V_{Ti}	2.69	2.09	1.01

For the diffusion of doped Si atom on Al1 site, Si atom hopping to the first nearest Al1 vacancy needs to cross an energy barrier of 0.45 eV, which is lower than those of hops mediated by the nearest Al2 vacancy and Ti vacancy. Si atom hopping to the nearest Ti vacancy needs to cross a much larger energy barrier of 2.69 eV due to the fact that the system where Si atom is on Ti site is unstable [81]. For the diffusion of doped Si atom on Al2 site, the lowest energy barrier of 0.62 eV is needed when Si atom hops to the nearest Al1 vacancy. Si atom on Al2 site hopping to the nearest Al2 vacancy needs to overcome a large energy barrier of 3.24 eV due to the long diffusion distance and the fact that the Si atom needs to pass through a quadrangle consisting of two Ti atoms and two Al1 atoms. For the diffusion of doped Si atom on Ti site, no saddle point has been found when Si atom hops to the first nearest Al1 vacancy as well as Si atom hops to the nearest Al2 vacancy, indicating that the systems where Si occupies Ti site is unstable.

As mentioned before, Si prefers to occupy Al site, and both doped Si atoms on Al1 site or Al2 site prefer to diffuse via the nearest-neighbour Al1 vacancy. But the most probable vacancy in Al_3Ti under Al-rich condition is Ti vacancy, resulting in difficulty of Si diffusion

in Al$_3$Ti. Thus Si atom diffusion in Al$_3$Ti particles is arduous during Si removal by using Ti addition method, which is unfavourable for Si doping in Al$_3$Ti. Therefore the potential of alloying method with Ti addition for Si removal from Al alloy is poor.

4.3.4 Conclusion

The site preference of Si in Al$_3$Ti is studied by using the first-principle calculation. Most of the heats of formation of supercells where Si occupies Al2 sites are lower than those of supercells where Al1 or Ti sites are occupied by Si, thus Si atom generally has a preference to substitute an Al2 atom. But both Al1 and Al2 site are preferred at low Si doping concentration (Si<3.125 at.%).

The formation energies of point defects and the effect of vacancy on the site preference of Si in D0$_{22}$ Al$_3$Ti were investigated. For antisites, the calculated results indicate that the formation energy of Al$_{Ti}$ is lowest under Al-rich condition, 0.51 eV, which means that Al$_{Ti}$ is most likely to occur. On the other hand, the value of Ti$_{Al2}$ formation energy is lowest under Ti-rich conditions, -0.21 eV. For vacancies, the most probable vacancy is Ti vacancy under Al-rich condition, and the most probable vacancy is Al2 vacancy under Ti-rich condition. In Si-doped Al$_3$Ti, the formation energies of Al1 and Al2 vacancies under Al-rich condition are decreased compared with those in pure Al$_3$Ti, but the formation energies of Ti vacancy are slightly increased when Si occupies Al2 or Ti sites.

The vacancy migration paths in pure and Si-doped Al$_3$Ti and the effect of Si doping on vacancy formation were also studied. In pure Al$_3$Ti, both Al1 vacancy and Ti vacancy prefer to diffuse via the first nearest-neighbour hop, and the migration energy barriers are determined to be 0.54 eV and 1.41 eV, respectively. Al2 vacancy prefers to diffuse via the second nearest-neighbour hop with the migration energy barrier of 1.10 eV. The intra sublattice diffusion of Ti vacancy needs to overcome a high energy barrier of 5.89 eV, which can be dramatically reduced by a two-defect complex diffusion mechanism proposed in this work. The preferred migration paths for vacancies in Al$_3$Ti with Si doping are the same with those in pure Al$_3$Ti except the migration path of Al1 vacancy when Si occupies Ti site. Both doped Si atoms on Al1 site or Al2 site prefer to diffuse via the nearest-neighbour Al1 vacancy with the migration energy barriers of 0.45 eV and 0.62 eV, respectively. The system where Si occupies Ti site is unstable, therefore no saddle point has been found when Si hops to the first nearest Al1 vacancy and the nearest Al2 vacancy. The migration energy of Si in Al$_3$Ti is important for the calculation of the diffusion coefficient of Si in Al$_3$Ti. The diffusion rate of Si is not calculated in this chapter due to the unknown diffusion coefficient D$_0$ which is related to the frequency of vibration of Si in Al$_3$Ti, coordination number of Si in Al$_3$Ti, the interplanar spacing in the direction of Si diffusion and the crystal structure. The detailed calculation of diffusion rate of Si in Al$_3$Ti will be calculated in future work.

Si prefers to occupy Al site, both doped Si atoms on Al1 site or Al2 site prefer to diffuse via the nearest-neighbour Al1 vacancy. But the most probable vacancy in Al$_3$Ti under Al-rich condition is Ti vacancy, resulting in difficulty of Si diffusion in Al$_3$Ti. Thus Si atom diffusion in Al$_3$Ti particles is arduous during Si removal by using Ti addition method, which is unfavourable for Si doping in Al$_3$Ti. Furthermore, Si doping concentration in Al$_3$Ti

is decreased with decreasing initial Si concentration in Al alloy during Si removal experiments. Therefore the potential of alloying method with Ti addition for Si removal from Al alloy is poor.

Reference

[1] Ramanan RA, Sharkawy SW, El-zeky MA. Effect of silicon addition on the microstructure constitutents of Al-9Zn-2.5Mg alloys. Scripta Metallurgica et Materialia 27 (1992) 821.

[2] Yuan SP, Liu G. et al. Coupling effect of multiple precipitates on the ductile fracture of aged Al–Mg–Si alloys. Scripta Materialia 57 (2007) 865.

[3] Mondolfo LF. Aluminum Alloys: Structure and Properties. (1976) Butterworth, London.

[4] Srivatsan TS. The high-cycle fatigue fracture behaviour of aluminium alloy 7055. Mater. Sci. Eng. A 281 (2000) 292.

[5] Nagao M, Oosumi K, Nakamura T. Removal of impurity silicon from molten aluminum alloy with compound method. Journal of Japan Institute of Light Metals 46 (1996) 488. (In Japanese)

[6] Yang YS, Zhang QS, He YL and Hu ZQ. The segregation of copper and slicicon in Al-Si-Cu alloy during electromagnetic centrifugal solidification. Sci. Technol. Adv. Mater. 2 (2001) 271.

[7] Pan Z, Du Y, Huang BY. Experimental investigation and thermodynamic calculation in the Al–Be–Si ternary system. International Journal of Materials Research 96 (2005) 1301.

[8] Suzuki T. Aluminium-Silicon-Zinc, Ternary Alloys. VCH 8 (1993) 338.

[9] Lukas HL. Refractory Metal Systems: Phase Diagrams, Crystallographic and Thermodynamic Data. (2009) Springer-Verlag Berlin Heidelberg.

[10] Gröbner J, Mirkovic D, Schmid-Fetzer R. Thermodynamic aspects of grain refinement of Al-Si alloys using Ti and B. Mater. Sci. Eng. A 395 (2005) 10.

[11] Rogl P, Schuster JC. Phase Diagrams of Ternary Boron Nitride and Silicon Nitride Systems. ASM Int. (1992) 131.

[12] Hillert M, Jonsson S. Prediction of the Al-Si-N system. CALPHAD 16 (1992) 199.

[13] Zuo M, Liu XF, Sun QQ, Jiang K. Effect of rapid solidification on the microstructure and refining performance of Al-Si-P master alloys. Journal of Materials Processing Technology 209 (2009) 5504.

[14] Huber B, Effenberger HS, Richter KW. Phase equilibria in the Al-Si-V system. Intermetallics 18 (2010) 606.

[15] Richter KW, Gutierrez DT. Phase equilibria in the Al-Co-Si system .Intermetallics 13 (2005) 848.

[16] Pan XM, Jin ZP, Zhao JC. Determination of the isothermal sections of the Al-Ni-Si ternary system at 750 ℃ and 850 ℃. Metall. Mater. Trans. A 36 (2005) 1757.

[17] Phillips HWL. The constitution of Aluminum Copper Silicon alloys. J. Inst. Metals (London) 82 (1953) 9.

[18] Pan XM, Lin C, Morral JE, Brody HD. An assessment of thermodynamic data for the liquid

phase in the Al-rich corner of the Al-Cu-Si system and its application to the solidification of a 319 alloy. J. Phase Equilb. Diffus. 26 (2005) 225.

[19] Hansen SC, Loper Jr CR. Effect of antimony on the phase equilibrium of binary Al-Si alloys. CALPHAD 24 (2000) 339.

[20] Kadaner ES, Turkina NI, Kuz'mlna VI. Aluminum-rich range of the Al-Si-Li phase diagram, Russ. Metall. 1 (1976) 150.

[21] Lacaze J, Valdes R. CALPHAD-type Assessment of the Al–Mg–Si System. Monatsh Chem. 136 (2005) 1899.

[22] Feufel H, Godecke T, Lukas HL, Sommer F. Investigation of the Al-Mg-Si system by experiments and thermodynamic calculations. J. Alloys Compd. 247 (1997) 31.

[23] Doan G. Über das System Aluminium-Kalzium-Silizium. Z. Metallkd. 18 (1926) 350.(In German)

[24] Esslinger P, Quatrehomme F, Bleidorn H. Uber die aluminiumecke des systems Aluminium-Chrom-Silizium. Z. Metallkd. 56 (1965) 735. (In German)

[25] Chen HL, Weitzer F, Schuster JC, Du Y, Xu H. The isothermal section of the Al-Cr-Si system at 800 $^{\circ}$C and the crystal structure of τ_2 (Cr_3Al_9Si). J. Alloys Compd. 436 (2007) 313.

[26] Krendelsberger N, Weitzer F, Schuster JC. On the constitution of the system Al-Mn-Si. Metall. Mater. Trans. A 33 (2002) 3311.

[27] Du Y, Schuster JC, Weitzer F, Krendelsberger N, Huang B, Jin Z, Gong W, Yuan Z, Xu H. A thermodynamic description of the Al-Mn-Si system over the entire composition and temperature ranges. Metall. Mater. Trans. A 35 (2004) 1613.

[28] Ganiev IN, Vakhobov AV, Dzhurayev TD. The Al-Si-Sr phase diagram. Russ. Metall. 4 (1977) 175.

[29] Drits ME, Kuz'mina VI, Turkina NI. Phase-equilibria in Al-rich Al-Si-Y alloys. Russ. Metall. 3 (1980) 178.

[30] Schmid-Fetzer R. Aluminium-Barium-Silicon, ternary alloys. VCH 3 (1990) 310.

[31] Gröbner J, Mirković D, Schmid-Fetzer R. Thermodynamic aspects of the constitution, grain refining, and solidification enthalpies of Al-Ce-Si alloys. Metall. Mater. Trans. A. 35 (2004) 3349.

[32] Ghosh G. Al-Fe-Si, ternary alloys. Vol5, VCH (1992) Weinheim, Germany.

[33] Liu ZK, Chang YA. Thermodynamic assessment of the Al-Fe-Si system. Metall. Mater. Trans. A 30 (1999) 1081.

[34] Raghavan V. Fe-Sn-U (Iron-Tin-Uranium). J. Phase Equilibria 23 (2002) 362.

[35] Barlock JG, Mondolfo LF. Structure of some Aluminium-Iron-Magnesium-Silicon alloys. Z. Metallkde 66 (1975) 605.

[36] Reynolds JA, Tottle CR. The nucleation of cast metals at the mould face. J. Inst. Met. 80 (1951) 93.

[37] Raman A, Schubert K. Uber den aufbau einiger zu $TiAl_3$ verwandter legierungsreihen, 2: Untersuchungen in einigen T-Al-Si und T4…6-In-systemen. Z. Metallkde. 56 (1965) 44. (In

German)

[38] Zakharov AM, Guldin IT, Arnold AA, Matsenko YA. Izv. Akad. Nauk SSSR, Metally 4 (1988) 181.

[39] Perrot P, Aluminium-silicon-titanium, MSIT ternary evaluation program, in: G. Effenberg (Ed.), MSIT Workplace, MSI, Materials Science International Services GmbH, Stuttgart (1993) (DocumentID:10.14604.1.20).

[40] Zeren M, Karakulak E. Influence of Ti addition on the microstructure and hardness properties of near-eutectic Al-Si alloys. J. Alloys Compd. 450 (2008) 255.

[41] Yu R, He LL and Ye HQ. Effect of W on structural stability of TiAl intermetallics and the site preference of W. Phys. Rev. B 65 (2002) 184102.

[42] Jansen HJF and Freeman AJ. Total-energy full-potential linearized augmented-plane-wave method for bulk slides: electronic and structure properties of tungsten. Phys. Rev. B 30 (1984) 561.

[43] Ravi C, MathiJaya S, Valsakumar MC and Asokamani R. Site preference of Zr in Ti_3Al and phase stability of Ti_2ZrAl. Phys. Rev. B 65 (2002) 155118.

[44] Andersen OK and Jepsen O. Explicit, first-principles tight-binding theory. Phys. Rev. Lett. 53 (1984) 2571.

[45] Sluiter MHF and Kawazoe Y. Site preference of ternary additions in Ni_3Al. Phys. Rev. B 51 (1995) 4062.

[46] Sluiter MHF, Takahashi M, Kawazoe Y. The effect of magnesium on site preference in Ni_3Al. Acta Mater. 44 (1996) 209.

[47] Carara SS, Thesing LA, Piquini P. First principles study of vacancies and Al substitutional impurities in δ-TiN. Thin Solid Films 515 (2006) 2730.

[48] Kellou A, Feraoun HI, Grosdidier T, Coddet C, Aourag H. Energetics and electronic properties of vacancies, anti-sites, and atomic defects (B, C, and N) in B2-FeAl alloys. Acta Mater. 52 (2004) 3263.

[49] Zhang X, Wang CY. First-principles study of vacancy formation and migration in clean and Re doped γ′-Ni_3Al. Acta Mater 57 (2009) 224.

[50] Debiaggi SB, Decorte PM, Monti AM. Diffusion by vacancy mechanism in Ni, Al, and Ni_3Al: Calculation based on many-body potentials. Phys Status Solidi B 195 (1996) 37.

[51] Duan JS. Atomistic simulations of diffusion mechanisms in stoichiometric Ni_3Al. J Phys Condens Matter 4 (2006) 1381.

[52] Harris C, Tedstrom R, Daw MS, Mills MJ. Calculations of diffusion and diffusion-limited processes in Ni_3Al using accelerated molecular dynamics. Comput Mater Sci 37 (2006) 462.

[53] Höglund A, Castleton CWM, Mirbt S. Diffusion mechanism of Zn in InP and GaP from first principles. Phys Rev B 77 (2008) 113201.

[54] Elcock EW, Mccombie CW. Vacancy diffusion in binary ordered alloys. Phys Rev 109 (1958) 605.

[55] Stolwijk NA, van Gend M, Bakker H. Self-diffusion in the intermetallic compound CoGa. Phil Mag A 42 (1980) 783.

[56] Kao CR, Chang YA. On the composition dependencies of self-diffusion coefficients in B2 intermetallic compounds. Intermetallics 1 (1993) 237.

[57] Xu QC, Van der Ven A. First-principles investigation of migration barriers and point defect complexes in B2-NiAl. Intermetallics 17 (2009) 319.

[58] Han YF, Li K, Wang J, Shu D, Sun BD. Influence of high-intensity ultrasound on grain refining performance of Al-5Ti-1B master alloy on aluminium. Mater. Sci. Eng. A 405 (2005) 306.

[59] Han YF, Shu D, Wang J, Sun BD. Microstructure and grain refining performance of Al-5Ti-1B master alloy prepared under high-intensity ultrasound. Mater. Sci. Eng. A 430 (2006) 326.

[60] Youdelis WV. Nucleation entropy and grain refinement of alloys. Metals Sci. 13 (1979) 540.

[61] Wang XM, Jha A, Brydson R. In situ fabrication of Al_3Ti particle reinforced aluminium alloy metal-matrix composites. Mater. Sci. Eng. A 364 (2004) 340.

[62] Sigworth GK. The grain refining of aluminum and phase relationships in the Al-Ti-B system. Metall. Trans. A 15 (1984) 277.

[63] Segall MD, Lindan PLD, Probert MJ, Pickard CJ, Hasnip PJ, Clark SJ, Payne MC. First-principles simulation: ideas, illusions and the CASTEP code. J Phys Condens matter 14 (2002) 2717.

[64] Vanderbilt D. Soft Self-consistent Pseudopotentials in a generalized eigenvalue formalism. Phys Rev B 41 (1990) 7892.

[65] Perdew JP, Burke K, Ernzerhof M. Generalized gradient approximation made simple. Phys Rev Lett 77 (1996) 3865.

[66] Monkhorst HJ, Pack JD. Special points for Brillouin-zone integrations. Phys Rev B 13 (1976) 5188.

[67] Pfrommer BG, Côté M, Louie SG, Cohen ML.Generation of turbulent inflow data for spatially-developing boundary layer simulations. J Comput Phys 131 (1997) 233.

[68] Govind N, Petersen M, Fitzgerald G, King-Smith D, Andzelm. A generalized synchronous transit method for transition state location. J. Comp Mater Sci 28 (2003) 250.

[69] Wang JY, Zhou YC, Liao T, Zhang J, Lin ZJ. A first-principles investigation of the phase stability of Ti_2AlC with Al vacancies. Scripta Materialia 58 (2008) 227.

[70] Kubaschewski O, Dench WA. The heats of formation in the systems titanium-aluminum and titanium-iron. Acta. Metall. et Mater. 3 (1955) 339.

[71] Stuve JM, Ferrante M J. Report of Investigations-United States, Bureau of Mines (1974) 7834.

[72] Srinivasan S, Desch PB, Schwartz RB. Metastable phases in the Al_3X (X = Ti, Zr, and Hf) intermetallic system. Script. Metall. et Mater. 25 (1991) 2513.

[73] Maas J, Bastin G, vanLoo F, Metselaar RZ. The texture in diffusion-grown layers of trialuminides $TiAl_3$, Val_3, $TaAl_3$, $NbAl_3$, $ZrAl_3$, $HfAl_3$ and VNi_3. Z. Metallkde. 74 (1983) 294.

[74] Frazier WE, Benci JE. Crystal structure and phase relationships in as-cast and melt spus Al_3Ti and Al_3Ti plus copper. Script. Metall. Mater. 25 (1991) 2267.

[75] Watson RE, Weinert M. Transition-metal aluminide formation: Ti, V, Fe, and Ni aluminides. Phys Rev B 58 (1998) 5981.

[76] Mark OR, Falicov LM. Electronic theory of ordering and segregation in transition-metal alloys. Phys Rev B 29 (1984) 1333.

[77] Ershbaumer H, Podloucky R, Rogl P, Temnitschka G, Wanger R. Atomic modelling of Nb, V, Cr, and Mn substitutions in γ-TiAl. I: c/a ratio and site preference. Intermetallics 1 (1993) 99.

[78] Zou J, Fu CL, Yoo MH. Effects of ternary addition on the structure stability of Ti_3Al. Philos. Mag. Lett. 71 (1995) 45.

[79] Alahmed Z, Fu HX. First-principles determination of chemical potentials and vacancy formation energies in $PbTiO_3$ and $BaTiO_3$. Phys. Rev. B 76 (2007) 224101.

[80] Wei SH, Zhang SB. Chemical trends of defect formation and doping limit in II-VI semiconductors: The case of CdTe. Phys. Rew. B 66 (2002) 155211.

[81] Zhu GL, Dai YB, Shu D, Wang J, Sun BD. Substitution behavior of Si in Al_3Ti ($D0_{22}$)- a first-principles study. J Phys Condens Matter 21 (2009) 415503.

Summary

Aluminium is one of the most important metals in our life. The recycling of Al alloys plays a significant role in sustainable development of the Al industry. Compared to primary aluminium production from bauxite, several advantages can be achieved from Al alloy recycling: energy saving, waste disposal reduction, emission reduction and capital cost reduction. High strength aerospace Al alloys are important members in the Al alloy family. The fibre reinforced metal laminates GLARE containing 67 wt% 2024 Al alloy is used as fuselage in Airbus A380, but the solution for GLARE recycling is still lacking. Thermal recycling method was always used to recycle fibre reinforced polymers (FRPs) with good efficiency. This thesis developed a practical solution based on thermal recycling for GLARE recycling on industrial scale. The decomposition behaviour of resins in GLARE was studied, as well as the recycling of separated 2024 Al alloy after thermal delamination.

Silicon is a usual impurity element in aerospace Al alloys, Si content will always be increased during recycling and exceeds the maximum permissible Si concentration of aerospace Al alloys. The main reason for the increase of Si concentration in the secondary aerospace Al is that small amount of high-silicon Al alloy scrap is introduced into aerospace Al scrap during the cutting, shredding and classification process of retired aircraft. At present, commercial pure aluminium has to be added into secondary aluminium to ensure the impurity silicon and iron content within the limit. With the fast growing of secondary aluminium industry, a direct method for removal of impurity silicon from aluminium melt is highly demanded. Impurity silicon removal from Al was investigated by several methods, including directional solidification, alloying method and external field method. But, unfortunately, no one is successfully used for the removal of impurity silicon from Al alloy in industry. In this thesis, an attempt to remove the impurity element Si from Al melt on industrial scale was studied. After the evaluation of Al-Si-X ternary diagrams, research based on alloying method by using Ti addition was conducted to investigate the Si removal efficiency. We focus on impurity Si removal from an Al-Si melt with very low Si concentration, generally lower than 1 wt%, which is significant for wrought Al recycling and refining.

The current solutions for FRPs recycling and Al recycling were reviewed in *Chapter 1*. Mechanical recycling, chemical recycling and thermal recycling are main solutions for FRPs recycling. For Al alloy recycling, the refining method is the practical solution in industry.

In *Chapter 2*, thermal method was employed for GLARE recycling. The thermal decomposition behaviour of epoxy resins BR127 and FM 94 in GLARE under non-isothermal and isothermal conditions were investigated to obtain suitable treatment temperature for GLARE thermal delamination, and epoxy resins decomposition kinetic

models were built up. The resins decomposition consists of four steps under non-isothermal condition, first step is attributed to the decomposition of BR 127, and later three steps are attributed to decomposition of FM 94. The initial decomposition temperature of BR 127 and FM 94 is 188 ^{o}C and 255 ^{o}C, respectively in both oxidising and inert atmospheres when the heating rate of 1 ^{o}C min^{-1} is employed. But the exothermic peak in step four was much higher in air compared to that in nitrogen, and the oxidising atmosphere is more beneficial to the epoxy resins decomposition compared to inert atmosphere. The isothermal kinetics of resins decomposition at 230 ^{o}C, 310 ^{o}C, 350 ^{o}C and 450 ^{o}C were studied, the isothermal temperatures were selected based on non-isothermal thermal analysis results. The conversion is 4.4%, 48.4%, 57.8% and 100% respectively when samples were placed at 230 ^{o}C, 310 ^{o}C, 350 ^{o}C and 450 ^{o}C for 3 hours in nitrogen, while the conversion under same conditions in air is 7.2%, 43.4%, 69.4% and 100% respectively. All epoxy resins in GLARE can be completely decomposed at 450 ^{o}C, the required time is 100 and 70 min respectively in nitrogen and air. Oxidising atmosphere is more preferred for resins decomposition which is consistent with the non-isothermal analysis results. Two decomposition mechanisms, *n*th-order for decomposition at 230 ^{o}C and 450 ^{o}C and autocatalysis for the decomposition at 310 ^{o}C and 350 ^{o}C, were found during isothermal analysis.

The refined GLARE thermal delamination process is 480 ^{o}C for 2 hours based on thermal analysis results and experimental optimization, and the S2-glass fibres and 2024 Al alloys can be well separated by using this process. Most of residues on the surfaces of Al sheets can be removed in water with ultrasonic cleaning after the decomposition of primer BR 127 during thermal delamination.

After GLARE delamination, the recycling of separated 2024 Al sheets was studied in *Chapter 3*. The refining method is employed in this work because of the concise operation and the high quality of recycled Al alloy. $NaCl-KCl-Na_3AlF_6$ and $NaCl-KCl-MgF_2$ were used as fluxes respectively during the 2024 Al re-melting. For $NaCl-KCl-Na_3AlF_6$ flux, the efficiency of two different ratios of NaCl to KCl, 70%NaCl-30% KCl and 44%NaCl-56%KCl, were discussed. Additional 10 wt% cryolite is preferred for both fluxes considering the recycled Al alloy quality together with the economic cost. But, the yield of big metal beads (> 2 mm) after recycling with $44\%NaCl-56\%KCl-10\%Na_3AlF_6$ is lightly increased compared to $70\%NaCl-30\% KCl-10\%Na_3AlF_6$. It was attributed to the lower melting point of equimolar NaCl-KCl system which has a positive influence on the metal coalescence due to the lower viscosity of molten flux. The concentrations of major alloying elements and impurity elements in recycled Al alloys are consistent with nomination composition of 2024 alloy except for Mg, and the Mg loss is caused by the reaction between Mg and cryolite. The big metal beads yield (>2 mm) is obviously decreased with the amount of salts flux. The metal yield was drastically decreased when the weight ratio of salts flux to Al scrap was lower than 1.5. The reduction of metal yield is attributed to the reduced fluidity of salts flux and decreased metal coalescence capacity. The fluidity of flux and Al melt is decreased with the decreasing of re-melting temperature. The decreased fluidity is deleterious to metal droplets aggregation, resulting in a lower metal yield. The lower metal yield for the smaller size scrap recycling is mainly due to more oxides on the higher specific surface area and more contaminations which were caused during shredding and packaging. The experimental results indicated that the scrap

size bigger than 10 mm×10 mm should be preferred. For NaCl-KCl-MgF$_2$ flux, the big metal beads yield is decreased with MgF$_2$ addition amount, especially when the amount is bigger than 10 wt%. Different with the influence of cryolite on metal aggregation behaviour, the increase of MgF$_2$ leads to more small size beads, indicating that the metal coalescence capacity reduced with the increasing amount of MgF$_2$ in salts flux. The possible reason for that is the viscosity of molten salt flux increased with MgF$_2$ addition amount while the high viscosity is unfavourable for the movement of aluminium droplets. The effect of Ti-6Al-4V shear hi lock in fuselage on the GLARE End of Life recycling was also evaluated in this chapter. The calculation result shows that the weight ratios of Ti alloy hi lock to 2024 alloy are 0.73% and 0.94% when hi lock with D_{pin} of 5/32 and 6/32 inch is used, respectively, which will leads to unsatisfied Ti concentration of 0.682 wt% and 0.876 wt%. But the experimental results indicated that the Ti-6Al-4V hi lock will not dissolve into Al melt while hi lock will settle down to the bottom of crucible due to the higher melting point and bigger density of Ti-6Al-4V alloy compared to 2024 Al. Thus, the Ti concentration in the recycled Al alloy within the range of 2024 Al alloy nominal composition can be obtained after re-melting.

In *Chapter 4*, all elements of the periodic table were considered for the selection of feasible elements which can react with low concentration Si in Al melt and form binary or ternary phases with high melting point which can be easily removed to decrease impurity Si concentration. Herein, just ternary Al-Si-X (X is the candidate element) phase diagrams were considered due to complexity and data shortage for quaternary and multi-elements phase diagrams. Titanium is the probable candidate element after the evaluation of Al-Si-X ternary phase diagrams. However, the experiment results indicated that Si can replace Al in Al$_3$Ti phase and form high melting point (Al$_{1-x}$,Si$_x$)$_3$Ti particles, but no TiSi or other Si-rich binary phases were found when 1 wt% Ti was added into Al-Si alloy melt (Si content < 1 wt%). Si purification efficiency is related to the initial Si concentration in Al melt. With the addition of 1 wt% Ti, the decrease of Si concentration is 0.01 wt% when the initial Si concentration is 0.14 wt% but the decrease of Si is enhanced to 0.17 wt% for Al melt with initial Si concentration of 1.04 wt%. The holding temperature has little influence on Si purification efficiency when the Si initial concentration in Al melt is 0.20 wt%. Though the increase of Ti addition amount can slightly improve the Si removal from Al melt containing 0.2 wt% Si, it will consume more Al. Hence, the Si purification efficiency by alloying method with Ti addition is poor for Al melt with low Si initial concentration.

Si substitution behaviour in Al$_3$Ti was investigated by using first-principles calculation to understand the potential of Ti addition on Si removal. The results indicated Si generally prefers to occupy Al2 site, but both Al1 and Al2 site are preferred at low Si doping concentration (Si<3.125 at.%). The formation energies of point defects and the effect of vacancy on the site preference of Si in D0$_{22}$-Al$_3$Ti were investigated. The most probable vacancy is Ti vacancy under Al-rich condition, and the most possible vacancy is Al2 vacancy under Ti-rich condition. The vacancy migration paths in pure and Si-doped Al$_3$Ti and the effect of Si doping on vacancy formation were also studied in this chapter. In pure Al$_3$Ti, both Al1 vacancy and Ti vacancy prefer to diffuse via the first nearest neighbour hop. Al2 vacancy prefers to diffuse via the second nearest neighbour hop. The intra sublattice diffusion of Ti vacancy needs to overcome a high energy barrier of 5.89 eV, which can be

dramatically reduced by a plausible two-defect complex diffusion mechanism proposed in this work. In Si-doped Al_3Ti, under Al-rich condition, the formation energies of Al1 and Al2 vacancies are decreased compared with those in pure Al_3Ti, but the formation energies of Ti vacancy are slightly increased when Si occupies Al2 or Ti sites. The preferred migration paths for vacancies in Al_3Ti with Si doping are the same with those in pure Al_3Ti except the migration path of Al1 vacancy when Si occupies Ti site. Both Si atoms on Al1 site or Al2 site prefer to diffuse via the nearest neighbour Al1 vacancy with the migration energy barriers of 0.45 eV and 0.62 eV, respectively. The system where Si occupies Ti site is unstable, therefore no saddle point has been found when Si hops to the first nearest Al1 vacancy and nearest Al2 vacancy.

Si prefers to occupy Al site, both doped Si atoms on Al1 site or Al2 site prefer to diffuse via the nearest neighbour Al1 vacancy. But the most probable vacancy in Al_3Ti under Al-rich condition is Ti vacancy, resulting in difficulty of Si diffusion in Al_3Ti. Thus Si atom diffusion in Al_3Ti particles is arduous during Si removal by using Ti addition method, which is unfavourable for Si doping in Al_3Ti. Furthermore, Si doping concentration in Al_3Ti is decreased with the decreasing of initial Si concentration in Al alloy during Si removal experiments. Therefore the potential of alloying method with Ti addition for Si removal from Al alloy is poor.

Si removal efficiency by Ti addition is unsatisfied when initial Si concentration in Al melt is low. Therefore, we should notice that the classification of aerospace Al scrap is critical to reduce the impurity doping during the recycling of aerospace Al alloy considering that the doped Si is hard to be removed on industrial scale. Moreover, this research method about first-principles calculation on Si substitution behaviour in Al_3Ti can be used in other doped systems to well understand doping mechanism.

In conclusion, the thesis explains the following key points: 1) FM94 and BR127 decomposition mechanism in GLARE during thermal delamination, as well as the decomposition kinetics models under isothermal conditions; 2) establishment of GLARE thermal delamination process parameters on industrial scale and the evaluation of GLARE End of Life recycling; 3) the flux behaviour during high strength Al alloy recycling and the influence of different fluxes on the metal yield and recycled high strength Al alloy quality; 4) Si removal efficiency by alloying method with Ti addition and Si substitution behaviour in Al_3Ti.

The successful recycling of GLARE can provide valuable thinking to other fibre reinforced metal laminates recycling, as well as fibre reinforced composites. In addition, the detailed investigation on 2024 Al alloy recycling, such as the influence of different flux types, scrap size, re-melting temperature and additional fluoride amount on metal yield and recycled Al alloy composition, offers significant data to optimize process parameter of Al recycling on industrial scale, and the results also can be extended to the recycling of other Al alloys.

Samenvatting

Aluminium (Al) is een van de belangrijkste metalen in ons leven. De recycling van Al-legeringen speelt een belangrijke rol in de duurzame ontwikkeling van Al-industrie. Ten opzichte van de primaire productie van aluminium uit bauxiet, kan een aantal voordelen worden bereikt met recycling van Al-legeringen: energiebesparing, afval reductie, emissiereductie en kapitaalkostenreductie. Hoge-sterkte Al-legeringen voor de ruimtevaart zijn belangrijke leden van Al-legering familie. De met vezel versterkte metaal laminaten GLARE met 67% (gewicht) 2024 Al-legering werd gebruikt voor de romp in Airbus A380, maar de oplossing voor GLARE recycling was nog niet gevonden. Thermische recycling werd altijd gebruikt om vezelversterkte composieten (FRPs) te recyclen met een goede efficiëntie. Dit proefschrift ontwikkelt een praktische oplossing voor GLARE recycling op industriële schaal. De ontleding van gedrag van harsen in GLARE werd bestudeerd, evenals de terugwinning van afgescheiden 2024-Al legering na thermische delaminatie.

Silicium (Si) is een gebruikelijk vervuilend element in ruimtevaart Al-legeringen. De hoeveelheid Si wordt tijdens de recycling altijd verhoogd en is groter dan de maximaal toelaatbare Si concentratie van lucht- en ruimtevaart Al-legeringen. De belangrijkste oorzaak voor de toename van Si-concentratie in secundair lucht- en ruimtevaart Al is dat kleine hoeveelheden hoog-silicium Al-legering worden toegevoegd aan lucht- en ruimtevaart Al schroot tijdens het snijden, raspen en classificeren van afgedankte vliegtuigen. Momenteel moet commercieel zuiver aluminium worden toegevoegd aan secundair aluminium om vervuiling door silicium en ijzer onder de grens te krijgen. Met de snel groeiende industrie van secundair aluminium, is een directe methode voor het verwijderen van silicium uit vloeibaar aluminium zeer gewenst. Diverse manieren om vervuilend silicium uit Al te verwijden zijn al onderzocht, waaronder gericht stollen, legering methode en externe veld methode. Helaas heeft nog niemand succes geboekt voor het verwijderen van vervuilend silicium uit Al-legeringen in de industrie. In dit proefschrift wordt een poging gedaan om op industriële schaal het vervuilende element Si uit vloeibaar Al te verwijderen bestudeerd. Na de evaluatie van Al-Si-X ternaire diagrammen, werd door middel van een legering methode door toevoeging van Ti onderzocht in hoeverre Si verwijderd was. Wij richten ons op verwijdering van Si uit een vloeibaar Al-Si mengsel met een zeer lage Si concentratie, in het algemeen lager dan 1% van het gewicht, wat van belang is voor recycling en raffinage van gesmeed Al.

De huidige oplossingen voor FRP recycling en Al recycling worden beoordeeld in *hoofdstuk 1*. Mechanische recycling, chemische recycling en thermische recycling zijn de belangrijkste oplossingen voor FRP recycling. Voor Al-legering recycling, de raffinage-methode is de praktische oplossing in de industrie.

In *Hoofdstuk 2* wordt een thermische methode voor GLARE recycling besproken. Het thermische ontledingsgedrag van epoxyharsen BR 127 en FM-94 in GLARE onder niet-isotherme en isotherme omstandigheden werd onderzocht om een geschikte behandeltemperatuur vast te stellen voor GLARE thermische delaminatie. Daarnaast worden kinetische modellen opgebouwd voor de afbraak van epoxyharsen. De ontleding van harsen bestaat uit vier stappen in de niet-isotherme toestand. De eerste stap is de ontleding van BR 127 en de overige drie stappen worden toegeschreven aan ontleding van FM 94. De eerste ontledingstemperatuur van BR 127 en FM 94 is 188 ^{o}C en 255 ^{o}C in respectievelijk oxidatieve en inerte atmosfeer, waarbij een opwarmsnelheid van 1 ^{o}C per minuut wordt gehanteerd. De exotherme piek in stap vier is in lucht veel hoger dan in stikstof en de oxiderende atmosfeer is gunstiger voor de epoxyharsen ontleding vergeleken met inerte atmosfeer. De isotherme kinetiek van ontleding van harsen bij 230 ^{o}C, 310 ^{o}C, 350 ^{o}C en 450 ^{o}C werd bestudeerd, de isotherme temperaturen werden geselecteerd op basis van niet-isotherme thermische analyse resultaten. De omzetting bedraagt 4.4%, 48.4%, 57.8% en 100% bij 230 ^{o}C, 310 ^{o}C, 350 ^{o}C en 450 ^{o}C bij monsters die gedurende 3 uur in stikstof geplaatst werden, terwijl de omzetting onder dezelfde omstandigheden in lucht 7.2%, 43.4%, 69.4% en 100% is. Alle epoxy harsen in GLARE kunnen volledig worden ontleed op 450 ^{o}C, de vereiste tijd is 100 en 70 min in respectievelijk stikstof en lucht. Oxiderende atmosfeer heeft de voorkeur voor ontleding van harsen, wat overeenkomt met de niet-isotherme analyseresultaten. Twee ontledingsmechanismen, n-de orde voor de ontleding bij 230 ^{o}C en 450 ^{o}C en autokatalyse voor de afbraak bij 310 ^{o}C en 350 ^{o}C, werden gevonden tijdens de isotherme analyse.

De verfijnde GLARE thermische delaminatie-proces is 480 ^{o}C gedurende 2 uren op basis van thermische analyse resultaten en experimentele optimalisatie, en de S2-glasvezels en 2024 Al-legeringen kunnen goed worden gescheiden met behulp van dit proces. De meeste residuen op het oppervlak van Al platen kunnen worden verwijderd met water met een ultrasone reiniging na primer BR 127 ontleding.

Na GLARE delaminatie, wordt de recycling van gescheiden 2024 Al platen bestudeerd in *hoofdstuk 3*. In dit werk wordt een refining methode toegepast vanwege het beperkte gebruik en de hoge kwaliteit van gerecycled Al-legeringen. NaCl KCl-NaCl-Na$_3$AlF$_6$ en- KCl-MgF$_2$ werden gebruikt als flux tijdens het hersmelten van 2024 Al. Voor NaCl-KCl-Na$_3$AlF$_6$ flux wordt de doelmatigheid van twee verschillende verhoudingen van NaCl-KCl (70% NaCl-30% KCl en 44% NaCl-56% KCl) besproken. 10 gew% extra kryoliet heeft in beide gevallen de voorkeur, gezien de kwaliteit en economische kosten van de gerecyclede Al-legering. Maar de opbrengst van grote metalen kralen (> 2 mm) is bij recycling met 44% NaCl-56% KCl-10% Na$_3$AlF$_6$ licht hoger dan bij 70% NaCl-30% KCl-10% Na$_3$AlF$_6$. Dit wordt toegeschreven aan het lagere smeltpunt van equimolaire NaCl KCl-systeem dat een positieve invloed heeft op de metaalcoalescentie door de lagere viscositeit van gesmolten flux. De concentraties van belangrijke legeringselementen en verontreinigingelementen in gerecyclede Al-legeringen zijn consistent met de samenstelling van de 2024 legering behalve Mg. Het verlies van Mg wordt veroorzaakt door de reactie tussen Mg en kryoliet. De grote metalen kralen opbrengst (> 2 mm) is drastisch afgenomen met de hoeveelheid

zout flux. De metaal opbrengst was drastisch verminderd wanneer de gewichtsverhouding van zout flux ten opzichte van Al schroot lager was dan 1.5. De reductie van metaal opbrengst is toe te schrijven aan de verminderde vloeibaarheid van zout flux en verminderde coalescentie capaciteit van het metaal. De fluïditeit van flux en gesmolten Al neemt af bij een afnemende hersmelttemperatuur. De verminderde vloeibaarheid is schadelijk voor de aggregatie van metaaldruppels, resulterend in een lagere metaalopbrengst. Het lagere metaalrendement voor recycling van het fijnere schroot komt vooral door meer oxyden op het hogere specifieke oppervlak en door verontreinigingen die ontstaan tijdens versnipperen en verpakken. De experimentele resultaten gaven aan dat de voorkeur gegeven moet worden aan een schrootmaat groter dan 10 mm $\times$ 10 mm. Voor NaCl-KCl-MgF$_2$ flux, daalde de opbrengst van grote metalen kralen bij toevoeging van MgF$_2$, vooral wanneer de hoeveelheid groter was dan 10 gew%. Afwijkend van de invloed van kryoliet op metaal aggregatie gedrag, leidt de toename van MgF$_2$ tot meer kleine kralen, wat aangeeft dat de metaalcoalescentie capaciteit vermindert bij een toenemende hoeveelheid MgF$_2$ in zout flux. De mogelijke oorzaak hiervoor is dat de viscositeit van gesmolten zout flux toeneemt bij toevoeging van MgF$_2$, terwijl de hoge viscositeit ongunstig is voor de beweging van aluminium druppels. Het effect van Ti-6Al-4V shear hi lock in de romp op de Glare End of Life recycling wordt ook geëvalueerd in dit hoofdstuk. Uit de berekening blijkt dat de gewichtsverhouding van Ti legeringen hi lock ten opzichte van 2024 legering 0.73% en 0.94% bedraagt bij gebruik van hi lock met D$_{pin}$ van 5/32 en 6/32 inch respectievelijk, hetgeen leidt tot onverzadigde Ti-concentratie van 0.682 gew% en 0.876 gew% respectievelijk. De experimentele resultaten tonen echter aan dat de Ti-6Al-4V hi lcok niet zal oplossen in gesmolten Al omdat hi lock naar de bodem zakt door het hogere smeltpunt en de grotere dichtheid van Ti-6Al-4V legering in vergelijking met 2024 Al. Derhalve kan de Ti-concentratie in de gerecyclede Al legering in het bereik van de nominale samenstelling van een 2024 Al legering verkregen worden door hersmelten.

In *hoofdstuk 4*, worden de meeste chemische elementen geëvalueerd om geschikte elementen te selecteren die kunnen reageren met een lage concentratie Si in gesmolten Al en die binaire of ternaire fasen vormen met een hoog smeltpunt, die eenvoudig verwijderd kunnen worden om de vervuilende Si concentratie te verminderen. Hierin worden slechts ternaire Al-Si-X (waarbij X kandidaat element is) fasediagrammen onderzocht aangezien de complexiteit en beschikbare gegevens niet toelaten voor quartaire en multi-elementen fasediagrammen te onderzoeken. Titanium blijkt het waarschijnlijk element na de beoordeling van Al-Si-X ternaire fasediagrammen. Uit de resultaten van het experiment blijkt echter dat Si Al kan vervangen in de Al$_3$Ti fase waarbij (Al$_{1-x}$,Si$_x$)$_3$Ti deeltjes met een hoog smeltpunt gevormd worden, maar geen TiSi of andere Si-rijke binaire fasen werden gevonden wanneer 1 gew% Ti werd toegevoegd aan een gesmolten Al-Si legering (Si-gehalte <1 gew%). De zuiveringsrendement van Si is sterk gerelateerd met de aanvankelijke Si concentratie gesmolten Al. Bij toevoeging van 1 gew% Ti, is de afname van de Si concentratie 0.01 gew.% als de aanvankelijke concentratie Si 0.14 gew% bedraagt, maar de afname van Si wordt verhoogd tot 0.17 gew% als de aanvankelijke Si concentratie in het gesmolten Al 1.04 gew% is. De temperatuur heeft weinig invloed op het Si zuiveringsrendement wanneer de beginconcentratie van Si in gesmolten Al 0.20 gew% is. Hoewel verhoging de toegevoegde hoeveelheid Ti een iets betere Si verwijdering uit

gesmolten Al met 0.2 gew% Si kan geven, zal er meer Al verbruikt worden. Vandaar dat deze legeringsmethode met Ti toevoeging niet geschikt is voor het zuiveren van gesmolten Al met een lage Si-concentratie.

Si substitutie gedrag in Al$_3$Ti onderzocht door elementaire berekeningen om inzicht te verkrijgen in de potentiele invloed van Ti toevoeging op Si verwijdering. De resultaten toonden aan dat Si bij voorkeur Al2 locaties bezet, maar zowel AL1 en AL2 site zijn voorkeur bij lage Si dotering (Si <3,125 bij.%). De vormingsenergieën van puntdefecten en het effect van lacune op de site voorkeur van Si in D0$_{22}$-Al$_3$Ti werden onderzocht. De meest waarschijnlijke lacune onder Al-rijke conditie is Ti lacune, en onder Ti-rijke conditie is de meest voorkomende lacune Al2. De lacune migratie paden in schone en Si-gedoteerde Al$_3$Ti en het effect van Si doping op de lacunevorming worden ook bestudeerd in dit hoofdstuk. In schone Al$_3$Ti, verspreiden zowel Al1 lacunes als Ti lacunes zich bij voorkeur via de dichtstbijzijnde buur. Al2 lacunes daarentegen verspreiden zich liever via de tweede naaste buur. De intra subrooster diffusie van Ti lacunes moet een hoge energie-barrière van 5.89 eV overwinnen, die drastisch kan worden verminderd door een twee-defect complex diffusie mechanisme voorgesteld in dit proefschrift. In Si-gedoteerd Al$_3$Ti, onder Al-rijke voorwaarde zijn de vormingsenergieën van Al1 en Al2 lacunes gedaald in vergelijking met die in schone Al$_3$Ti, maar de vormingsenergieën van Ti lacunes worden licht verhoogd wanneer Si Al2 of Ti locaties bezet. De geprefereerde migratiepaden voor lacunes in Al$_3$Ti met Si doping zijn gelijk aan die in schone Al$_3$Ti met uitzondering van het migratiepad van de Al1 lacune indien Si een Ti locatie bezet. Zowel Si-atomen op een Al1 locatie als op een Al2 locatie geven er de voorkeur aan via de dichtstbijzijnde Al1 buren lacunes te verspreiden met de migratie energie barrières van 0.45 eV en 0.62 eV, respectievelijk. Het systeem waarbij Si bezet Ti onstabiel is, is dan ook geen zadel punt is gevonden bij Si hop naar de eerste dichtstbijzijnde AL1 leegstand en dichtstbijzijnde Al2 vacature.

Si geeft er de voorkeur aan Al locaties te bezetten, gedoteerde Si-atomen op Al of Al2 locaties verspreiden zich liever via de dichtstbijzijnde Al1 lacune. Maar de meest waarschijnlijke lacunes in Al$_3$Ti onder Al-rijke voorwaarde zijn Ti lacunes, wat resulteert in moeizame Si diffusie in Al$_3$Ti. Daarom verloopt Si atoom diffusie in Al$_3$Ti deeltjes niet zo vlotjes tijdens Si verwijdering bij toepassing van de Ti toevoeging methode, hetgeen ongunstig is voor Si doping in de Al$_3$Ti. Bovendien moet de Si doteringsconcentratie in Al$_3$Ti af bij afnemende aanvankelijke Si concentratie in de Al legering tijdens Si verwijderingsexperimenten. Daarom is de potentie van de legeringsmethode met Ti toevoeging voor de verwijdering van Si uit een Al-legering slecht.

Het Si verwijderingsrendement door Ti toevoeging is onbevredigend als de aanvankelijke Si concentratie in gesmolten Al laag is. Daarom moeten we opmerken dat de classificatie van lucht- en ruimtevaart Al schroot cruciaal is om de onzuiverheid doping gedurende de recycling van lucht- en ruimtevaart Al-legering te reduceren, aangezien de gedoteerde Si moeilijk op industriële schaal te verwijderen is. Bovendien kan deze methode van onderzoek naar elementaire berekening van Si substitutie gedrag in Al$_3$Ti worden gebruikt in andere vervuilde systemen om het dopingmechanisme goed te begrijpen.

Tot slot, het proefschrift belicht de volgende belangrijke punten: 1) FM94 en BR127 ontledingsmechanisme in GLARE tijdens thermische delaminatie, evenals de ontledingskinetiek modellen onder isotherme condities, 2) vaststelling van GLARE thermische delaminatie procesparameters op industriële schaal en de evaluatie van GLARE End of Life recycling, 3) het flux gedrag tijdens recycling van een hoge sterkte Al-legering en de invloed van verschillende stromen op de metaalopbrengst en op de kwaliteit van gerecycled hoge sterkte Al-legeringen; 4) Si verwijderingsrendement bij de legering methode met Ti toevoeging en Si substitutie gedrag in Al_3Ti.

De succesvolle recycling van GLARE kan een waardevolle denkrichting bieden voor recycling van andere vezelversterkte metaallaminaten, en vezelversterkte composieten. Bovendien biedt het diepgaand onderzoek naar recycling van 2024 Al-legeringen (zoals de invloed van verschillende types flux, schrootgrootte, hersmelttemperatuur en extra fluoride toevoeging op metaalopbrengst en samenstelling van de Al-legering) significante gegevens om procesparameter voor Al-recycling op industriële schaal te optimaliseren. Daarnaast kunnen de resultaten worden uitgebreid ten behoeve van de recycling van andere Al-legeringen.

List of publications

Journal

1. **Guoliang Zhu**, Yongbing Dai, Da Shu, Jun Wang, Baode Sun, "*First-principles study on substitution behavior of Si in TiAl$_3$.*" Acta Physica Sinica 58 (2009) S210.

2. **Guoliang Zhu**, Yongbing Dai, Da Shu, Jun Wang, Baode Sun, *"Substitution behavior of Si in Al$_3$Ti (D0$_{22}$): a first-principles study."* Journal of Physics: Condensed Matter. 21 (2009) 415503.

3. **Guoliang Zhu**, Yongbing Dai, Da Shu, Yanping Xiao, Yongxiang Yang, Jun Wang, Baode Sun, Rob Boom, "*First-principles study of point defects and Si site preference in Al$_3$Ti.*" Computational Materials Science 50 (2011) 2636.

4. **Guoliang Zhu**, Yongbing Dai, Da Shu, Yanping Xiao, Yongxiang Yang, Jun Wang, Baode Sun, Rob Boom, "*Diffusion mechanisms of vacancy and doped Si in Al$_3$Ti from first-principles calculations.*" Intermetallics 19 (2011) 1036.

5. **Guoliang Zhu**, Yanping Xiao, Yongxiang Yang, Guiming Song, Jun Wang, Baode Sun, Rob Boom, "*Thermal degradation behaviour of resins in GLARE.*" To be submitted.

6. **Guoliang Zhu**, Yongxiang Yang, Yanping Xiao, Jun Wang, Baode Sun, Rob Boom, "*Thermal Recycling of fibre metal laminates GLARE.*" To be submitted.

Conferences

1. Yongxiang Yang, **Guoliang Zhu**, Yanping Xiao, "*Recycling of Fibre-Metal Laminates: GLARE*" in 2011 International Conference on Advanced Engineering Materials and Technology, July 29-31 2011, Sanya, China.
Published in: Advanced Materials Research 295-297 (2011) 2329.

2 **Guoliang Zhu**, Yanping Xiao, Yongxiang Yang, Jun Wang, Baode Sun, Rob Boom, "*Degradation behavior of epoxy resins in fibre metal laminates under thermal conditions.*" in 10th International Conference on Eco-materials, November 21-24 2011, Shanghai, China.
Published in: Journal of Shanghai Jiaotong University (Science) 17 (2012) 257.

3. **Guoliang Zhu**, Yongxiang Yang, Yanping Xiao, Jun Wang, Baode Sun, Rob Boom, "*Recycling of aluminum from Fibre Metal Laminates.*" in 10th International Conference on Eco-materials, November 21-24 2011, Shanghai, China.
Published in: Journal of Shanghai Jiaotong University (Science) 17 (2012) 263.

Curriculum Vitae

Guoliang Zhu

Born on 21 September, 1983
in Linli, Hunan Province, China

Sept. 2000 – Jul. 2004

Bachelor of Science in Engineering, Department of Mechanical Engineering, Xiangtan University, Xiangtan, China.

Sept. 2004 – Jul. 2006

Master of Science in Materials Science, Department of Materials Science and Engineering, Haerbin Institute of Technology, Haerbin, China, under supervision of Prof. Zunjie Wei.

Sept. 2006 – Oct. 2009

Ph.D. candidate in the group of Solidification Science of Technology, Department of Materials Science and Engineering, Shanghai Jiao Tong University, Shanghai, China, under supervision of Prof. Baode Sun.

Oct. 2009 – Oct. 2012

Joint Ph.D. candidate in the group of Light Metal Processing, Department of Materials Science and Engineering, Faculty of Mechanical, Maritime, Materials Engineering (3ME), Delft University of Technology, Delft, The Netherlands, under supervision of Prof. dr. Rob Boom and Assoc. Prof. dr. Yongxiang Yang.